THE HONG KONG
POLYTECHNIC UNIVERSITY
香港理工大學

Pao Yue-kong Library
包玉剛圖書館

Copyright Undertaking

This thesis is protected by copyright, with all rights reserved.

By reading and using the thesis, the reader understands and agrees to the following terms:

1. The reader will abide by the rules and legal ordinances governing copyright regarding the use of the thesis.

2. The reader will use the thesis for the purpose of research or private study only and not for distribution or further reproduction or any other purpose.

3. The reader agrees to indemnify and hold the University harmless from and against any loss, damage, cost, liability or expenses arising from copyright infringement or unauthorized usage.

If you have reasons to believe that any materials in this thesis are deemed not suitable to be distributed in this form, or a copyright owner having difficulty with the material being included in our database, please contact lbsys@polyu.edu.hk providing details. The Library will look into your claim and consider taking remedial action upon receipt of the written requests.

Pao Yue-kong Library, The Hong Kong Polytechnic University, Hung Hom, Kowloon, Hong Kong

http://www.lib.polyu.edu.hk

High Power Nd:YAG Laser Welding of SiC Particle

Reinforced Aluminium Alloy 2124

by

Du Jihua

A thesis submitted to

The Hong Kong Polytechnic University

for the degree of

Master of Philosophy

At

Department of Manufacturing Engineering

The Hong Kong Polytechnic University

In November 1997

Abstract of thesis entitled 'High Power Nd:YAG Laser Welding of SiC Particle

Reinforced Aluminium Alloy 2124'

Submitted by <u>Du Jihua</u>

For the degree of M.Phil.

At The Hong Kong Polytechnic University in November 1997

In this research, the effects of different YAG-laser output waveforms on the weldability of a SiC particle reinforced Al-alloy 2124 have been studied. In addition, a new laser joining technique has been developed with an aim to avoid the formation of harmful aluminium carbide phases in the fusion zone. This technique involved brush plating of nickel on the aluminium composite prior to laser welding.

The results show that although the square waveform can produce the greatest depth-of-penetration amongst the three different waveforms studied, i.e. CW, sine-wave and square-wave, a high level of porosity was observed in the weld. This is believed due to the inherent fast cooling rate of the square-wave process. Whereas, porosity free welds with a reasonable depth-of-penetration could be obtained by using a sine-waveform operated at high peak powers. However, the results also clearly show that it would not be possible to stop the formation of aluminium carbides in the weld entirely simply by varying the laser output parameters and the waveform. The penetration depth of the fusion zone was successfully predicted by using a threshold laser intensity model.

In order to stop the formation of aluminium carbides in the weld, nickel coating of a thickness between 0.15-0.25 mm was applied to the joining surfaces by means of a

brush plating technique prior to laser welding. With an appropriate thickness of nickel coating, it was found possible to prevent the formation of aluminium carbides in the weld zone. Good metallurgical bond was obtained between the Ni coating and the composite matrix. Moreover, the results show that for the plated samples the power intensity required for achieving the same depth of weld penetration as in the case of the non-plated samples was at least 25% lower. Corrosion test results of the weld zone show that the overall corrosion current was reduced by a factor of 10 when nickel plating was employed. For the non-nickel plated joint the fusion zone would be completely destroyed after leaving it in laboratory air for two weeks. This was due to the hydrolysis of Al_4C_3 to $Al(OH)_3$.

Acknowledgements

Chapter 1. Introduction

1.1   Problems in laser welding of SiC_p/Al MMCs

Silicon carbide particle reinforced aluminium alloy metal matrix composites

(SiC_p/Al MMCs) are attractive to aerospace and automobile industries due to their

high specific properties and relatively inexpensive price. [1-3] Unfortunately, these

materials have very poor weldability, and fusion welding of MMCs has been shown to

be problematic. Their poor weldability to certain extent has limited the widespread

application of these materials. The welding problem arises mainly due to the inherent

high thermal conductivity and viscosity of these materials, as a result poor weld

penetration and formation of porosity occur. [4,5] Among the major welding

techniques, laser welding using CO_2 lasers has shown limited success in the welding of

certain types of Al-Si/SiC MMCs [6-8]. The merits of laser welding are apparent: the

intrinsic focusing ability and the possibility of transmitting lasers to the workpiece by

optical fibres has increased the flexibility of the process. In addition, autogenous laser

welding without resorting to filler metals is another distinct advantage over many

conventional welding techniques. However, having mentioned all these, the major

welding problems of MMCs are largely unsolved when CO_2 lasers or traditional

pulsed Nd:YAG lasers were used. The results show that although the weld quality

could be improved by the optimisation of the laser output parameters, the welding

results were still far from satisfactory.

Now, with the latest developed high power Nd:YAG lasers (output power in

the range of 2-4kW) some of the welding problems encountered may be overcome.

This is made possible because metals show a higher absorpability to YAG lasers

than CO_2 lasers. Also, most of the commercially available high power YAG lasers not only can produce output wave in a continuous form (CW), but also can generate different types of pulse waveforms. The effects of different waveforms on the weldability of SiC/Al composites will be dealt with in this study.

Another issue that required paying attention to when welding MMCs is that most of the matrix/reinforcement systems are thermodynamically unstable. In laser welding, the intense heat input will inevitably upset the existing metastable micro-environment. This very often will result in the formation of brittle Al-carbide phases, such as Al_4C_3, which can cause the corrosion resistance and the toughness of the material to be reduced to an unacceptably low level [9-10]. Moreover, the problem of the hydrolysis of Al_4C_3 could further accelerate the degradation of the material. In order to stop the formation of brittle carbides in the weld zone, a pre-welding treatment using a brush plating technique will be adopted in this research.

1.2   Scope and objectives

1.2.1   The Effects of Laser Output Waveforms on Welding Performance

In this part of the study, the effects of different waveforms of a high power Nd:YAG laser on the welding performance of a SiC/Al composite will be studied in some detail. Three different types of waveforms will be considered in this study, namely: continue wave (CW), sine-wave (SIN) and square-wave (SQR) Other laser processing parameter such as pulse frequency, mean power, and feed rate will also be included. The main objectives of this part of the study can be summarised as below.

- To study the effects of laser output waveform as well as other laser processing parameters on the microstructure and dimensions of laser welds.

- To determine the optimum laser welding parameters in the consideration of maximum penetration depth, occurrence of porosity and aluminium carbide phase.

- To predict the depth-of-penetration of laser welds by using the critical laser intensity model.

1.2.2 Elimination of Aluminium Carbides by Means of Nickel Plating

In order to stop the formation of brittle carbides in the weld, some laser welding experiment will be performed using a "sandwich" technique in which the joining surfaces will be coated with a layer of nickel by means of the brush plating technique. In the welding process, the laser beam would be directed onto the nickel plated region (Fig. 1.1). The merit of this technique is apparent: the beam is no longer coming to direct contact with the composite material. Provided an optimum condition is arrived, it is conceivable that minimal microstructural changes would occur at the nickel/composite interface. A further advantage arises in using this technique over the conventional fusion methods is that no filler material is required. Although, in some respects this approach is similar to the diffusion welding technique (DWT), they differ greatly in that the DWT requires a squeezing pressure, and normally the whole diffusion cycle will take many hours. To the author's knowledge the proposed "sandwich" technique making use of brush plating has not been applied in laser welding of metal matrix composites.

The objectives of this part of the research are:

- To stop the formation of carbide phases in laser welding of SiC/Al composite by means of a "sandwich" welding technique.

- To have a better understanding on the thermal condition of the formation of aluminium carbides in laser welding through the study of the microstructure of the nickel-MMC interface.

- To evaluate the corrosion properties of both the laser welds with and without nickel plating.
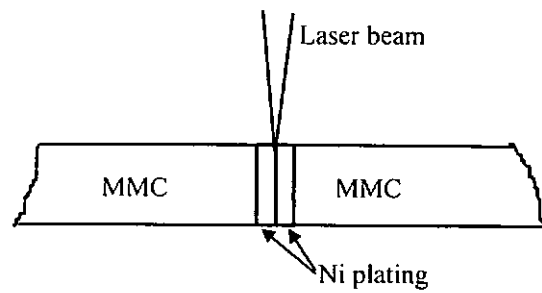

Figure 1.1: Butt-joint laser welding of MMC with Ni plating.
("sandwich" technique)

Chapter 2. Background and Literature Review

2.1 Metal matrix composites (MMCs)

2.1.1 MMCs and processing of MMCs

Discontinuously reinforced metal matrix composites (DRCs) represent a group of materials that combine the strength and hardness of the reinforcing phase with the ductility and toughness of the matrix. The high stiffness-to-weight ratio of light alloy MMCs makes them attractive in application fields such as aerospace, automobile and electronics. Aluminium alloys serve as the matrix material in most of the light alloy MMCs due to their excellent mechanical properties. The reinforcements of the matrix are generally available in the following forms:

- Reinforcement by continuous fibers of a high strength material;

- Reinforcement by whiskers or short fibers of a high strength material;

- Reinforcement by particles of a high strength material.

Generally, continuous fiber reinforced composites have higher specific strength in the fiber direction and better fracture toughness than the particle reinforced composites. The particle reinforced composites have much in common with precipitation/dispersion strengthened materials except that the problem of precipitate/dispersoid coarsening does not normally exist. Compared to the continuous fibre reinforced composites the DRCs exhibit isotropic properties. Besides, they are less expensive than those fibre and whisker reinforced MMCs. Thus, they show great promise for stiff and light weight structural applications.

Reinforcements for the composites materials can be silicon carbide, titanium carbide, alumina, and graphite materials. Amongst the reinforcement materials, silicon carbide has the advantages of excellent thermal conductivity and good corrosion resistance. The mechanical and physical properties of DRCs depend very much on the particle morphology, particle size and distribution, particle surface chemistry, fractional content and dispersion uniformity.

Normally, Al-Si alloys are the commonly used matrix material for cast MMCs [11]. Whereas wrought aluminium alloys, such as 2024, 2124, 5156, 6061, 8090 etc. are currently being used to produce MMCs through solid state processes. [12]. The basic requirement and purposes of the matrix materials are:

- Provide ductility;

- Transfer load between individual reinforcement materials;

- In case of fiber reinforced materials, provide transverse strength.

The processing of metal matrix composites can be broadly divided into two categories of fabrication techniques: (a) solid state and (b) liquid state. A majority of the commercially viable applications are now produced by liquid-state processing because of the inherent advantages of this processing technique over solid-state techniques. That is, the liquid metal route is generally less expensive and a wide variety of near-net-shape components can be produced using methods already developed in the casting industry. However, liquid-state processes often suffer from a lack of reproducibility as a result of incomplete control of the processing parameters. Also, undesirable chemical reactions between the molten metal and the reinforcement phase often occur. Besides, they are often limited to some low-melting-point alloys, although some reinforced intermetallics have now been

produced by liquid-state processes. Liquid-state processing technologies can be sorted into four major categories by methods to physically combine the matrix and the reinforcement [2]: (a) Infiltration, (b) Dispersion, (c) Spraying, and (d) In-situ fabrication.

Solid state processes are generally used to obtain the highest mechanical properties in metal matrix composites. This is because segregation effects and brittle reaction product formation are at a minimum in the solid state processes when compared with liquid-state processes. The solid-state processes [2] include: (a) Powder consolidation, (b) Diffusion bonding, (c) High-rate consolidation.

2.1.2 Microstructure and mechanical properties of MMCs

The mechanical properties of MMCs depend very much on their constituents, the physical forms and the uniformity of the dispersion of the reinforcement, the interfacial and microstructural properties. The condition of the reinforcement-matrix interface is an important factor in governing the mechanical properties of the MMCs. Since most MMCs are non-equilibrium systems, a chemical potential gradient exists across the reinforcement-matrix interface. This could result in the formation of an interlayer or compounds with chemistry and properties much different from either that of the matrix or the reinforcement. As a consequence, the mechanical properties and the corrosion resistance of the composite could be adversely affected [13-15]. For the DRCs produced by the solid state routes very often the reinforcement phase appears as stringers and aligned in the material working direction. In these cases the properties of the composites will be anisotropic.

Table 2.1 presents some typical properties of a DRC material, which was manufactured by BP Metal Composites Limited.

Table 2.1: Some typical properties of a SiC_p/Al-2124 MMC

	UTS (MPa)	Strain to failure (%)	0.2% proof strength (MPa)	Modulus (GPa)	Density (g/cc)
2124 Al + 17.8 vol% SiC	610	5-7	400	100	2.85
2124 Al + 25 vol% SiC	630	2-4	490	116	2.88
unreinforced 2124 Al	470	10-12	325	72	2.77

The data presented clearly demonstrate the huge improvement gained in strength and stiffness when SiC particles are added. The addition of 25 vol% silicon carbide particle reinforcement to 2124 aluminium increases the elastic modulus by 61%, yield strength (0.2% proof strength) by 34%, and tensile strength by 51%, while only increases the density by 4%. However, the penalty to pay is a huge reduction in ductility from 10-12% to 2-4%. Harrigan [16] and McDaniels [17] reported that mechanical working such as hot rolling can improve the ductility of SiC_p/Al MMCs substantially. For discontinuous SiC reinforced aluminium, the modulus was observed to be isotropic and independent of the type of reinforcement or the matrix alloy used. The fracture toughness properties of SiC_p/Al MMCs was found to be dependent upon both the matrix and the reinforcement materials. The work by Logsdon [18] showed that SiC reinforced 2124 aluminium composites displayed a fracture toughness-orientation dependence.

2.1.3   *Applications of SiC/Al MMCs*

The high strength/weight ratio and the excellent wear resistance of most MMCs have made them desirable for many engineering applications, especially in

the aerospace and automobile industries. For example, Aluminium based composite materials are being used commercially in producing engine blocks for Honda Prelude[2]. Also, after years of development SiC/Al-Si cast brake discs are finally a commercial reality [19]. Conventional monolithic aluminium and polymer composites have a materials performance limitation of 120°C to 450°C. Yet for high speed aircraft, temperatures can reach over 1600°K at the nose, 1000°K to 1600°K in the lower body. SiC/titanium and SiC/aluminium composites are targeted for use in structural components for the national aerospace plane, advance fighters and gas turbine applications [2]. Moreover, more applications could emerge in other industries such as communication. 3M company has already applied SiC/Al MMCs in providing stiff supporting to their communication optical fibers. Finally, it is foreseen that as the technique and market growing, it is anticipated that the price of MMC materials will be lowered in the near future, as a result many other engineering applications may be able to afford to use these novel materials.

2.2   Joining of SiC$_p$/Al MMCs

Despite recent advancements made in the manufacturing technology of MMCs, as in powder metallurgy, co-spraying, low pressure liquid infiltration and squeeze casting, the need for post-manufacture joining of MMC components are very often required. Thus, the successful implementation of these novel materials will still largely depend on how cost-effectively the component can be fabricated and transformed to the useful final shape. In this connection, to certain extent, their applications will depend on their ability to be joined to themselves and to other monolithic materials. Unfortunately, these materials have poor weldability. Conventional fusion processes present new challenges when welding MMCs because

most aluminium-based MMCs exhibit high viscosity in the molten state, this in fact causes the composite not to be readily mixed with the filler metal. Another concern is the rejection of the reinforcement phase(s) by the solidification front. Furthermore, most of the matrix/reinforcement systems are thermodynamically unstable, therefore, any joining process that involves high heat input will inevitably upset the existing metastable micro-environment. For instance, prolonged exposure of Al-based/SiC composites at reasonably high temperatures may promote reactions between the matrix and the reinforcement phase, in that the formation of brittle Al-carbide phases would cause the corrosion resistance and the toughness of the material to be reduced to an unacceptably low level.

Some processes used for joining composite materials are listed below:

- Arc welding

- Laser beam welding

- Electron beam welding

- Inertia welding

- Diffusion Welding

Basically, these welding techniques could be summarised into two groups: fusion processes and solid state processes.

2.2.1   Fusion processes

Arc welding, laser beam welding and electron beam welding are typical fusion processes, which all produce intensive heat input on a limited area of the material and form a melting pool, so that metallic bonding could be achieved in a short time.
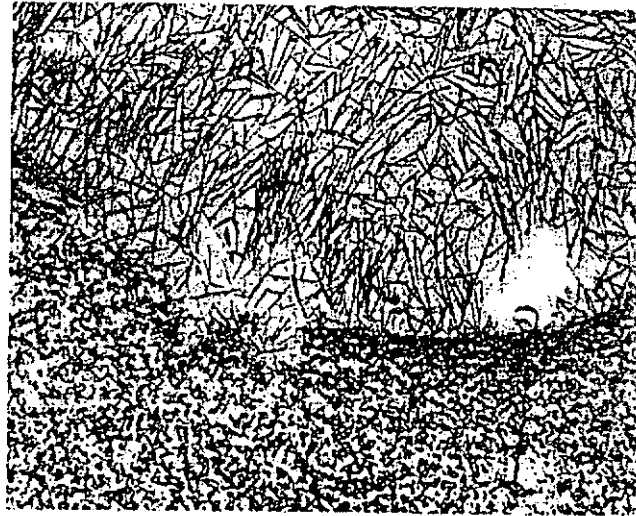
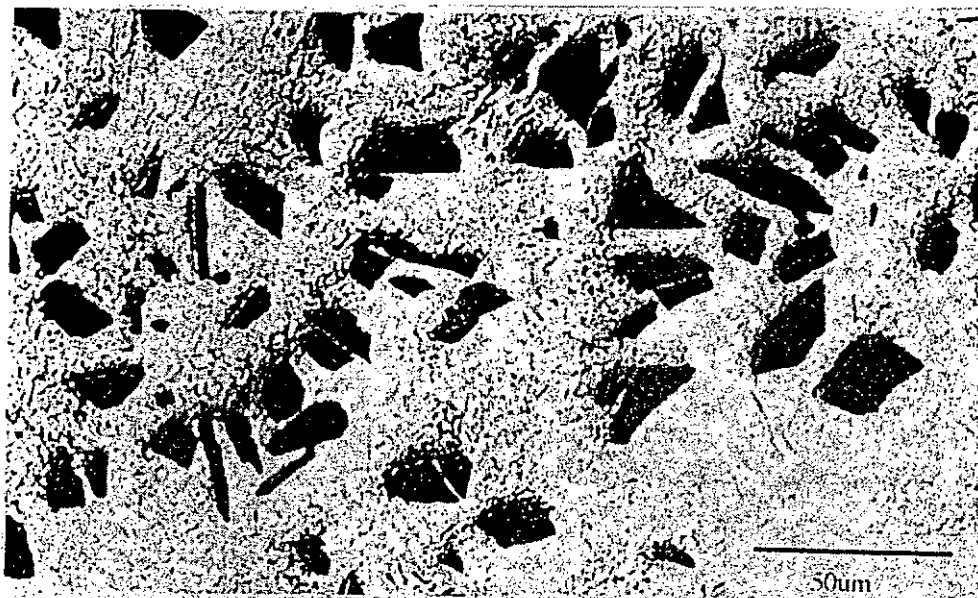Figure 2.1: SiC/Al-2024 joined by GTAW at 170 amperes (50X). [5]

Figure 2.2: Light microgragh of electron beam weld at 3.0 kW, 85mm/sec, and sharp

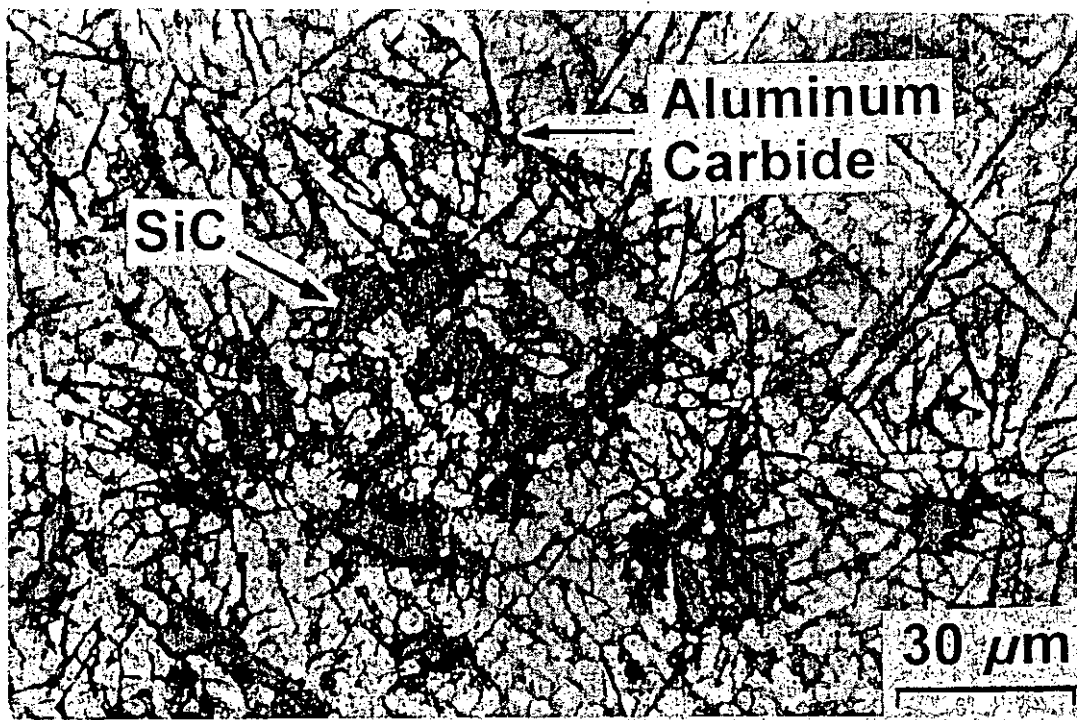focus (estimated beam diameter of 0.4mm) in Al-SiCp. [5]

Figure 2.3: Microstructure showing plate-like phase in laser joined 10 vol% SiC/Al-alloy composite. [29]

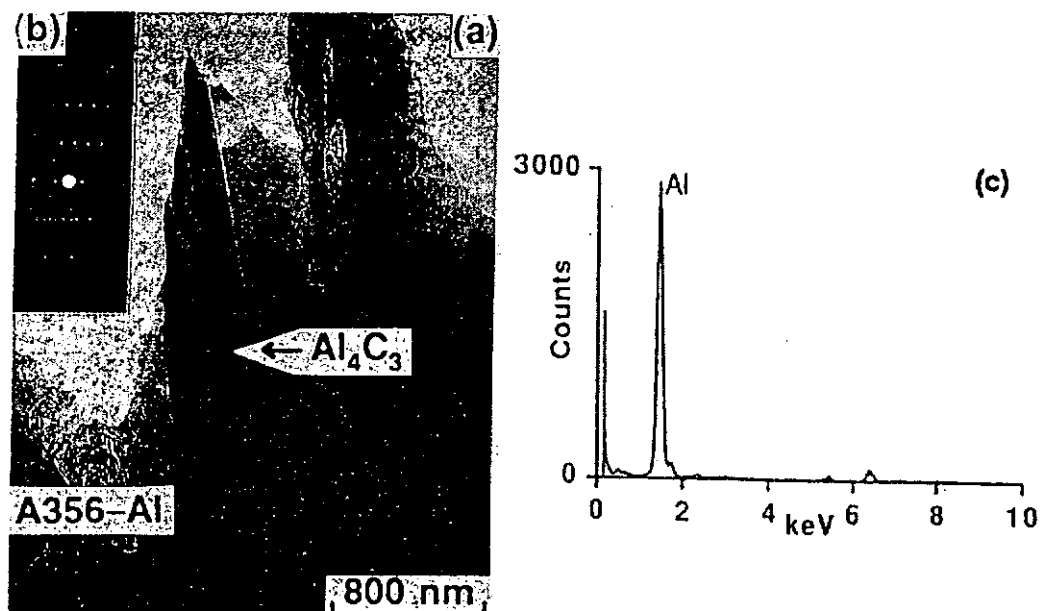Figure2.4: TEM microgragh of aluminum carbide plates in the weld region showing, (a) Al_4C_3 plates in A356 Al matrix, (b) SAD pattern of Al_4C_3 plate with (2210) orientation, and (c) x-ray microchemical analysis on the aluminium carbide plates. [28]

2.2.1.1 Arc Welding

Gas tungsten (GTA) and gas metal arc (GMA) welding processes have been used to join SiC/Al composites [20-21]. From previous studies, it is clear that arc welding faces many problems in joining composite materials. These include the formation of porosity and undesirable chemical reaction products and hot cracking. It was reported that, GTA welding of 40% SiCp/Al-6061 produced a weld pool with significant amount of porosity in the fusion zone and the heat affected zone[4]. Figure 2.1 shows the microstructure of a SiC/Al-2024 composite welded by GTA, where large quantity of plate-like aluminium carbide phases present. The formation of aluminium carbide phases in arc welding can be considered a certainty. The reaction equation is given by:

$$4Al(l) + 3SiC(s) \rightarrow Al_4C_3(s) + 3Si(s)$$

Iseki [22] reported that the reaction could not proceed at temperatures below approximately 730°C, because the free energy change of the reaction is positive:

$$\Delta G \ (J/mol) = 113900 - 12.06 \ TlnT + 8.92 \times 10^{-3} \ T^2 + 7.53 \times 10^{-4} \ T^{-1}$$

$$+ 21.5 \ T + 3RTln \ a_{si}$$

Where a_{si} is the activity of silicon in liquid aluminium. The reaction proceeds as temperature (T) increases above 730°C and ΔG becomes increasingly negative. Obviously, the above reaction can only be applied when an equilibrium thermodynamic condition is reached. From a stand point of kinetic consideration, it will need a much higher temperature to dissolve SiC particle and form Al_4C_3 phase in a highly non-equilibrium processing condition, as in the case of laser welding. Theoretically, the formation of aluminium carbides could be minimised or even

eliminated by lowering the process temperature and reducing the process duration. But in practice this is always unachievable.

2.2.1.2 Electron beam welding (EBM)

Electron beam welding employs a rapid thermal cycle and low heat input. Unlike laser beam, there is no preferential absorption of the energy by silicon carbide particles which could produce excessive heat and hence the reaction between matrix and reinforcement. It was reported that electron beam welding could produce a lower level of aluminium carbide phases than laser beam welding at the same power and speeds [5]. A high travel speed and sharp focus of the beam was recommended to prevent the formation of aluminium carbide phases. Figure 2.2 shows a weld microstructure produced by electron beam. However, the restricted vacuum environment requirement of the technique limits the application.

2.2.1.3 Laser beam welding (LBW)

The laser welding process is capable of producing low heat input, high energy density welds. It is possible to attain a rapidly solidified weld with this process. A number of efforts have been made in welding SiC/Al composites using laser beam. However, nearly all the research reported that [4-7,23-29] massive quantities of plate-like phases were observed in the welds (Figure 2.3). TEM analysis showed that the plate-like phase was mainly aluminium carbide Al_4C_3 [28] (Figure 2.4). In the study of the microstructure of the weld of SiC/Al-Si composites, Dahotre [23] divided the laser weld into three regions (Figure 2.5). The central fusion region (Region A) which contains massive quantity of plate-like aluminium carbides and bulky primary silicon and matrix eutectic. Surrounding this region is an area where there has been a redistribution of SiC particles (Region B).

The edges of the particles have been smoothened as a result of surface melting. This region is followed by a partially melted zone (Region C), in which a fine cellular/dendritic structure in the matrix material is apparent. The weld is surrounded by the unmelted base material represented by Region D.
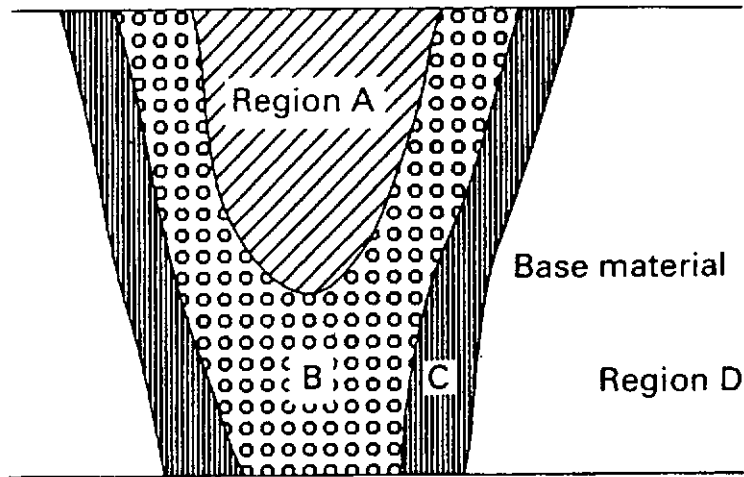

Figure 2.5: Schematic of the laser processed microstructure in Al-SiCp MMCs [23]
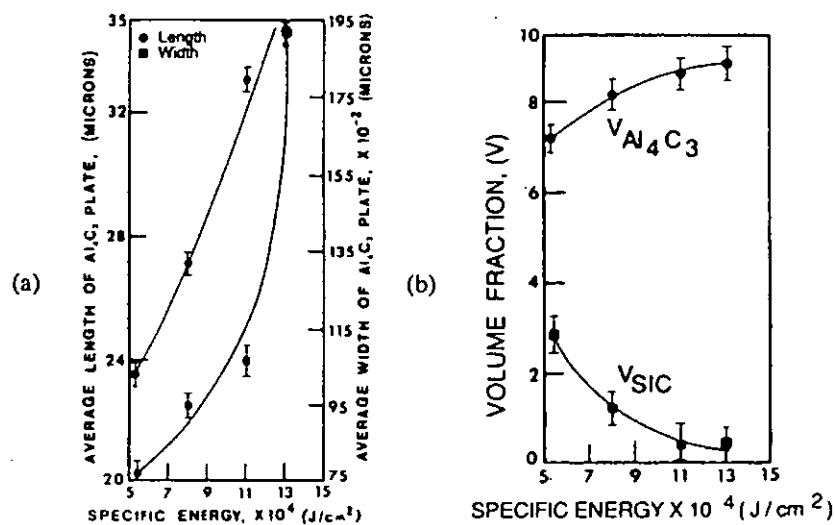

Figure 2.6: (a) The length and width of Al_4C_3 plates and (b) volume fraction of SiC and Al_4C_3 as a function of specific energy. [7]

In the central melted region, the intense heat developed has melted the SiC particles and as a result Al_4C_3 was formed. The amount of heat input has shown to have a significant effects on the amount and the dimension of the Al_4C_3 phase, which can be seen in figure 2.6. In that a drop in the volume of SiC associated with an increase in the volume of Al_4C_3 is evident. A high heat input has destroyed the SiC particles completely and large carbide plates were formed in the fusion zone. Some studies [7,26] have been carried out with an aim to avoid a massive formation of Al_4C_3 and the destruction of SiC particles by processing the composite with the laser operated in a high-frequency short-duration pulse mode. Also, the effects of using different lasers wavelength (CO_2 and Nd:YAG) and different thermal cycle (CW and pulsed wave) on the weldability of MMCs have been studied [23-27]. Although, it was found that the duty cycle of the pulsed laser could affect the degree of the SiC-Al reaction, and the microstructures of YAG laser weld was somewhat finer than those of the welds produced by CO_2 lasers, the formation of aluminium carbide seems to be inevitable. Recently, Dahotre [29] has developed a laser induced liquid phase reaction synthesis method to combat the carbide formation problem. In that a Ti or Ti-alloy reactive filler material was used, and preliminary results obtained were very promising.

In the partially melted zone, where SiC particles survive, the surface of the particles is partially melted. This has provided a strong interface between SiC and the Al matrix. The partially melted SiC particles are believed to act as either heterogeneous nucleation or recrystallization sites for the matrix. [28] The non-equilibrium phases such as Al_4C_3 and $Al_4Si_2C_5$ are sometimes found along the SiC-matrix interface.

Although quite a few reports [24,27] mentioned that due to the high viscosity and thermal conductivity of MMC materials a lot of porosity would form in the weld and the depth of weld penetration would be relatively small, detailed research in this area still remains lacking. As a matter of fact, the laser aborptivity of Al-based SiC composites is much higher that the Al-matrix material because aluminium has a very high laser reflectivity. At 600°C, its absorptivity for 10.6 µm radiation is only 0.031. This low value means that up to 97% of the laser energy is reflected. SiC particles, however, have a high absorptivity of around 0.19. Their presence in Al-alloys should therefore greatly improve the energy absorption ability of the material and the overall effectiveness of laser joining should be improved. Figure 2.7 shows the significant increase in laser absorptivity of the composites over their matrix counterparts.
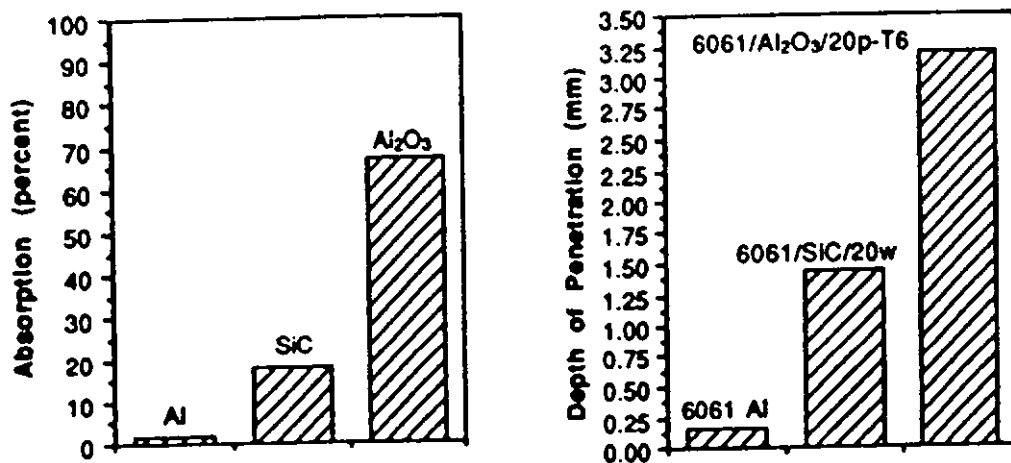

Figure 2.7: Absorptivity and depth of penetration for Al, Al+SiC and Al+Al₂O₃ [24]

In summary, it was found that the formation of aluminium carbide phases and the loss of reinforcement particles are very common in laser welding of SiC/Al-based composites. By controlling the heat input during laser processing, it is

possible to reduce the amount of carbide phases in the weld but seemingly it will not be easy to eliminate them totally.

2.2.2 Solid state processes

Solid state processes such as diffusion bonding have achieved some successful applications of joining composite materials [30-31]. The major advantage is that reinforcement-matrix reactions can be eliminated due to the lower processing temperatures. Moreover, the problems of high viscosity and occluding gases in molten weld pool are removed. The disadvantage of these processes is the restrict condition requirement and long processing time.

2.2.2.1 Inertia welding

In the inertia welding process, one of the two workpieces to be joined is held in a stationary position, while the other piece, attached to a flywheel, is rotated at a high speed. The driving power is removed at a pre-determined speed and the pieces are forced together under axial pressure [32]. Nearly defect free welds with excellent bonding were reported in joining 20 Vol% SiC/6061 Al composite. Figure 2.8 shows a section through the bond line of a inertia welded SiC/Al MMC. The absence of aluminium carbide was confirmed by X-ray diffraction. Inertia welding requires excessive deformation at the interface and may not be applied to components where minimal deformation is required. It also needs post-bond machining, due to the deformation.

2.2.2.2 Diffusion bonding

Successful diffusion bonding of Al-based MMCs has been achieved in previous studies [33-35]. It is a joining process wherein coalescence between two clean and closely fitting parts is obtained under the application of heat and pressure.
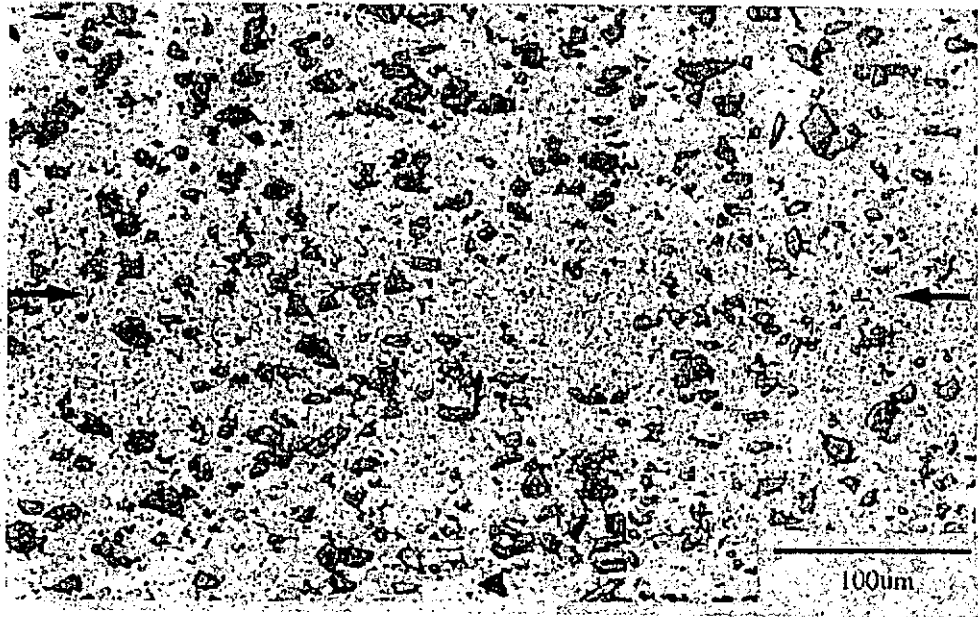
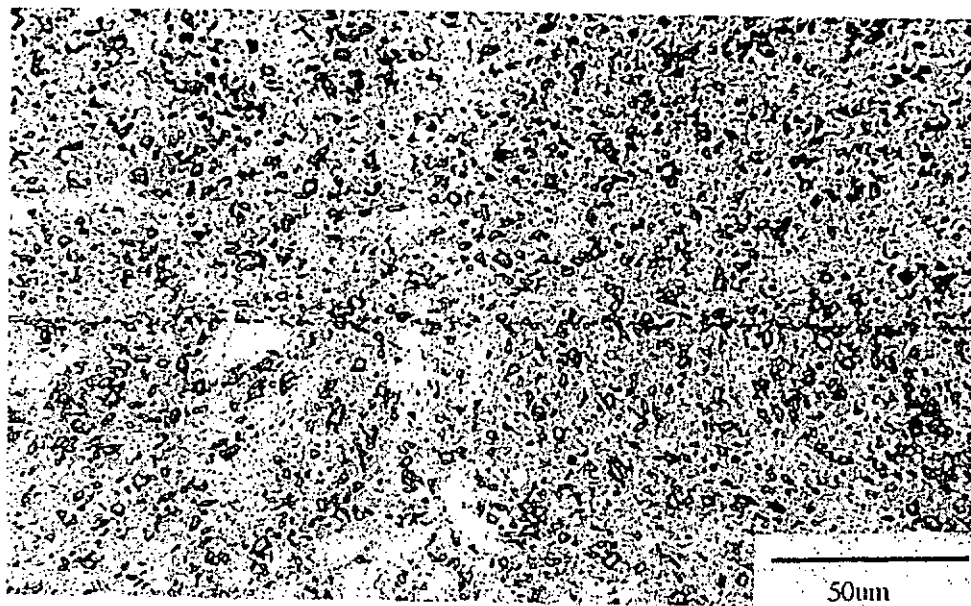Figure 2.8: Section through the bond line of an inertia welded 6061-20% SiCp MMC. Bond line arrowed [5]

Figure 2.9: Diffusion bond of 6061 – 20% SiCp MMC made using Ag interlayer [5]

The processing temperature is lower than that in fusion welding so that reinforcement-matrix reactions are eliminated. For aluminium based composite materials, previous studies also showed that an interlayer will be necessary. The tenacious oxide layer on the surface of the aluminium alloy and the addition of a ceramic reinforcement phase have imposed difficulty on the process. Figure 2.9 shows a diffusion bond in Al-6061/20% SiC composite produced by making use of an Ag interlayer.

2.3 Keyhole Laser welding

When a laser beam is incident on the surface of a sample, part of the energy is absorbed depending on the reflectivity of the material. The absorption of the laser energy by the surface of the material follows the relationship [36]:

$$E(x) = E_0 (1-R)e^{-\alpha x}$$

Where E_0 and $E(x)$ are the laser intensities at the surface and at a depth x respectively, R is the optical reflectivity of the material to laser radiation and α is the absorption coefficient. For metallic surfaces, α is of the order of 10^{-4} to 10^{-5} cm^{-1}, and therefore the energy absorption is limited to a very small depth of 10^{-5} to 10^{-4} cm at the surface. Thus, a point heat source forms on the surface of the material, and the energy is transferred into the material by heat conduction. If the energy is sufficient, melt and vaporization of the surface metal will take place. Increased heat input into the material results in the increased vaporization of the constituents. The vapor pressure and the surface tension gradients in the melt region result in the formation of a keyhole. The keyhole is a cavity filled with vapor or plasma, it behaves like a black body, absorbing most of the incident energy from the laser

beam. Effective absorption of up to 90% is possible in some cases. A high cooling rate is expected around the keyhole. Once a linear heat source is created within the material and energy is distributed along a line through the material, the wall of the keyhole will reach the vaporisation temperature of the material, and around the keyhole molten pool is developed. Due to the movement of the workpiece with respect to the beam, this molten region together with the keyhole will move in the welding direction. As a result, the material at the interface between the liquid phase and the solid phase will melt. The molten material enters the liquid pool, thus building up the weld seam. Figure 2.10 shows the keyhole mode of welding at high laser power intensity.
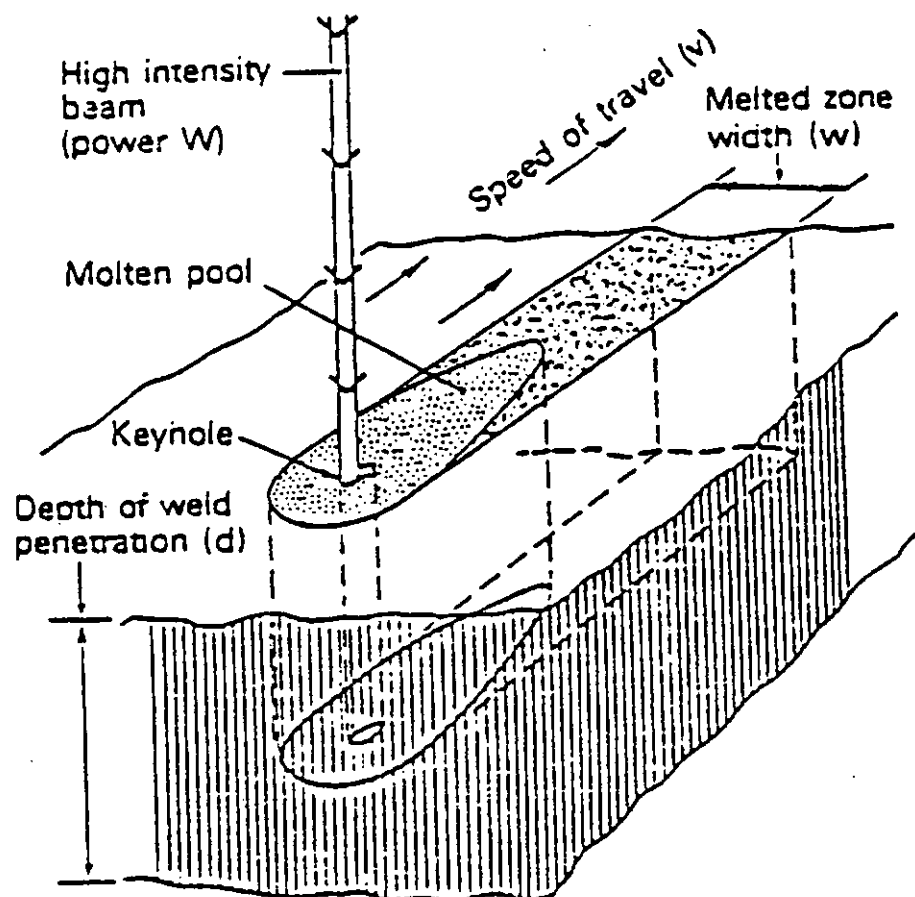

Figure2.10: Keyhole mode of welding at high laser power intensity

Laser keyholing will occur in steel at a power density of about 10^3 W/mm^2. At this level the welds tend to be shallow and wide. In contrast, at power densities in the order of 10^4-10^5 W/mm^2 the welds are deep and narrow, requiring short interaction times, thus promoting high welding speeds [37]. At power densities marginally greater than 10^5 W/mm^2 cutting and drilling regimes are reached and weld metal loss occurs through expulsion of molten and evaporated metal. Nevertheless, excessive power rarely produces blowholes in the weld, especially when welding thin sections at high speed. This is because much of the excess power disappears through the bottom of the keyhole. For other materials such as alloys of aluminium and copper the above welding trends are followed except that these materials do not readily absorb laser light because they are good reflectors.

2.4 Plating of Al based materials

In general, obtaining sound adhesion to aluminum and its alloys has always been a problem for bath platers. Even when accomplished, the bonding is never as good as that obtainable on steel parts. The difficulty arises from the presence of a tight, hard natural oxide on the aluminum surface. The oxide is easily removable by immersing the part in acidic or alkaline solutions, but the oxide immediately reforms when the part is exposed to the air. To overcome this drawback, the bath plater usually removes the oxide in a caustic solution containing either zincate or stannate ions. As soon as the oxide is removed, an immersion deposit of zinc or tin forms, preventing further oxidation. Unfortunately, these methods provide only fair adhesion on relatively pure aluminum, with a loss of adhesion on alloys, particularly those containing substantial percentages of copper and/or silicon.
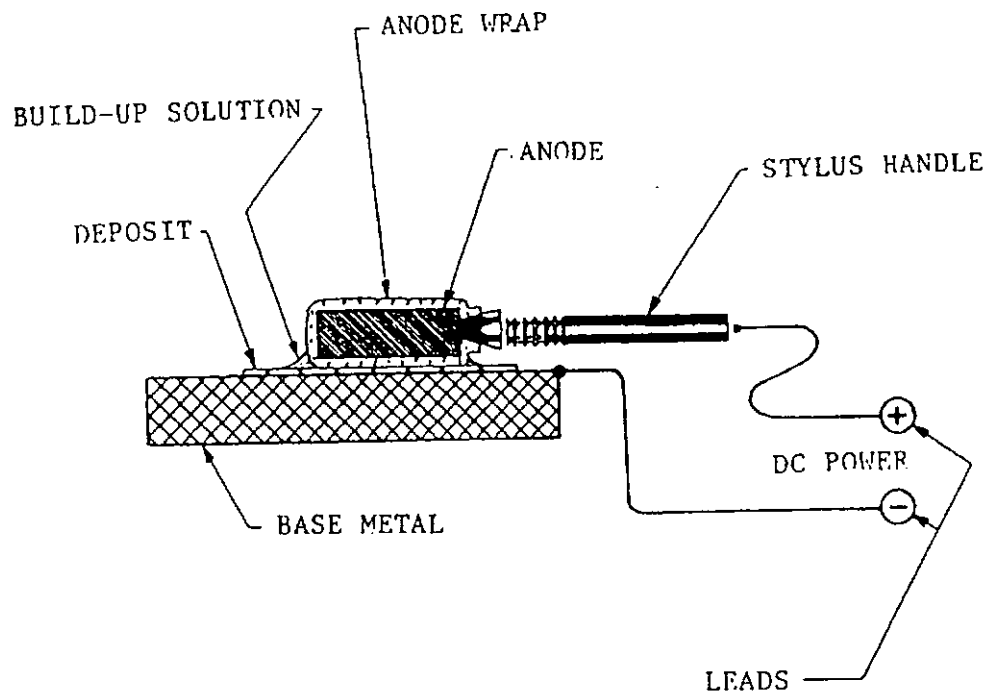
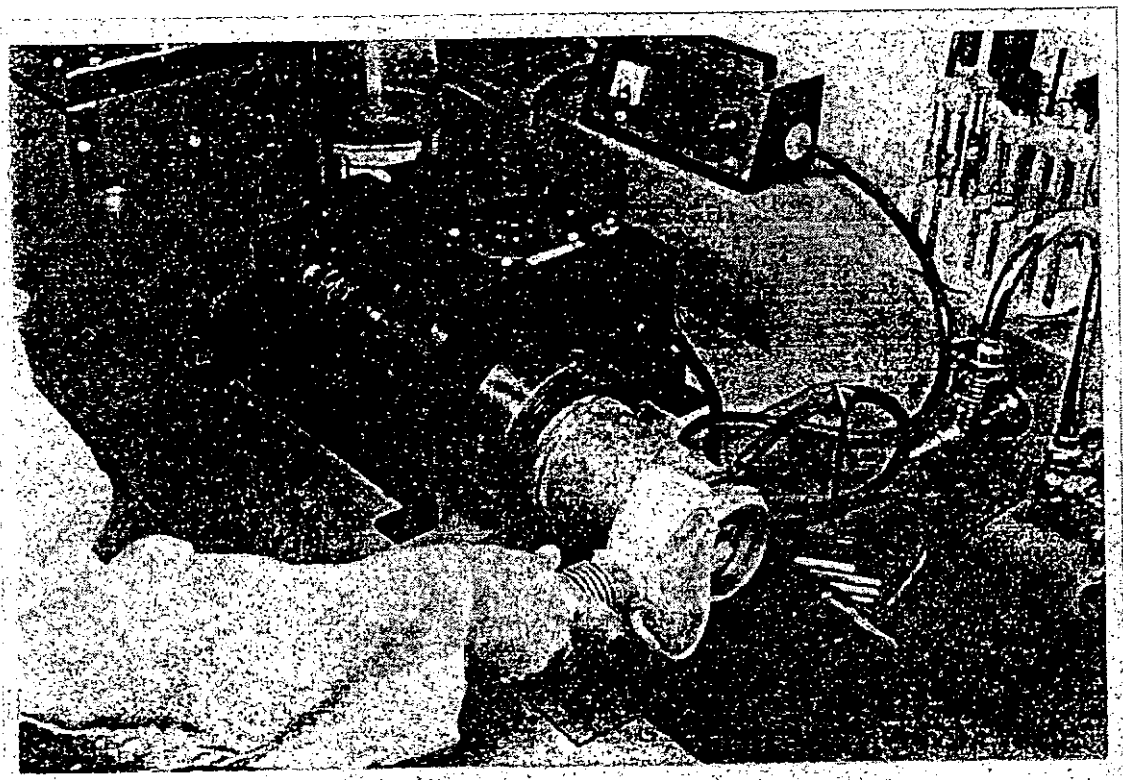Figure 2.11: Schematic of an electrochemical metallizing system

Figure 2.12: A brush plating job in action.

Brush plating can coat some difficult-to-plate metals such as molybdenum, and the interface bonding is good. Brush plating of aluminum alloy has already achieved good results in previous studies [38]. The high metal ion concentration, high electric current, pulse effect, and movement between anode and cathode of brush plating are greatly advantageous to obtain strong bonding. Moreover, the technology is inherently suitable for selective plating which is ideal to be used to plate the joining surfaces only. However, SiC/Al MMCs are much more difficult to be plated than aluminum alloys and not much work has been done in this area. So one of the main aims of the present project is to achieve a good nickel plating on MMC materials.

2.4.1   Brush plating technique

Brush plating is an electroplating technique without immersing the workpiece into plating bath. As can be seen in Figure 2.11, one lead of an electroplating rectifier is connected to the part (cathode); the other lead fits into a tool called a "stylus" or a "plating pen", with an anode of the proper size and shape to contact part of the area to be plated. The anode is covered with a Dacron "jacket" or wrapped with a cotton swab, which is dipped into a special high speed electroplating solution. With the current on, the anode swab is brushed over the area to be coated until the desired deposit thickness has been achieved. The plating thickness can be well controlled by the current density, the velocity of the anode, the flow rate of the electrolyte and the duration of plating. Figure 2.12 shows a brush plating job in action.

Using a minimum of inexpensive equipment, this system enables deposition of nickel, copper, gold, rhodium, cadmium, tin, nickel-tungsten hard alloys, tin-lead solder alloys, or other metals and advanced or unusual materials on small areas. Also

only a limited quantity of plating solution is used, with little or no masking required, without disassembly and without contaminating neighboring components. In brush plating, the rate of deposition is extremely high, sometimes as high as 50 microns per minute. The resulting deposits are relatively hard, low in porosity, very pure, and of high conductivity. Adhesion is excellent and very close tolerance control can be maintained.

A scientific explanation for such a practical improvement over tank-plated deposits is not always easily available, though a surmise is possible. The current densities in brush-plating often run at 1 to 5 A/cm^2, twenty times higher than that used in bath plating. As long as a burning threshold is not reached, operating at high current densities tends towards deposition of very tiny metallic crystals and very fine grained deposits, harder than coarse grained ones. This also partially explains the very low porosity of deposits. A secondary explanation is that the wiping action of the "brush" across the work during deposition wipes away gas bubbles and micro dirt particles which might act as a focus for creation of pores or pin holes. The superior adhesion of brush-plating has a similar explanation [39].

2.4.2 Procedures of brush plating nickel

The process of brush plating includes:

1. Surface preparation;

2. Bonding layer deposition;

3. Build-up layer deposition.

Surface preparation for brush plating normally consists of three steps, they are:

• Precleaning

- Electro-cleaning

- Activating

In pre-cleaning, grease and oil are dissolved with solvents, and rust or tarnish be removed by mechanical techniques such as grinding. Selective electro-cleaning is used to remove fingerprints or light residual oils prior to activation or metal deposition. Activation is very important in brush plating in order to obtain a sound adhesion by producing a fresh and activated metal surface. Different activators are required for different base metals. For aluminium based alloy, Activator #2 is recommended [38]. The major function of Activator #2 in this case is to remove the oxide layer on the surface of aluminium. The two most common bonding deposit solution used are Nickel Special and Copper Alkaline.

Build-up plating is the final step in brush plating whereby the coating will be thickened. For one single metal, for example nickel, there are more than ten kinds of build-up solutions which can produce coatings of different microstructure, inner stress and outlook. It was reported [38] that nickel coatings up to several millimeters had been successfully applied for part repairing.

2.5   Corrosion properties of MMCs

2.5.1   Basics of metal corrosion

Aqueous corrosion is an electrochemical process involving anodic (oxidation) and cathodic (reduction) reactions. Dissolution of metal M (the anodic reaction) is represented by:

$$M \longrightarrow M^{n+} + ne^-$$
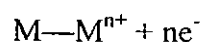
For corrosion to proceed, the electrons of the anodic reaction must be consumed by a cathodic reaction. Oxygen reduction and proton reduction are two predominant cathodic reactions in aqueous corrosion

$$O_2 + 4e^- + 2H_2O \rightarrow 4OH^-$$

$$2H^+ + 2e^- \rightarrow H_2$$
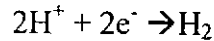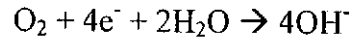
Oxygen reduction can only occur in aerated solution, whereas proton reduction can occur in both deaerated and aerated solutions. A metal or a MMC need not to be immersed in an aqueous solution for corrosion to occur. Water may condense on surfaces at values of relative humidity much lower than 100% because of temperature fluctuations and hygroscopic impurities in the atmosphere or in the metal or MMC. The atmosphere contains impurities such as $NaCl$, SO_2, NO_2, and other salts in concentrations varying with location.

Polarisation diagrams are used to assess the rates of metal dissolution or oxygen and proton reduction. The potential on the vertical axis of the polarisation diagram is a measure of the thermodynamic driving force for the electrochemical reaction. The current on the horizontal axis is a measure of the kinetics of the electrochemical reaction. A typical anodic polarisation diagram of an active-passive metal (eg. Fe, Cr, Ni) is shown in Figure 2.13. In the active regime from the open circuit potential E_{CORR} to the primary passive potential E_{PP}, the metal dissolution rate increases as the potential increases. The dissolution rate decreases at potentials greater than E_{PP} because of the formation of a passive film that protects the metal. At more noble potentials in the transpassive regime, destruction of the passive film or evolution of oxygen results in increasing currents. In some metals, only the active regime is present, while in others, the active regime may not exist. The shape of the

polarisation curve is governed by the metal and the environment. Some aggressive anions, particularly chlorides and other halides, can damage the passive film resulting in pit formation on the metal surface by localised corrosion. On a polarisation diagram, pitting commences at the pitting potential E_{PIT}, which is identified by a rapid increase in anodic current. The pitting potential decreases with increasing aggressive anion concentration, as shown in Figure 2.14
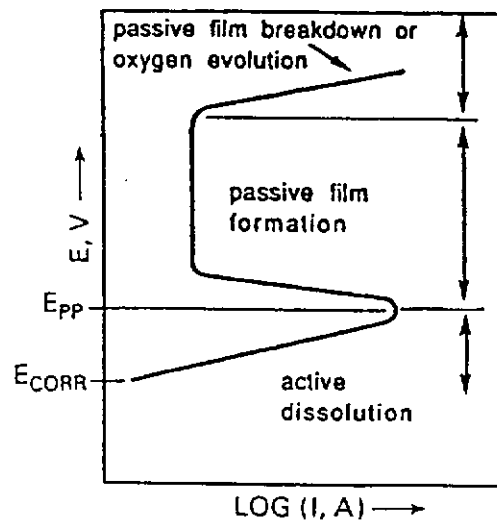

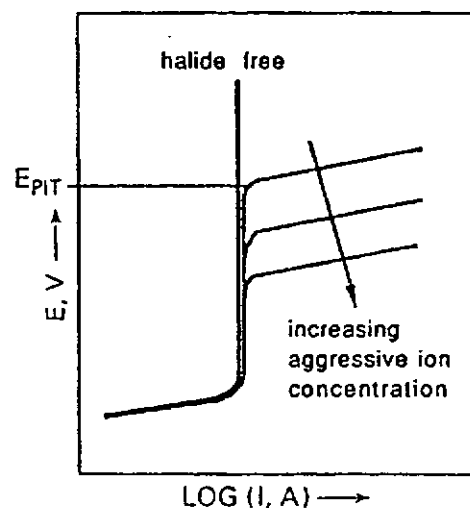Figure 2.13: Anodic polarisation diagram for a typical active-passive metal.

Figure 2.14: Anodic polarisation diagram for a typical passive metal induced to pit by exposure to aggressive ions. [42]

2.5.2 Corrosion of SiC/Al-MMCs

Galvanic corrosion is a primary concern regarding the corrosion behavior of MMCs. This is particularly true when an active metal such as aluminium or magnesium is galvanically coupled to a noble conductor such as graphitte fibre. Relatively inert materials such as graphite, SiC and TiB_2 are usually noble because they serve as inert electrodes for proton and oxygen reduction. Thus, a metal will usually corrode at an accelerated rate when galvanically coupled to a relatively inert material of adequate conductivity.

The electrical resistivity of SiC is dependent on its purity. It ranges from about 10^{13} to 10^{-5} Ωcm [40]. Thus, in the impure state, the resistivity of SiC can be rather low. In aqueous solutions, SiC can serve as an inert electrode for proton and oxygen reduction, and therefore, galvanic corrosion with aluminium is possible. Galvanic corrosion between aluminium and SiC can be significant in aerated chloride containing environments. Lore and Wolf [41] found that the corrosion rate in SiCw/Al-6061 MMCs exposed to chloride containing solutions is proportional to the SiC area fraction. It was reported that 20 vol.% SiC/Al-2024 composite and the monolithic Al-2024 alloy had been exposed to deaerated and aerated 3.5% NaCl. [42] In the deaerated solution, the composite and the alloy corroded at the same rate, which is expected because the galvanic corrosion rate cannot exceed the passive dissolution rate. In the aerated solution, however, the composite corroded about 40% faster than the matrix alloy. These studies showed that the degradation of SiC/Al MMCs in aerated, chloride containing environments was greater than that of the matrix alloys. The accelerated degradation of SiC/Al MMCs was apparently caused by galvanic corrosion between SiC and aluminium, and not by weakening of the passive film.

Various types of coating have been used on SiC/Al MMCs for corrosion protection. Excellent protection was achieved when coatings sealed composites completely [43]. Trzaskoma and McCafferty found that hardcoats increased E_{PIT} of 20vol.%SiC/Al-2024 composite, 20vol.%SiC/Al-6061 composite and Al-6061 alloy. [44] Galvanic corrosion cannot be prevented if SiC protrudes through the hardcoat and serves as a cathode for oxygen reduction. However, if the hardcoat is a poor cathode for oxygen reduction and if it completely covers SiC particles, there is a possibility that excellent corrosion resistance can be achieved.

On the other hand, only limited success has been achieved with anodisation. Some SiCw/Al MMCs that were either sulphuric acid anodised or chromic acid anodised and then exposed to marine environment in the open circuit condition pitted after 30 days exposure. Silicon carbide whiskers protruding from the matrix caused non-uniformities in the anodised layer. Mansfeld and Jeanjaquet reported that a sulphuric anodisation treatment was less effective on SiC/Al MMCs in comparison with their matrix alloys [45].

Several papers reported that in fusion joining of SiC/Al composites, the formation of Al_4C_3 could seriously undermine the corrosion resistance of the base material [21]. It was reported that [20], in the presence of moisture, aluminium carbide decomposed with the release of hydrocarbon gases. However, none of them had presented details of their corrosion tests nor any concrete data on the corrosion properties of the fusion weld was presented. And what is evident is that very little information is available concerning the corrosion behaviour of fusion welds of MMC materials.

# Chapter 3. Experimental Details

3.1 The composite material

The composite materials used in this study was a SiC 17.8 Vol% particle reinforced Al-Cu alloy (2124) MMC, which was manufactured by BP Metal Composites Limited. Typical particle size of the reinforcement phase is 1-3μm. Figure 3.1 (a) and (b) show the microstructure of the as received material. Rolling elongation can be clearly observed in the low magnification figure. Nominal chemical composition of the matrix material is listed below in Table 3.1.

Table 3.1   Chemical composition of the matrix alloy - Aluminium alloy 2124 (wt%)

Cu	Mg	Mn	Fe	Zn	Si	Cr	Zr&Ti	Total Others	Al
3.8-4.9	1.2-1.8	0.3-0.9	0.30 max	0.25 max	0.20 max	0.10 max	0.20 max	0.20 max	Remainder

Samples for laser welding were cut from a 2.5mm thickness hot rolled sheet. A typical microstructure of the composite is shown in Figure 3.1. Stringers of SiC particles were found in-line with the rolling direction. Welding coupons of the dimension of 50mm×25mm×2.5mm were wire-cut for the bead-on-plate and square butt welding experiment.

The welding surfaces were prepared by fine grinding on 600 grit size emery paper then ultrasonically cleaned. Sections of the weld beads for metallographic examination were obtained using wire-EDM.
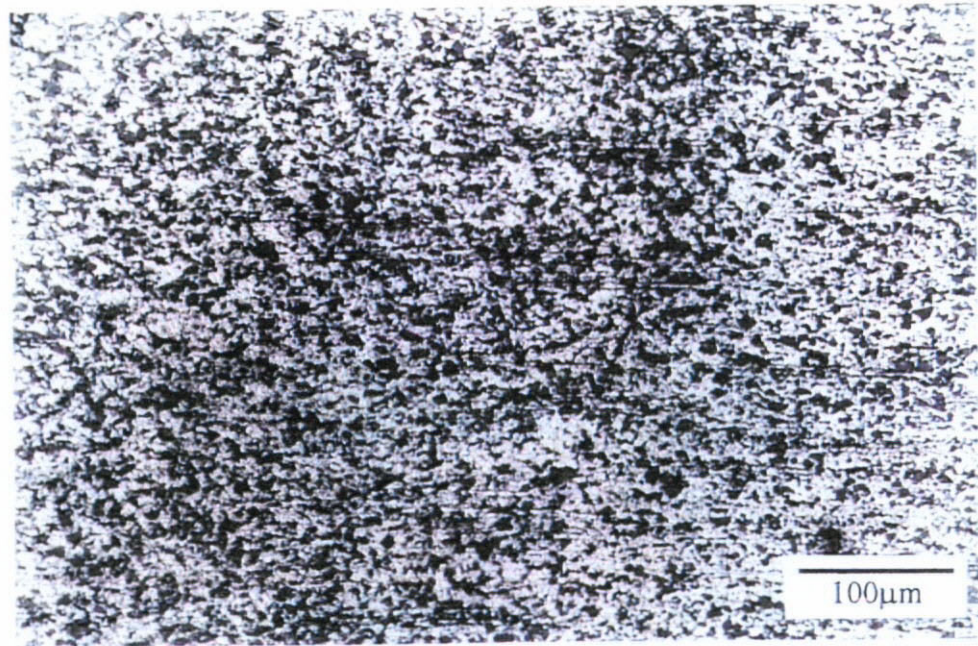
(a)
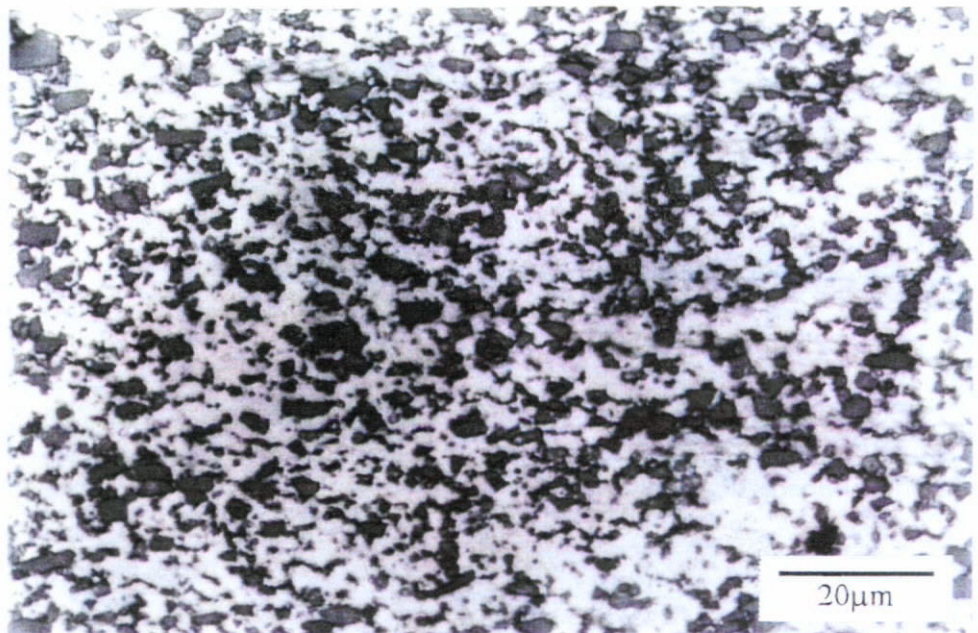
(b)

Figure 3.1: As received microstructure of the SiC$_p$ 17.8 Vol% Al-2124 MMC.
(a) low magnification; (b) high mignification.

3.2 Brush plating

Brush plating technique was selected as a pre-welding treatment for the MMC material. A number of procedures were experimented in order to attain a good nickel-MMC interface. Two sets of procedures are reported in this study. Their difference is on the use of different activation techniques. Activation Procedure 1# is a ready proven technique valid for the Al-2124 alloy. Procedure 2# is an improved process for high silicon content Al-alloy. Although Copper Alkaline has a pH value close to 7, the acidic Nickel Special was chosen as the bonding solution because nickel was the build-up metal. Nickel Alkaline was chosen as build-up solution because it produces compact coating. The plating procedures employed are listed in Table 3.2.

Table 3.2   Procedures of nickel brush-plating

Procedure	Procedure 1#	Procedure 2#
Electro-clean	• Electroclean at 5 to 8 SMPM (Speed in Metre Per Minute) at 8 to 10 volts for 10 to 15 seconds, polarity +; • Rinse;	
Activation	• Activator #2 at 5 to 8 SMPM at 10 volts for 20 to 30 seconds, polarity -; • Rinse;	• Activator #2 at 5 to 8 SMPM at 10 volts for 15 to 20 seconds, polarity -; • Rinse; • Activator #3 at 10 to 15 SMPM at 14 volts for 3 to 5 minutes, polarity -; then at 8 volts for 30 second, polarity +; • Rinse;
Bonding Layer	• Deposit bonding layer of Nickel Special to approximate 5 microns at 5 to 8 SMPM at 12 volts; • Rinse;	
Build-up Layer	Deposit build-up layer of Nickel Alkaline at 5 to 8 SMPM at 10 volts until desired thickness.	

3.3 Laser welding experiment

3.3.1 Experimental setup

Laser welding was accomplished using a Multiwave Nd-YAG laser ($1.06\mu m$ wavelength) which was capable of operating at a maximum average output power of 2kW. The laser beam was delivered to the workpiece by means of an optical fibre. (Figure 3.3) The focal length of the final focusing lens was 100mm, with such an arrangement a focal spot diameter of 0.5 mm was achieved. During welding the focal spot was focused on the surface of workpiece. The design of the laser head nozzle permits the flow of pure argon at approximately 10 l/min in a coaxial direction to protect the molten pool from excessive oxidation during welding. A fixture was employed to hold the sample in position and prevent it form deformation during welding. See Figure 3.2.
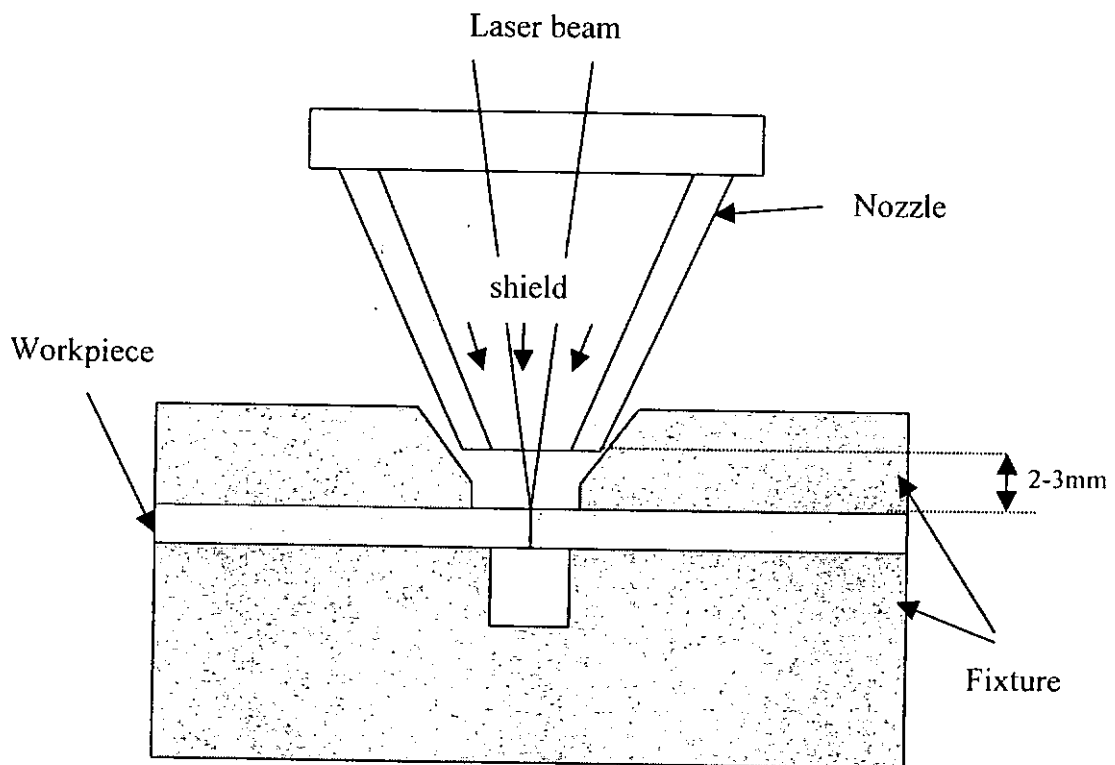

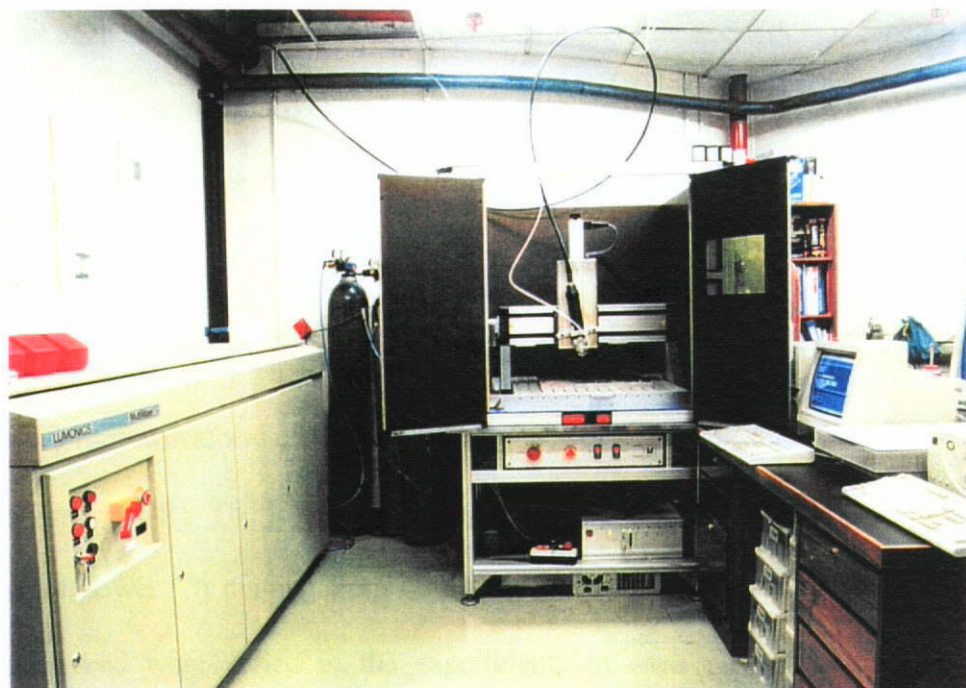Figure 3.2: Nozzle and fixture setup for the laser welding experiment.

Figure 3.3: The 2kW Nd:YAG laser with optical fibre beam delivery system.

A computer controlled X-Y table was used to move the laser head including the focus lens, the nozzle and the optic fiber. The minimum beam waist position was determined as the focus point of the Nd:YAG laser beam. To locate the focus point, a series of burns was produced by 20ms single shots on a stainless steel sheet with the laser head raised in 0.1mm steps each time. The size of the burns were then measured using a microscope. In a series of burn, if the diameter gradually decreased and then increased, the smallest burn position represented the focus point position. On the other hand if the diameter of the burn continued to get smaller or larger, the exercise was repeated with the laser head position raised or lowered. A power meter was employed to calibrate the laser mean output power regularly.

3.3.2 Laser welding of MMCs at various parameters

The experimental approach involved bead-on-plate welding of the MMC using three different waveforms, namely: continuous-wave (CW), sine-wave (SIN), and square-wave (SQR). The laser output parameters were varied in the experiment with the output power (P) ranging from $600W$ to $1400W$, the pulse frequency (f) and the welding speed were varied in the experiment. At each power level and output waveform, four welding travelling speeds in the range of 20 to 40 mm/sec were used to obtain partial to full penetration bead-on-plate welds. Figure 3.4 and Table 3.3 present the conditions of the five different modes of waveforms used in the experiment. The other laser welding parameters are listed in Table 3.4
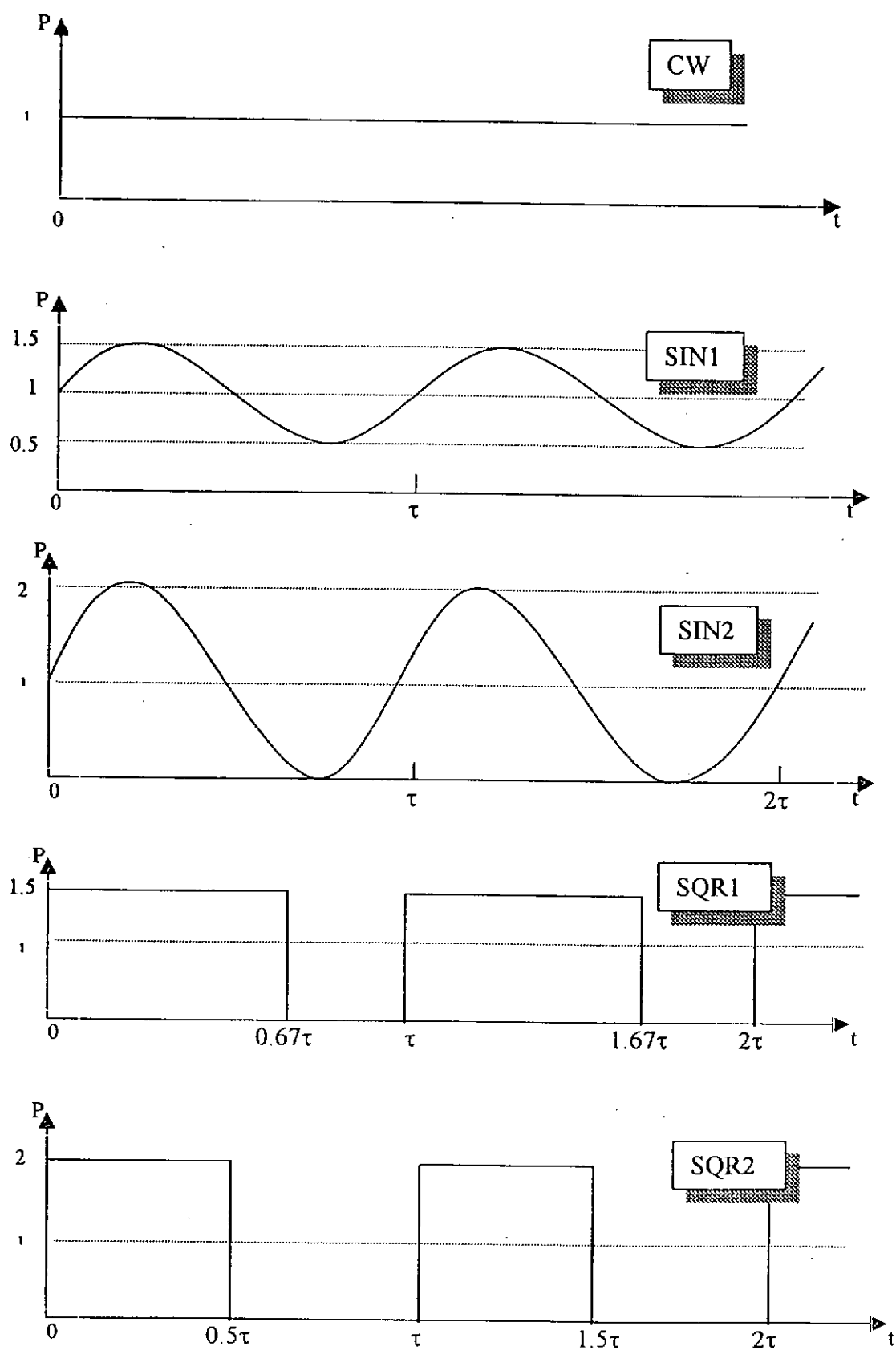
Let mean power = 1; pulse duration = τ

Figure 3.4: Illustration of experimented laser output waveforms

Table 3.3   Laser output waveforms

Waveform No.	Description	Peak power:Mean Power
CW	continuous wave	1:1
SIN1	sine wave with 150% peak power	1.5:1
SIN2	sine wave with 200% peak power	2:1
SQR1	square wave with 150% peak power	1.5:1
SQR2	square wave with 200% peak power	2:1
SQR3	square wave with 150% peak power	2.5:1

Table 3.4   Laser processing parameters:

Frequency:	100Hz, 200Hz, 300Hz, 400Hz, 500Hz
Mean power:	600W, 800W, 1000W, 1200W, 1400W
Traverse speed:	20, 25, 30, 35,40mm/s
Focus position:	On surface
Focal spot size (a)	0.5mm
Shielding gas:	Argon, 10 l/min

3.3.3 Laser welding of nickel plated MMCs

A pre-welding treatment of brush plating of nickel on the joining surfaces is used as a means to stop the formation of carbides in the weld zone. In this case, butt-joint welding is performed on the nickel plated samples using a sine-wave laser output. The conditions of the welding samples together with the welding conditions are presented in Table 3.5 and Table 3.6 respectively.

Table 3.5   Conditions of the samples for butt-joint welding

Sample1#	MMC with 0.15mm thick Ni plating
Sample2#	MMC with 0.2mm thick Ni plating
Sample3#	MMC with 0.25mm thick Ni plating
Sample4#	MMC without Ni plating

Table 3.6   Laser processing parameters

Output waveform:	sine
Frequency:	100Hz
Peak power/Average power:	200%
Average power:	600W, 800W, 1000W, 1200W, 1400W
Traverse speed:	30mm/s
Focus position:	On surface
Focal spot size (a)	0.5mm
Shielding gas:	Argon, 10 l/min

3.4   Measurement

Cross-sections of the welds were examined using an optical microscope together with an image analyser to determine the weld penetration depth, the bead width and the amount of porosity. At least three sections were examined for each weld and an averaged result was obtained for each measurement. For the nickel plated samples, EDX elemental analysis was employed to determine the types of metallic compounds founded at the Ni-MMC interface.

3.5   Corrosion Test

Some of the butt-jointed welded specimens were sectioned and prepared for corrosion testing. The section of weld was polished down to 1μm diamond paste. An unmasked region of 2mm wide which contains the weld zone was subjected to anodic polarization tests. Anodic polarization tests were carried out in a 3.5wt% NaCl solution which was prepared using analytical grade reagents. The initial pH value of the solution was 5.7. The specimens were driven from a (Ecorr-250mV) to -250mV or +200mV at a scanning rate of 1.0mV/s to produce potentiodynamic polarization plots. Initial delay of 1000 seconds was applied to guarantee stable test results. All potentials were measured with reference to a standard calomel electrode (SCE). The corroded surfaces were examined by SEM and EDX to explore the corrosion properties of the samples.

CHAPTER 4.   RESULTS AND DISCUSSION

4.1   Microstructure of Laser Welded MMC

4.1.1   Typical Weld Microstructure

A typical cross-section of a laser weld shown in Figure 4.1 reveals that broadly speaking the weld consists of two regions: the central fusion zone A and the partially melted zone B. In zone A, all the SiC particles were found to have been completely dissolved and a large amount of plate-like precipitates were found (Fig. 4.2). The plate-like phase has been identified by previous researchers [28] to be the Al_4C_3 phase (discussed in chapter 2). Other major phases present in zone A are re-solidified aluminium alloy and primary silicon particle. It was found that the width of zone A was close to the spot size of the laser beam which in this study was 0.5mm.

When the laser beam struck the composite surface it started to melt and very quickly a vapour channel, i.e. a keyhole, was formed below the interaction point. Soon after the keyhole was initially formed the material around was heated up to a very high temperature due to the Fresnel and the inverse bremsstrahlung absorption effects. The aluminium alloy was melted first and at the same time SiC would start to dissociate. At a temperature just below the vaporisation point of aluminium all SiC particles were believed to have been totally dissolved. As a result, a homogeneous liquid containing Al, Si, and C was formed. According to Kavali [46], the molten material would flow in a turbulent manner, and the liquid was pushed out to the rear side of the established keyhole (opposite to the direction of the laser beam, see Figure 4.5) forming a convection area. The established keyhole was
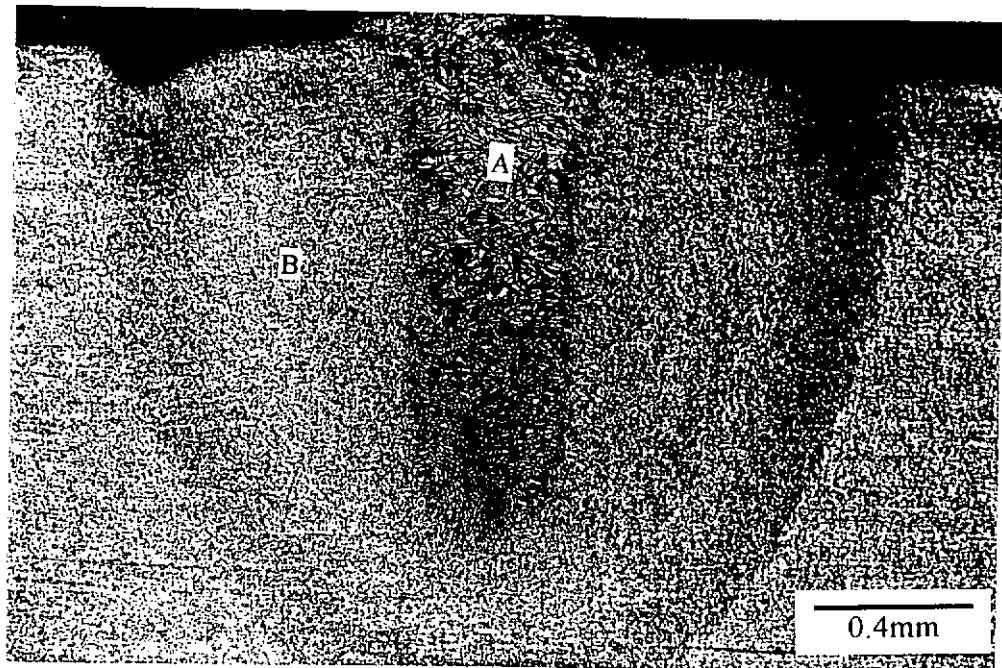
- 41 -

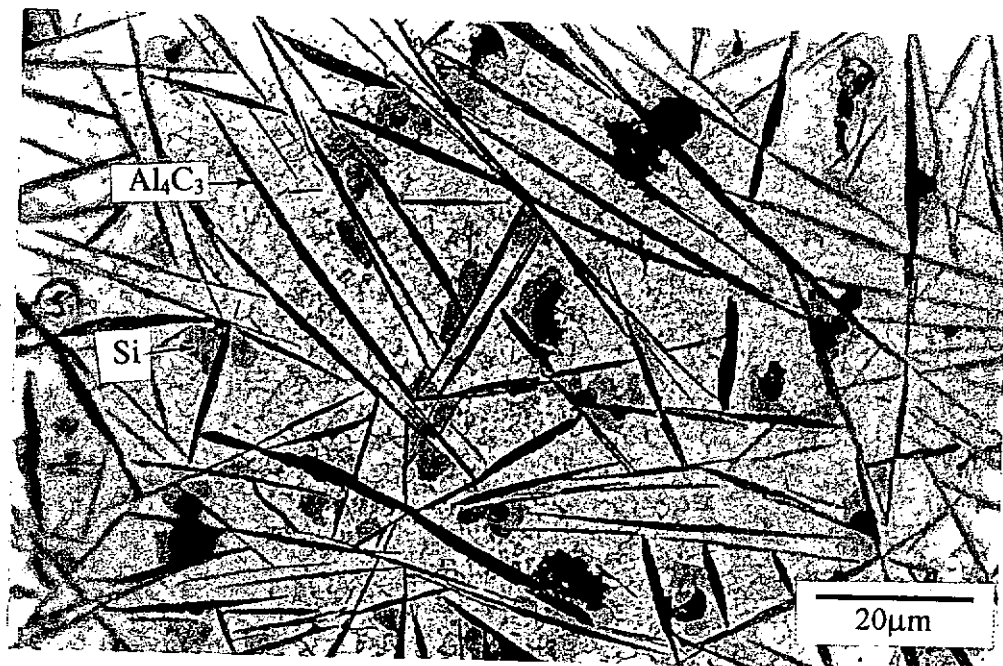Figure 4.1: A typical cross section of a laser weld
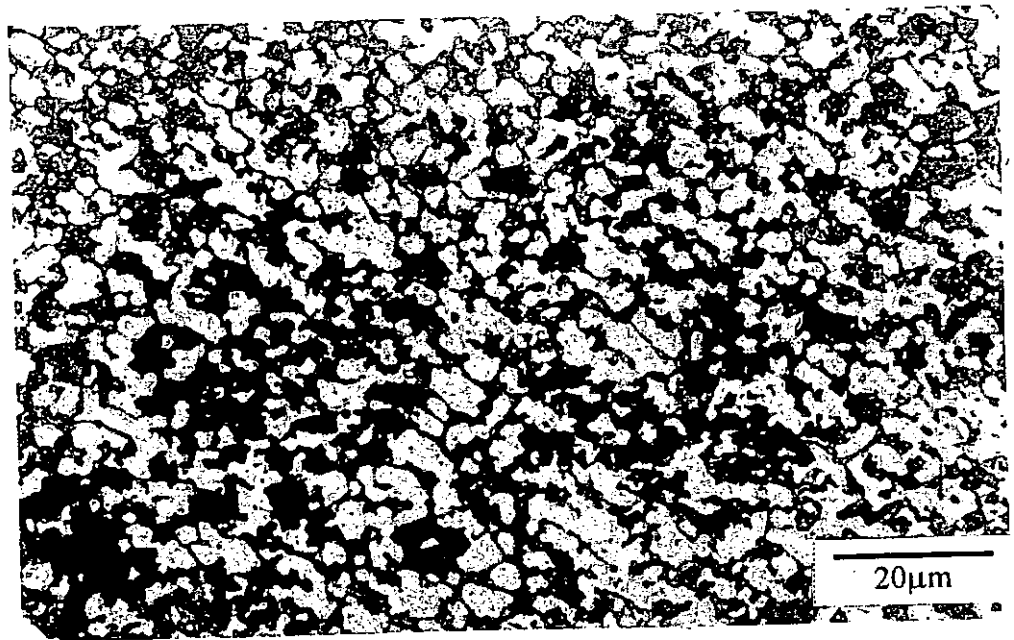

Figure 4.2: Microstructure of zone A

Figure 4.3: Microstructure of zone B
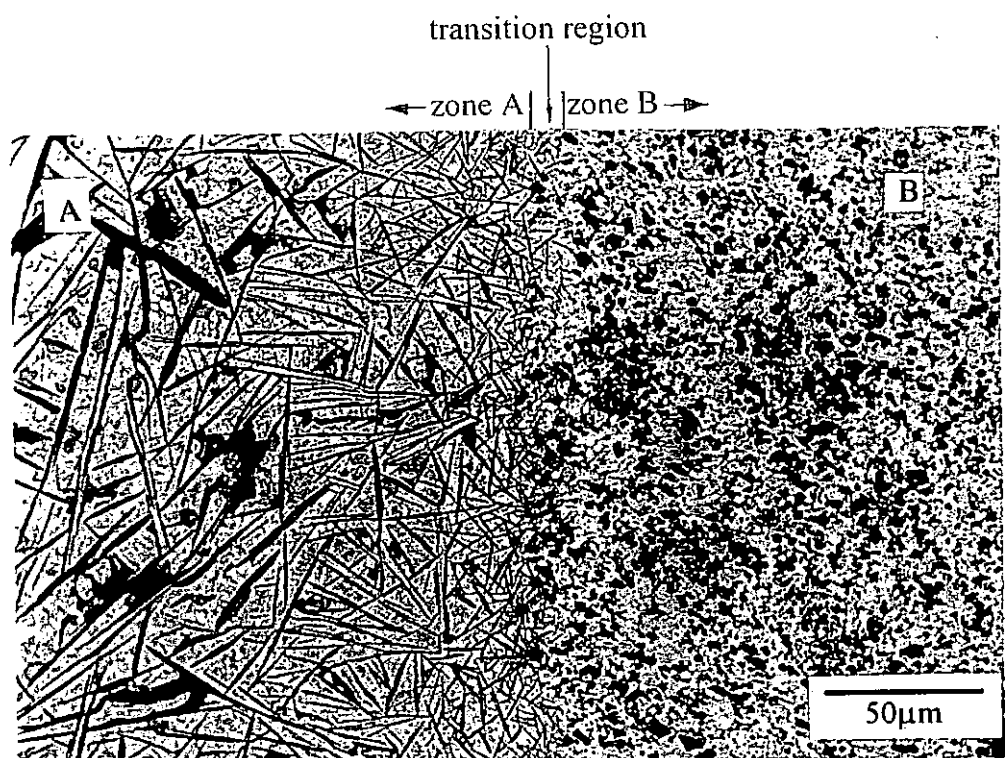
transition region

←— zone A | |zone B —→

Figure 4.4: Interface between zone A and zone B

stabilised by the balance between the vapor pressure and the surface tension of the liquid metal, or could even by the gas pressure of the plasma. As the laser beam was moved away the expelled molten material would refill the keyhole and re-solidify, thus zone A was formed. During the cooling down period a large amount of Al_4C_3 precipitates were formed in zone A. The dissolution of SiC was likely to happen below the melting temperature of SiC (2700°C-2927°C) and was believed to occur between 1404°C and 2467°C [47]. It was because the former temperature is the lowest eutectic temperature of the Si-C phase diagram and the latter is the vaporisation temperature of aluminium.

Meanwhile, as heat was conducted away from zone A, the matrix material in the vicinity area was melted however the SiC particles remain largely undissolved. After re-solidification, the matrix material clearly displays a dendritic structure, (Fig. 4.3) which confirmed that the matrix material was melted during welding. The elongated stringers of SiC particles as found in the as-rolled structure still remains, (see figure 4.1) which suggest that no convection has happened in zone B. The reason why the partially molten material in zone B was not expelled when the keyhole was formed could be attributed to its extremely high viscosity. In zone B, no plate-like Al_4C_3 was observed. Although there was a transition region between the interfaces of zone A and zone B (Fig.4.4) where SiC particles were partially melted, the region was relatively narrow and was in the order of 20μm. The complete dissolution of SiC happened only in zone A which was similar in size to that of the keyhole. Although, it has been suggested that the formation of Al_4C_3 would proceed if the processing temperature exceeds 730°C [12], the experimental results of the present study show that only when the SiC particles were completely dissolved in the molten aluminium matrix no extensive amount of plate-like Al_4C_3 phase would

form. This must be due to the inherent extremely short laser/material interaction time of the laser welding process.
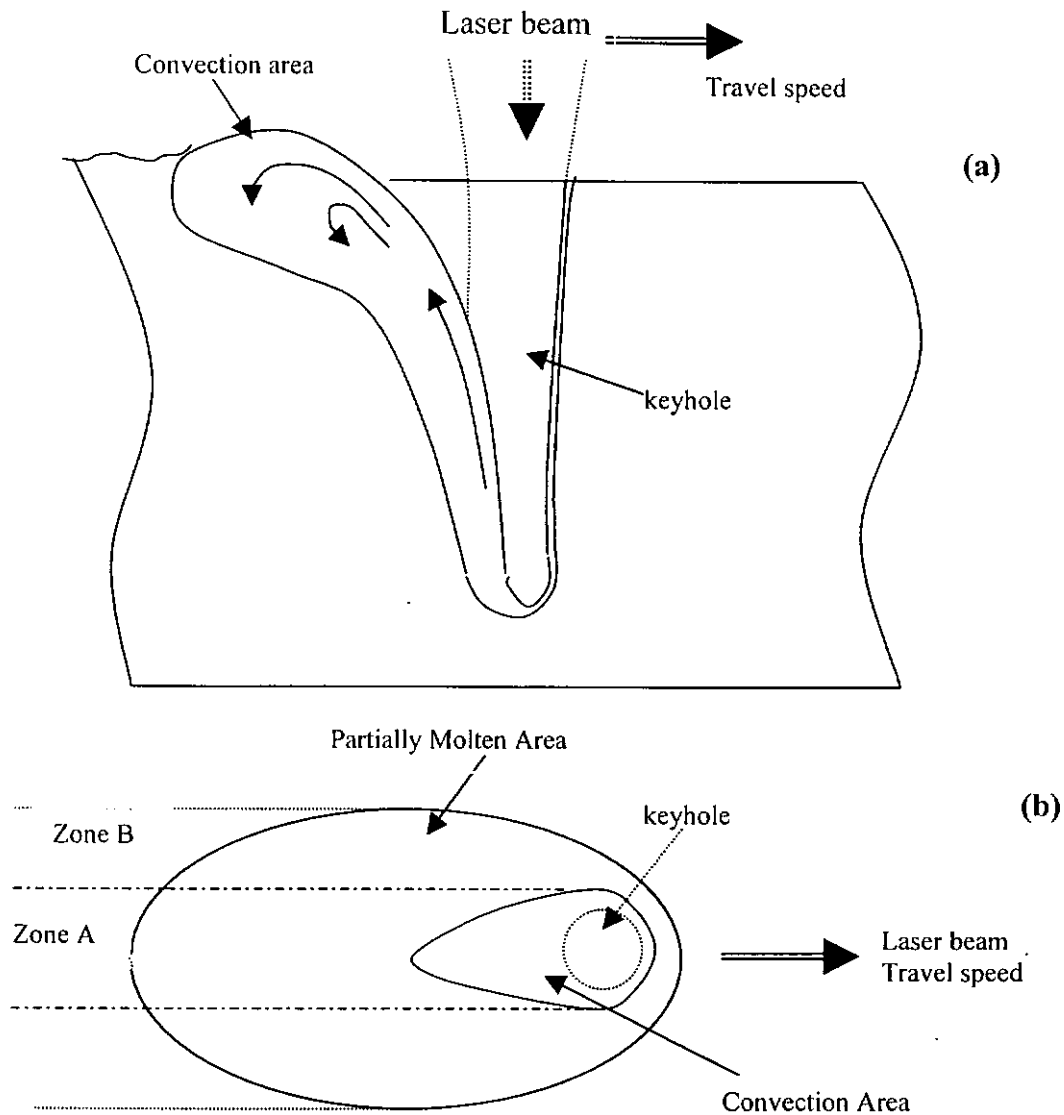

Figure 4.5: Keyhole laser welding of SiC/Al MMC. (a) cross section; (b) top view.

4.1.2 The Effects of Laser Output Waveform on Weld Microstructure

Typical cross-sections of the welds produced using the five different waveforms (CW, SIN1, SIN2, SQR1, SQR2) are shown in Figures 4.6(a)-(e). These figures show that the size of the Al_4C_3 phase decreased of the order of CW > sine-wave > square-wave. Although the size of Al_4C_3 could be reduced by employing a

square wave operated at high peak powers, it still would not be possible to eliminate the carbide phase just by varying the laser parameters and the output waveform. The kinetics of the reaction and the morphology of the compound itself are undoubtedly time dependent. Therefore, not only should the laser peak power be considered as an influential factor in controlling the formation of aluminium carbides, but pulse duration also affects the extent to which the reaction occurs.

Figure 4.7 shows the effects of waveform and mean power on the amount of porosity in the weld. The results show that using square-wave had produced a substantial amount of porosity in the weld. Whereas, continuous-wave and sine-waves produced much less porosity. In the case of square-waves, the laser power shut down abruptly at the end of the pulse-on-period, therefore the cooling rate of the weld would be much higher than that as in the cases of CW and sine-wave. It can be concluded that the solidification time was shorter than the pulse-off-period, in this case, was between 3.3 to 5ms. Because of the high viscosity of the MMC material, some trapped gas would not have enough time to escape and to be remained inside the weld. As the mean power was increased, the amount of porosity was found to have decreased. This could be due to the fact that more energy was input into the weld, and as a result the cooling rate was reduced. On the other hand, the laser power of the sine-wave declined gradually, so that any gas produced would have more time to escape. The effect of welding speed and pulse frequency on the amount of porosity formed in the weld are presented in Figures 4.8-4.9. The results indicate that using a higher welding speed the amount of porosity formed in the weld was increased. This was more so for the square-wave welding condition. Again this was believed due to insufficient time was allowed for the gas to be escaped from the weld zone. On the other hand, in the case of square-wave the amount of porosity
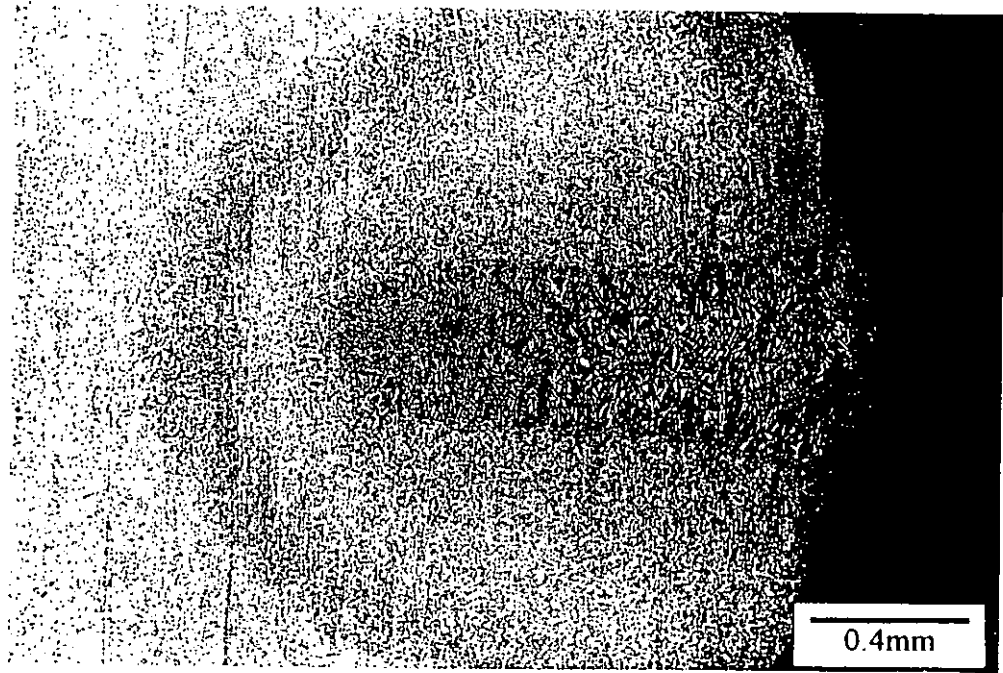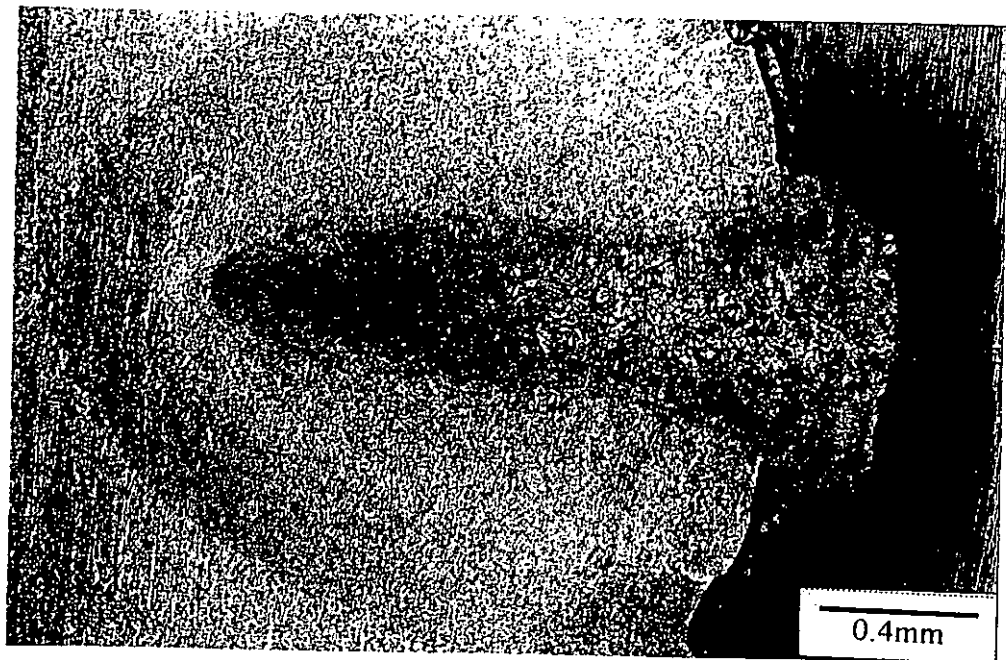
Figure 4.6 (a)
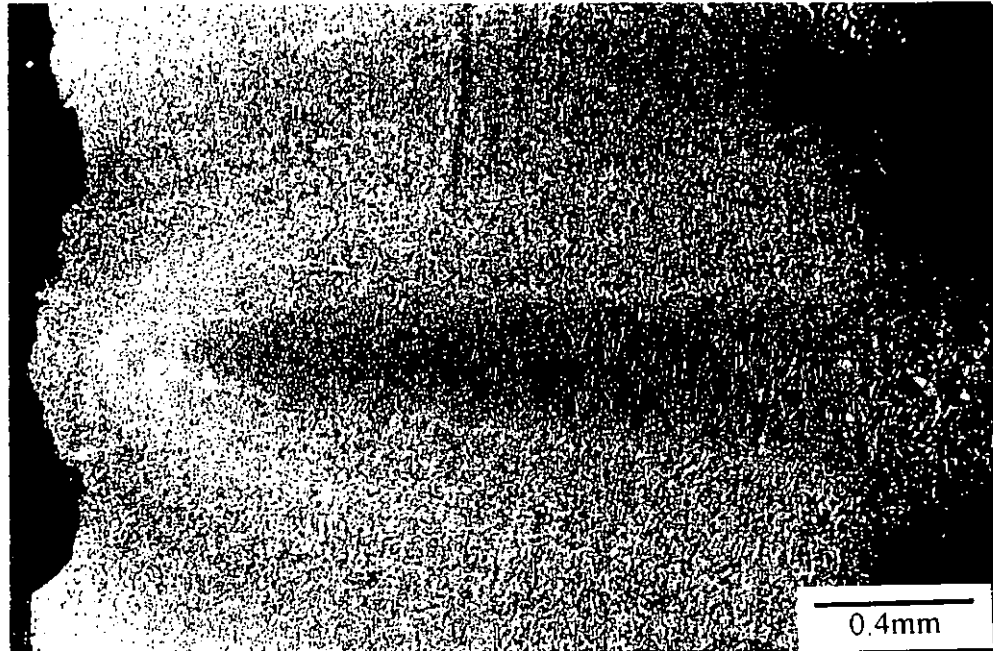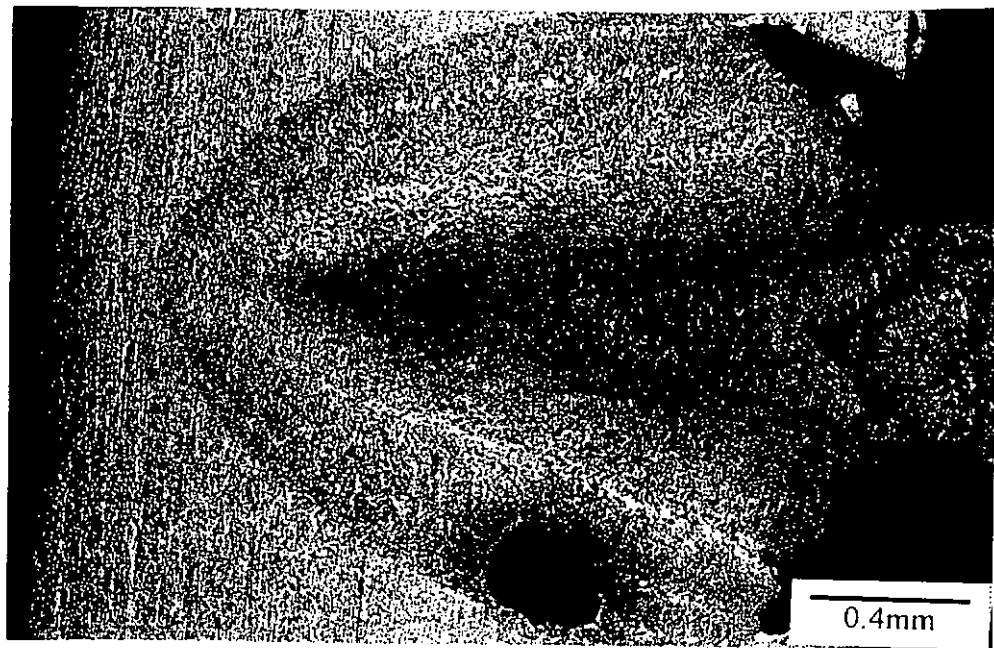

Figure 4.6 (b)

Figure 4.6 (c)

Figure 4.6 (d)

(e)

Figure 4.6: Cross-section of laser welds produced by different laser output
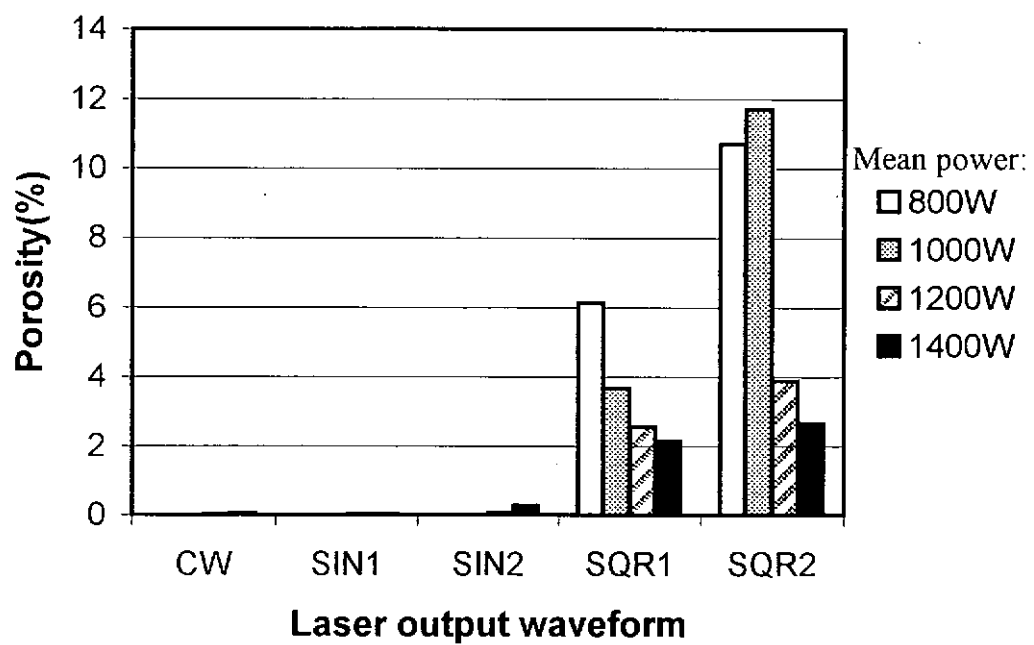waveforms. (a) CW; (b) SIN1; (c) SIN2; (d) SQR1; (e) SQR2.

Figure 4.7: Effects of waveform and mean power on the amount of porosity.
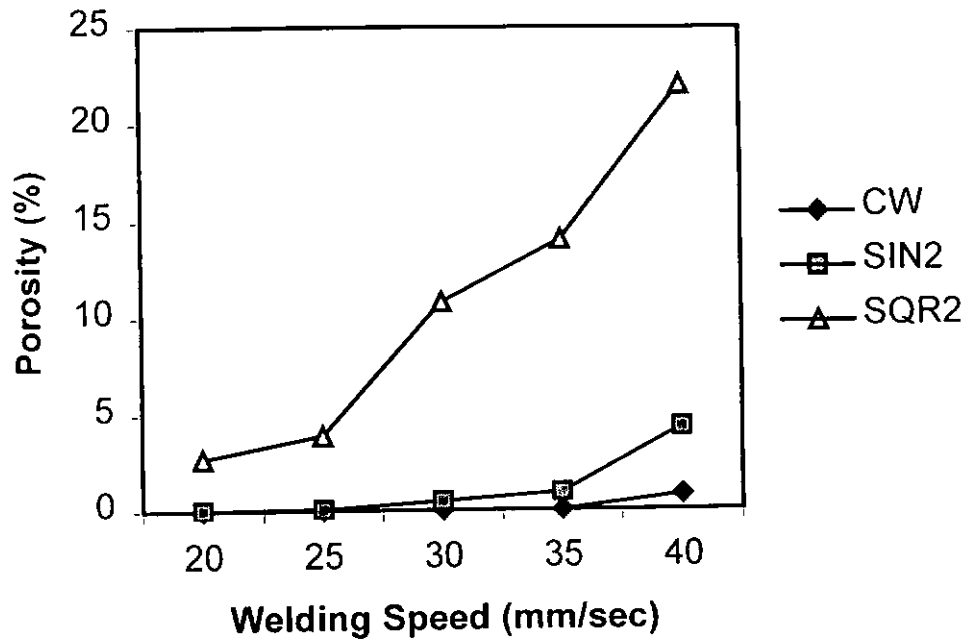(welding speed = 25mm/s, pulse frequency = 100Hz)

Figure 4.8: Effect of welding speed on the amount of porosity.
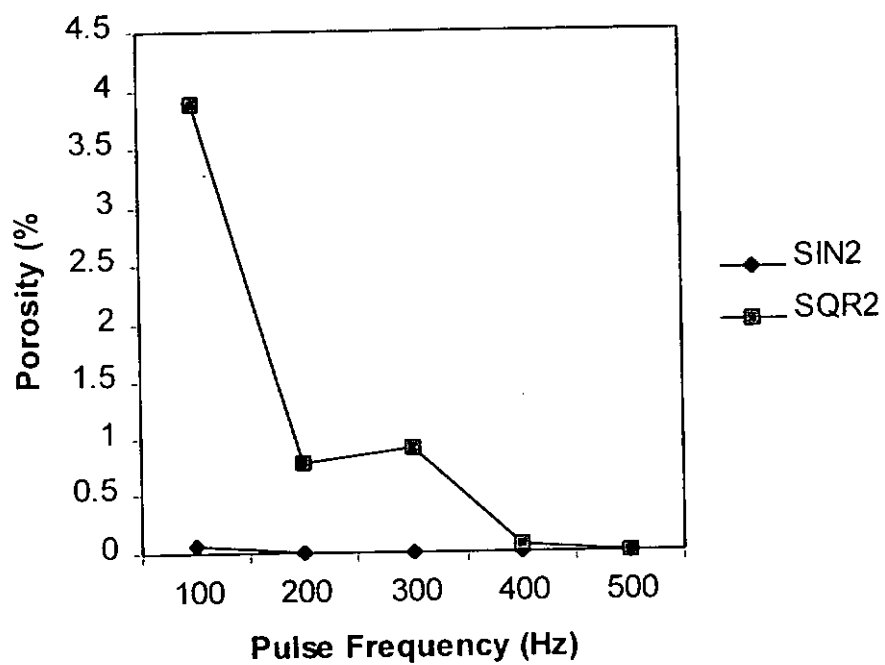(mean power = 1200W, pulse frequency = 100Hz)

Figure 4.9: Effect of pulse frequency on the amount of porosity.
(mean power = 1200W, welding speed = 25mm/s)

dropped dramatically as the pulse frequency was increased to above 200Hz. Now, at these high frequencies where the pulse-off-time was less than 2.5ms the weld was not totally solidified before the next pulse came on. As a result a longer time was allowed for the gas to escaped.

4.2   The Effects of Laser Outputs on Weld profile

4.2.1   Constant Welding Speed and Pulse Frequency

The effects of mean power, peak power and the laser output waveform on the depth of zones A and B are shown in Figures 4.10 and 4.11. In these cases the welding speed and the pulse frequency were kept constant at 25m/s and 100Hz respectively. A comparison of the results of SIN1, SIN2, SQR1 and SQR2 shows that at the same mean power, a higher peak power produced a greater depth-of-penetration. Whilst, at the same mean power and peak power, the square wave produced a deeper weld than the sine-wave did.

The effect of peak power (i.e. pulse energy/pulse duration) on weld penetration clearly shows that the depth-of-penetration increased as the pulse duration was reduced and this was true for the two pulsed waveforms studied. The adverse effect of long pulse duration on the depth-of-penetration was believed due to a higher proportion of heat conducted laterally into the specimen.

The effects of mean power, peak power and the laser output waveform on the width of zones A and B are shown in Figures 4.12 and 4.13 respectively. The result shows that the width of zone A changed very little as the mean power and the laser output waveform were varied. The width of zone A normally lies between 0.45mm to 0.5mm. The width of zone A was believed closely related to the focus size of the
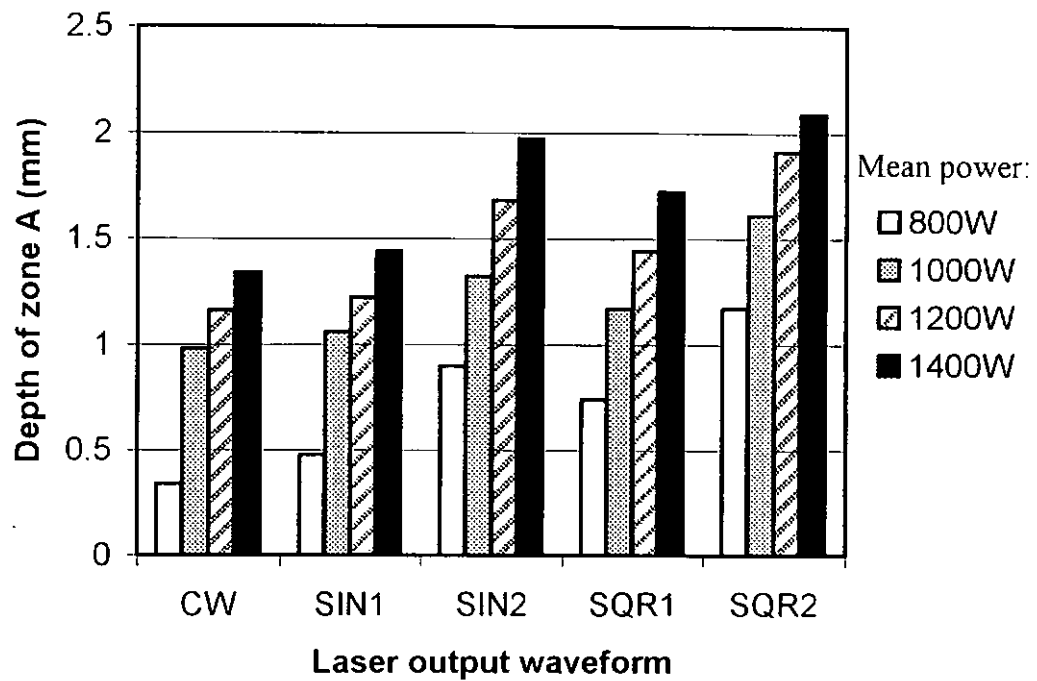
Figure 4.10: Effects of mean power and laser output waveforms on depth of
zone A. (welding speed = 25mm/s, pulse frequency = 100Hz)
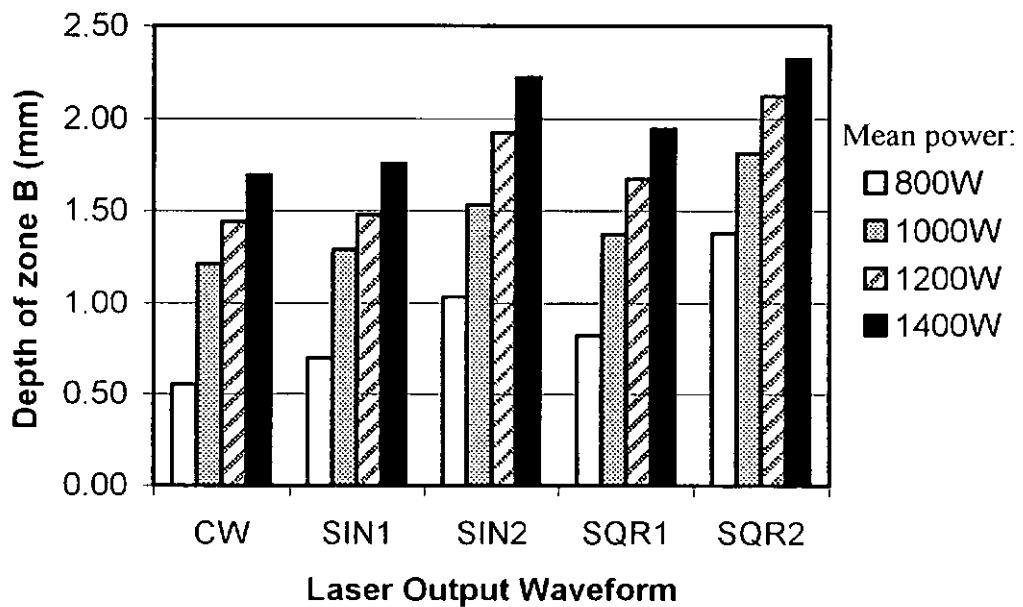

Figure 4.11: Effects of mean power and laser output waveforms on depth of
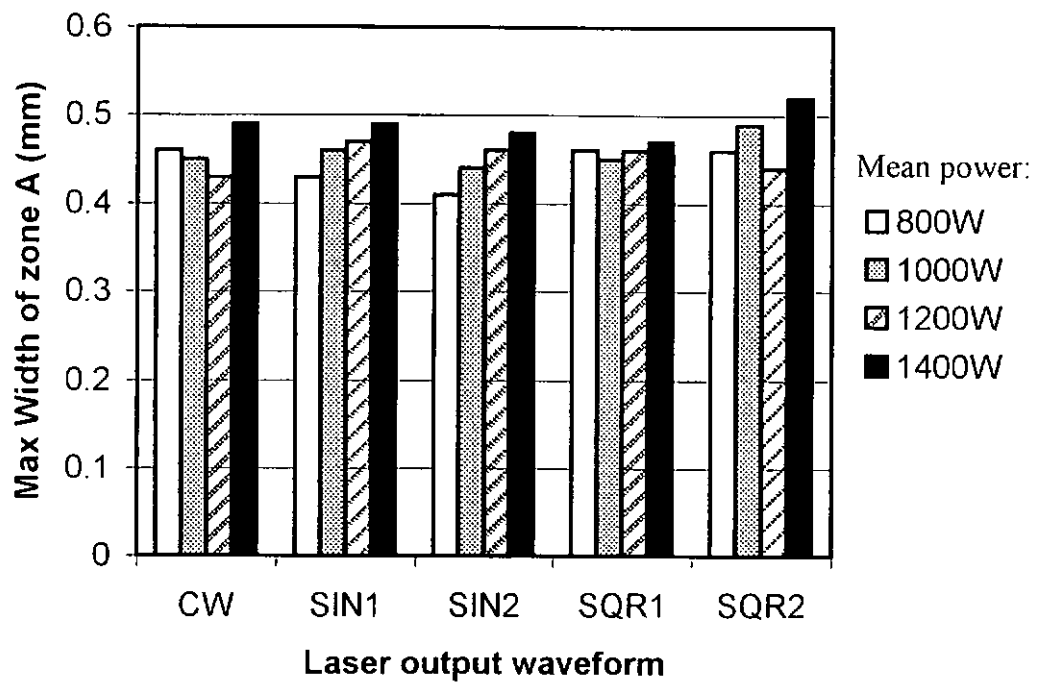zone B. (welding speed = 25mm/s, pulse frequency = 100Hz)

Figure 4.12: Effects of mean power and laser output waveform on width of zone A. (welding speed = 25mm/s, pulse frequency = 100Hz)
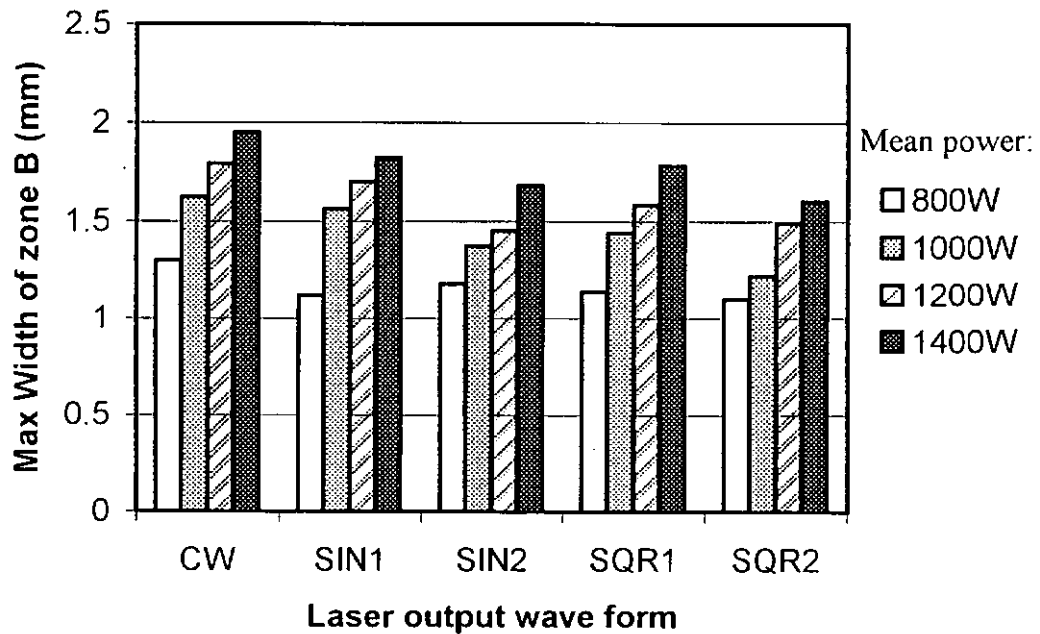

Figure 4.13: Effects of mean power and laser output waveform on width of zone B. (welding speed = 25mm/s, pulse frequency = 100Hz)

laser which in this study was 0.5 mm. The results thus indicate that in order to minimise the size of zone A, the spot size of the laser beam needs to be reduced. On the other hand, the mean power has a more pronounced effect on the width of zone B. This was due to the fact that unlike zone A, the formation of zone B was thermal conduction related. Increasing the mean power would mean an increase of the total heat input to the weld, therefore a larger molten area (zone B) was produced. Also for a fixed mean power condition, a deeper weld penetration means that a smaller zone B will be obtained.

4.2.2 Effects of Welding Speed and Pulse Frequency

The effect of welding speed on the dimensions of the weld for different waveforms: CW, SIN2 and SQR2 are shown in Figure 4.14 to Figure 4.17. In these cases the mean power and the pulse frequency were kept constant at 1200W and 100Hz respectively. In the case of CW, the depth of the weld decreased as the welding speed increased. This was expected since the laser dwelling time was reduced as the welding speed was increased. On the other hand, for the cases of pulsed welding the effect of welding speed on the depth-of-penetration was not significant. In these cases, since the solidification time of the weld was considered to be shorter than the pulse-of-time. As a result, every pulse was acting quite independently from each other. When the next pulse was on the weld would have been solidified already, therefore the welding speed (or the overlapping coefficient) has little effect on the depth-of-penetration.

The effect of pulse frequency on the dimensions of the laser weld that for the two waveforms, SIN2 and SQR2 are shown in Figures 4.18 to 4.21. The depth-of-
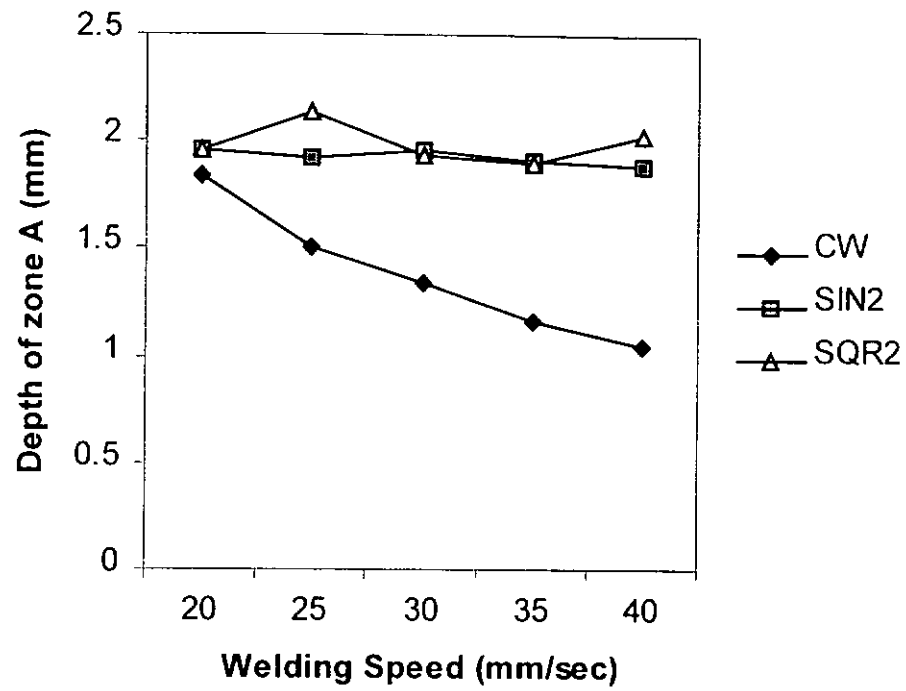
Figure 4.14: Effect of welding speed on depth of zone A.
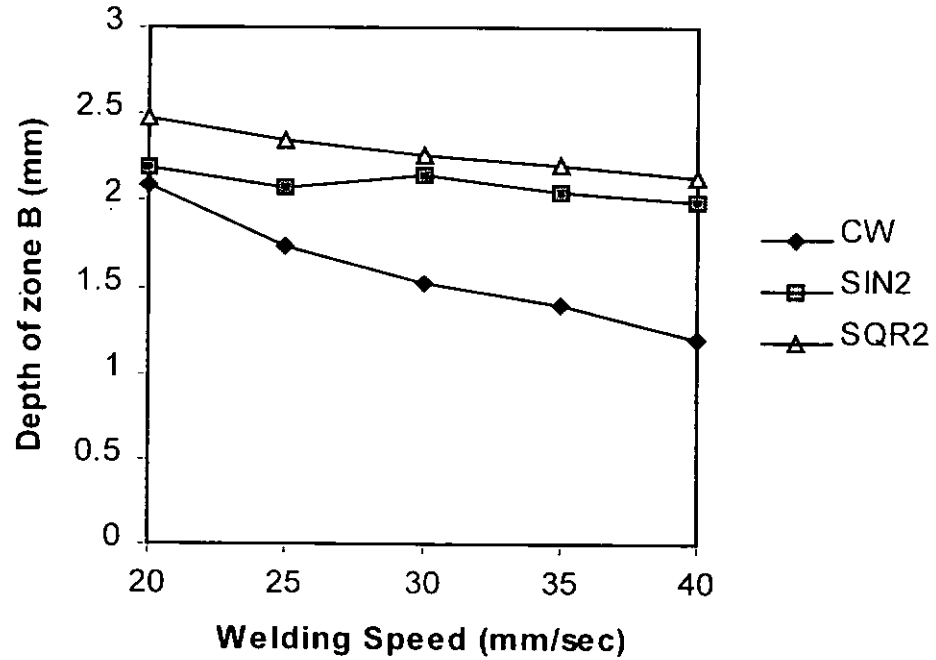(mean power = 1200W, pulse frequency = 100Hz)

Figure 4.15: Effect of welding speed on depth of zone B.
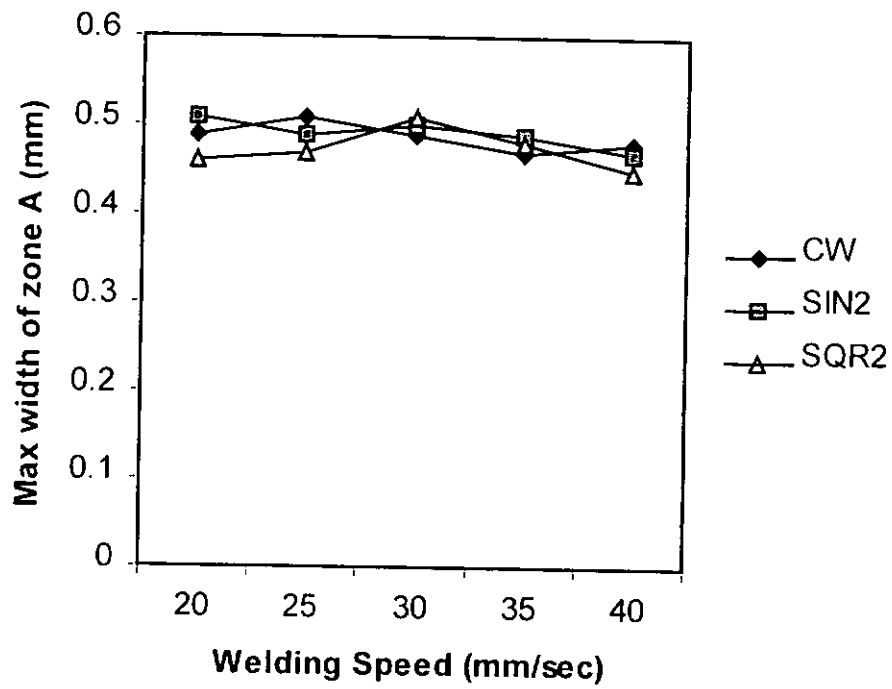(mean power = 1200W, pulse frequency = 100Hz)

Figure 4.16: Effect of welding speed on width of zone A.
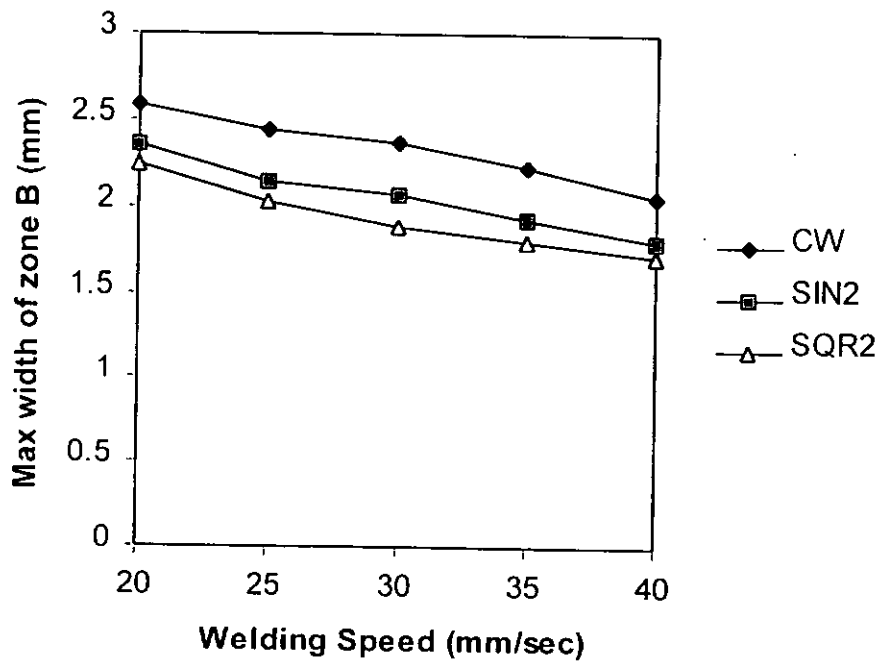(mean power = 1200W, pulse frequency = 100Hz)

Figure 4.17: Effect of welding speed on width of zone B.
(mean power = 1200W, pulse frequency = 100Hz)

Figure 4.18: Effect of pulse frequency on depth of zone A.
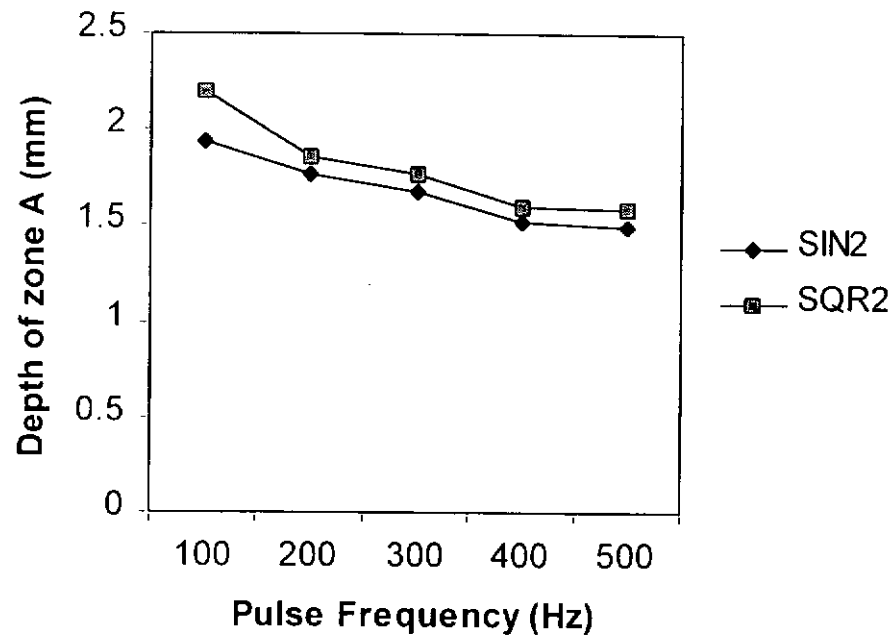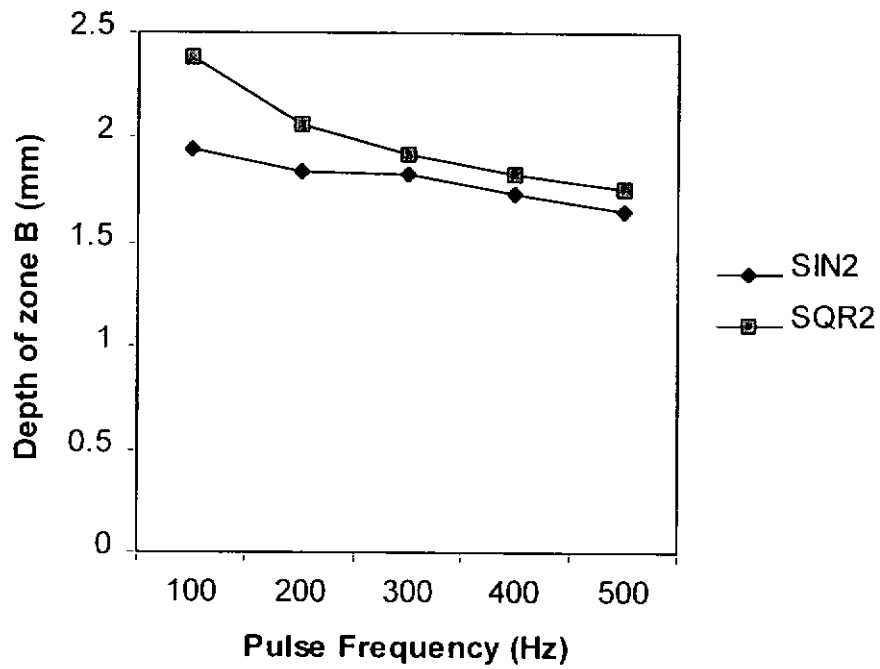(mean power = 1200W, welding speed = 25mm/s)

Figure 4.19: Effect of pulse frequency on depth of zone B.
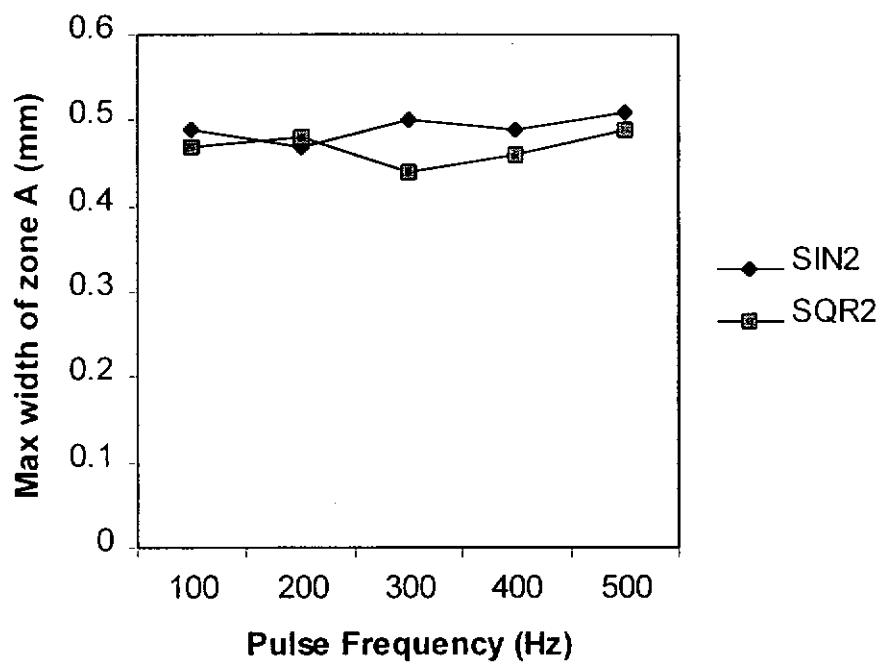(mean power = 1200W, welding speed = 25mm/s)

Figure 4.20: Effect of pulse frequency on width of zone A.
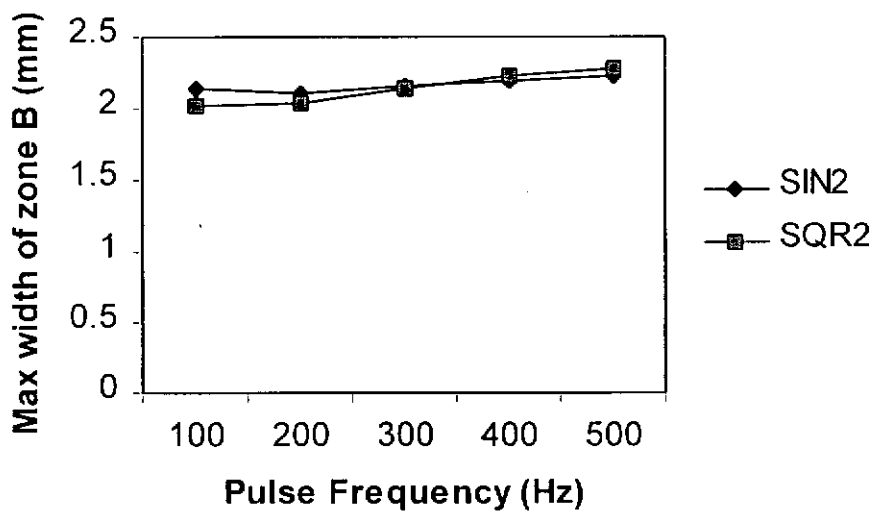(mean power = 1200W, welding speed = 25mm/s)

Figure 4.21: Effect of pulse frequency on width of zone B.
(mean power = 1200W, welding speed = 25mm/s)

penetration was reduced as the pulse frequency was increased. This could be attributed to the fact that for high frequency pulses insufficient pulse-on-time was allowed for the keyhole to be fully developed. Finally, the width of zone A varied very little as the welding speed or the pulse frequency was increased. This confirmed the conclusion that the width of zone A was closely related to the size of the keyhole which was largely controlled by the optical system of the laser.

4.2.3 Theoretical prediction on depth of zone A

In fact, for a fixed welding condition, the depth of zone A in pulse mode welding can be predicted by using the threshold intensity model for laser cutting [48]. It is considered that there exists a threshold intensity, I_t, at which SiC particles would be completely melted during laser welding. In this model it is assumed that the depth of zone A is equal to the depth of the keyhole. In order to predict the depth of zone A, it is assumed that the incident laser beam has a Gaussian intensity distribution:

$$I(r, z) = I(0, z) \cdot \exp[- \frac{2\,r^2}{R^2\,(z)}] \tag{1}$$

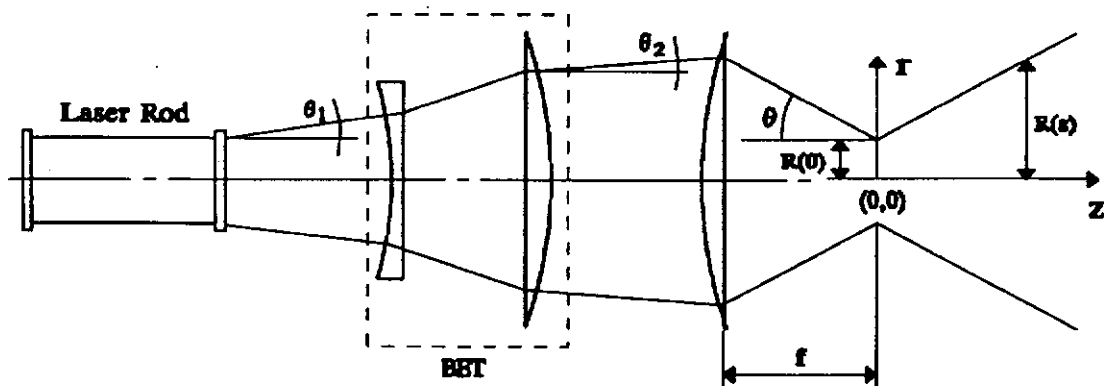the notations of the various parameters are shown in Figure 4.22.

Figure 4.22: Diagram of the laser beam propagation profile

where, $I(0,z)$ is the laser intensity at the central point of the laser beam in the z-plane, $I(r,z)$ is the local laser beam intensity at the coordinate (r,z), and $R(z)$ is the radius of the laser beam of which its intensity is down to $1/e^2$ of the center value.

According to the law of Gaussian beam propagation

$$R(z) = \sqrt{R^2(0) + (\theta z)^2} \tag{1}$$

where θ is the half-angle of the focusing laser beam as shown in Fig.4.21

The central intensity $I(0,z)$ can be determined using the following equations:

$$\frac{I(0,z)}{I(0,0)} = \frac{R^2(0)}{R^2(z)} \tag{2}$$

$$I(0,0) = \frac{2 P_{LP}}{\pi R^2(0)} = \frac{2E}{\pi R^2(0) t_i} \tag{3}$$

where $I(0,0)$ is the central intensity at the focus plane, P_{LP} is the pulse power, E is the pulse energy, and t_i is the pulse duration.

Substitute *equations (1)* and *(3)* into *(2)*

$$I(0,z) = \frac{2E}{\pi [R^2(0) + (\theta z)^2] t_i} \tag{4}$$

If D_A is the depth of zone A, according to the principle of the threshold intensity model the following condition should be satisfied:

$$I(0, D_A) \geq I_t \tag{5}$$

Therefore,

$$\frac{2E}{\pi [R^2(0) + (\theta D_A)^2] t_i} \geq I_t \tag{6}$$

Equation (6) can be rearranged as:

$$D_A \leq \sqrt{\frac{2E}{\pi t_i I_t} - R^2(0)} / \theta \qquad (7)$$

In equation (7), the magnitude of *R(0)* and θ depends on the arrangements of the laser beam guiding optics. *I(0,0)* is related to *R(0)* and the laser beam parameters *E* and t_i; whereas, I_t is a material property of SiC and is determined from experiment. This formula thus depict the conditon of the bottom position of zone A at which SiC particles are completely melted. Using equation (7), a comparison of the theoretical and experimental results on the depth of zone A for SQR1 and SQR2 was made (Figs. 4.23-4.24), and the two results are in good agreement. These results clearly show that the depth-of-penetration increased as the pulse duration was reduced.

4.3   Summary

The laser output waveform has a significant effect on both the depth-of-penetration and the amount of porosity formed in the weld. The results show that although the square waveform can produce the greatest depth-of-penetration of the three different waveforms studied, i.e. CW, sine-wave and square-wave, a high level of porosity was observed in the weld. This was believed due to the inherent fast cooling rate of the square-wave process. Whereas, porosity free welds with a reasonable depth-of-penetration could be obtained by using a sine-waveform operated at high peak powers. The depth of the aluminium carbide zone can be predicted by using a laser threshold intensity model.

Figure 4.23: A comparison of the theoretical and experimental results on the depth of zone A for SQR1. (welding speed = 25mm/s, pulse frequency = 100Hz)
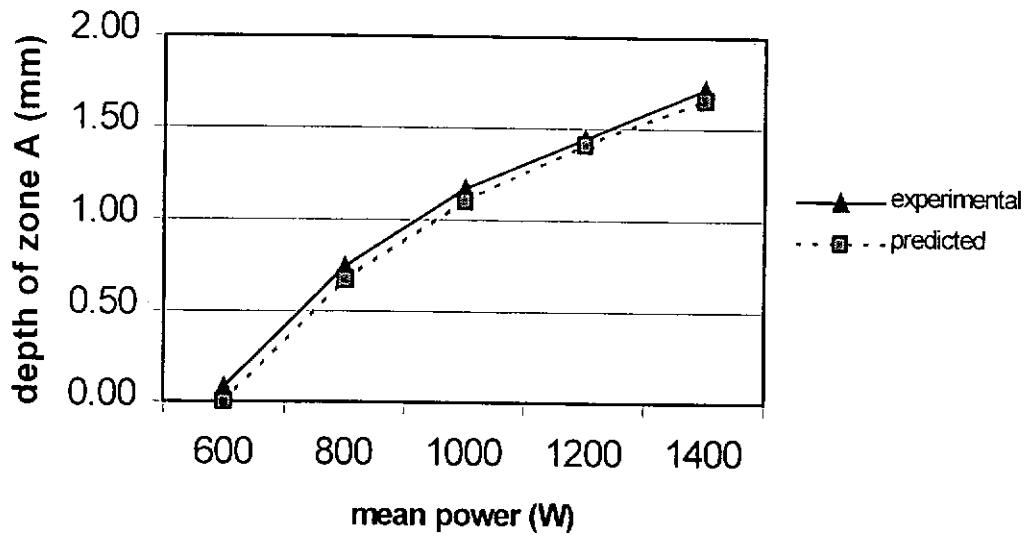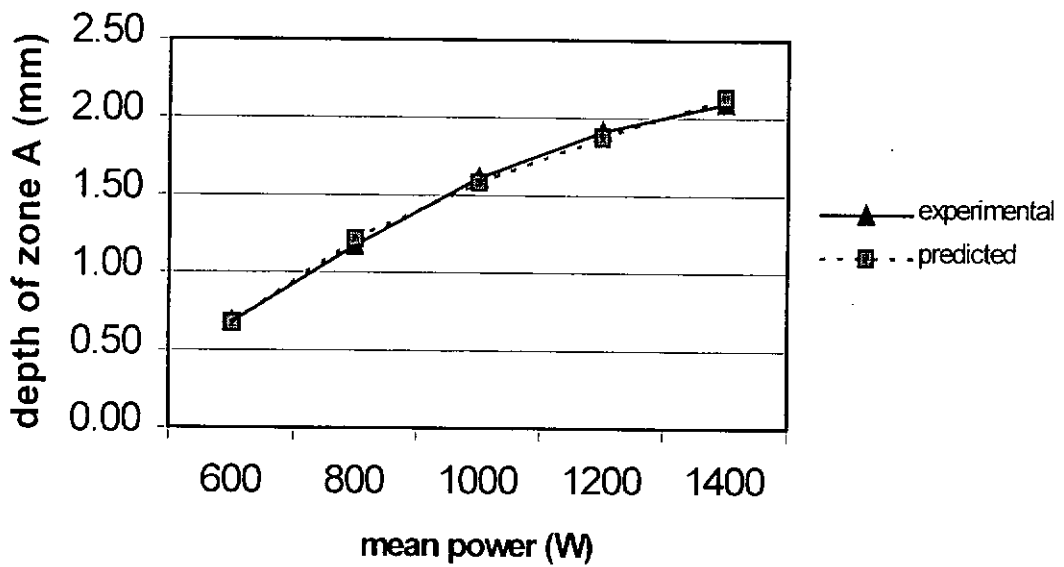

Figure 4.24: A comparison of the theoretical and experimental results on the depth of zone A for SQR2. (welding speed = 25mm/s, pulse frequency = 100Hz)

4.4 Elimination of carbides by nickel plating

The above results clearly show that it would not be possible to stop the formation of harmful aluminium carbides in the weld zone simply by varying the laser output parameters and the waveform. To eliminate Al-carbides, a "sandwich" welding technique was used. In order to obtain a good quality weld, it is vital to obtain a layer of compact nickel coating on the joining surfaces of the MMC at the first place.

4.4.1 Brush Plating of SiC/Al MMCs

Figures 4-25 and 4.26 show the cross sections at the interfaces of the nickel MMC interface produced by the two different experimental procedures 1# and 2# respectively. The thickness of the coating in both cases had reached 300μm without splitting. Although, both procedures were able to apply a layer of nickel coating on the MMC surface, procedure 2# has produced a better quality interface than procedure 1# did (c.f. Fig. 4.25 and Fig.4.26). Moreover, in the latter case more SiC particles together with some impurities were always present at the coating/matrix interface. The reason for that could be due to the fact that while the main function of Activator #2 was to remove the compact aluminium oxide, however, at the same time the metal matrix was also removed. As a result, many SiC particles and some soft aluminium oxide were left on the surface of the MMC substrate. In procedure 2#, an extra cleaning step was employed before Nickel Special was deposited. Now, because Activator #3 removed the metal matrix in a very slowly manner less SiC particles, oxide residues and porosity were found on the substrate surface. Also there may be more time for the impurities (such as carbon) on the surface to be oxidized.
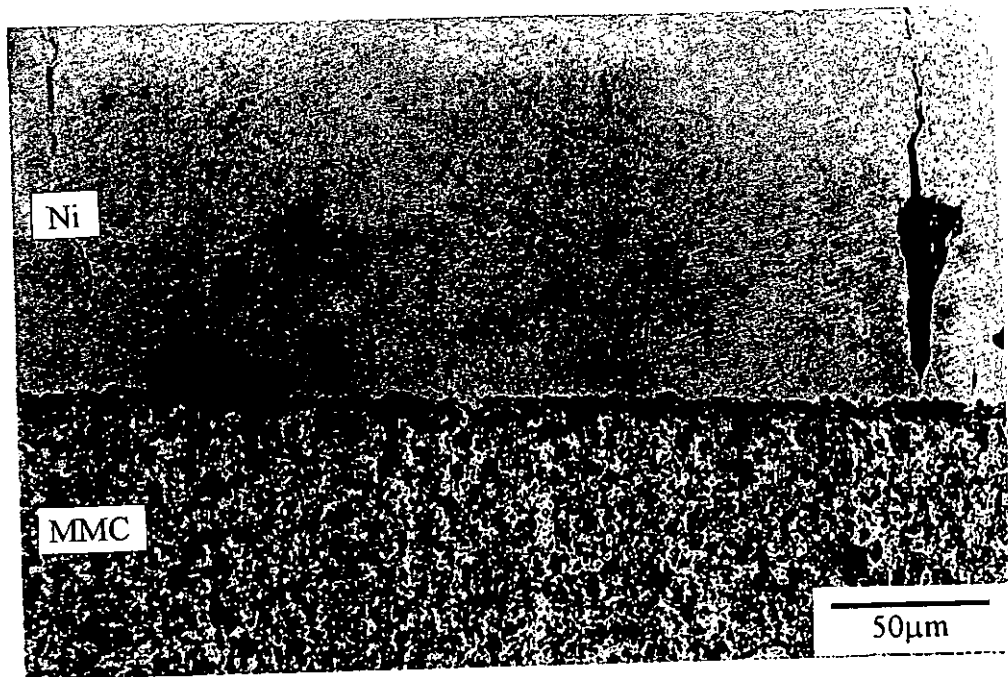
Figure 4.25: Nickel coating produced by brush-plating procedure 1#
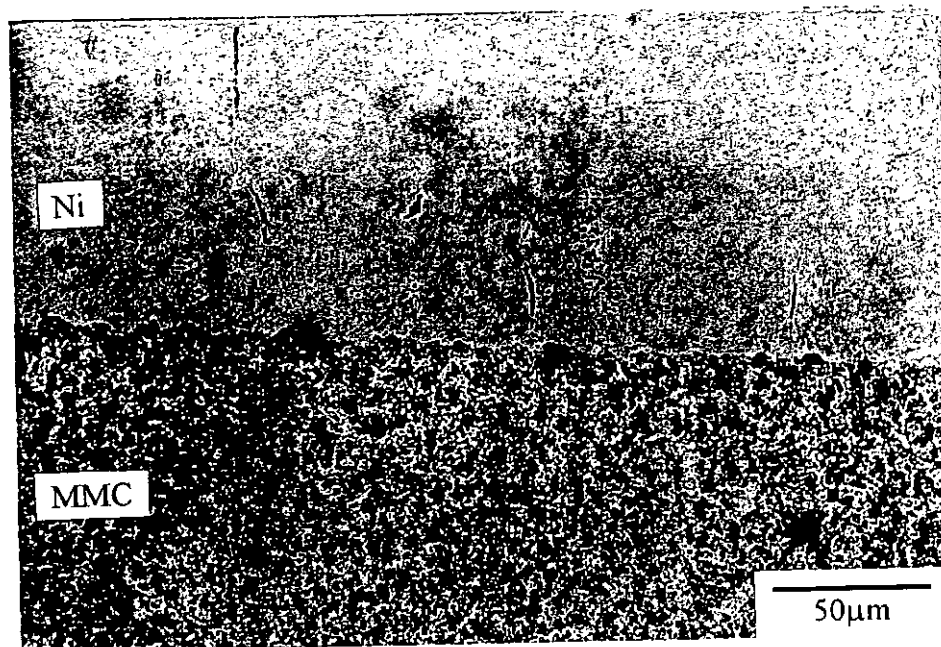

Figure 4.26: Nickel coating produced by brush-plating procedure 2#

No crack was found at the interface of the Ni coating and the Al-matrix, however, small amount of porosity and cracks were observed in the Ni coating layer. Looking at the morphology of the cracks, it appears that they were developed by joining up the porosity under the influence of internal stresses. Only those samples produced by procedures 2# were used for the laser welding experiment since a defect free interface is essential for achieving a good quality butt-joint.

4.4.2   Laser Welding of Nickel Plated MMC

4.4.2.1 Critical Power Density For Welding Ni-Plated Samples

Laser welding was performed on the nickel-plated samples as well as the non-plated samples using a sine-wave operated at different mean powers. The conditions of the samples used for the welding experiment together with the laser parameters employed are presented in Chapter 3, Tables 3.5 and 3.6 respectively. The effect of laser power intensity on the depth of keyhole for the plated and the non-plated samples are shown in Table 4-1. The bold font "-p-" in the table denotes that full weld penetration was achieved. The results show that for the plated samples the power intensity required for achieving the same depth of penetration as in the case of non-plated was at least 25% lower. The results also show that the thickness of the Ni layer did not seem to have much effect on the penetration depth. In pulsed laser processing, the critical power intensity (I_{th}) for vaporisation of metals has the following equation:

$$I_{th} = \frac{\lambda \quad K}{a \, C_P (1 - R)}$$

Where λ = enthalpy of vaporisation; a = focus spot size; C_p = heat capacity

Looking at this equation, the relatively low reflectivity (R) and thermal conductivity (K) of nickel perhaps in some way could explain why a lower power intensity was needed for the Ni plated samples.

Table 4-1. The effect of power intensity on depth-of-penetration

Mean Power (W)		600	800	1000	1200	1400
Peak power (W)		1200	1600	2000	2400	2800
Power intensity $(\times10^{10}W/m^2)$		0.61	0.82	1.02	1.22	1.43
Depth of keyhole in welding (mm)	Sample1#	1.18	1.83	-p-	-p-	-p-
	Sample2#	1.22	1.79	-p-	-p-	-p-
	Sample3#	1.14	1.82	-p-	-p-	-p-
	Sample4#	0.59	1.15	1.57	1.93	2.22

* Power intensity is considered as $(Peak\ Power)/(\pi a^2/4)$

* -p- denotes that it is full penetration weld

4.4.2.2 Microstructure of the welded Ni-MMC interface

The microstructure of the weld at the Ni-MMC interface of Samples 1# - 3# are shown in Figures 4.27(a-c). Good metallurgical bond was achieved in all three cases, and neither porosity nor crack was observed. Figures 4.28(a-d) show the results of the EDX elemental linear scanning analysis of nickel at the interfaces of the various samples, and the Ni-compounds detected at the interface were given in Table 4.2.
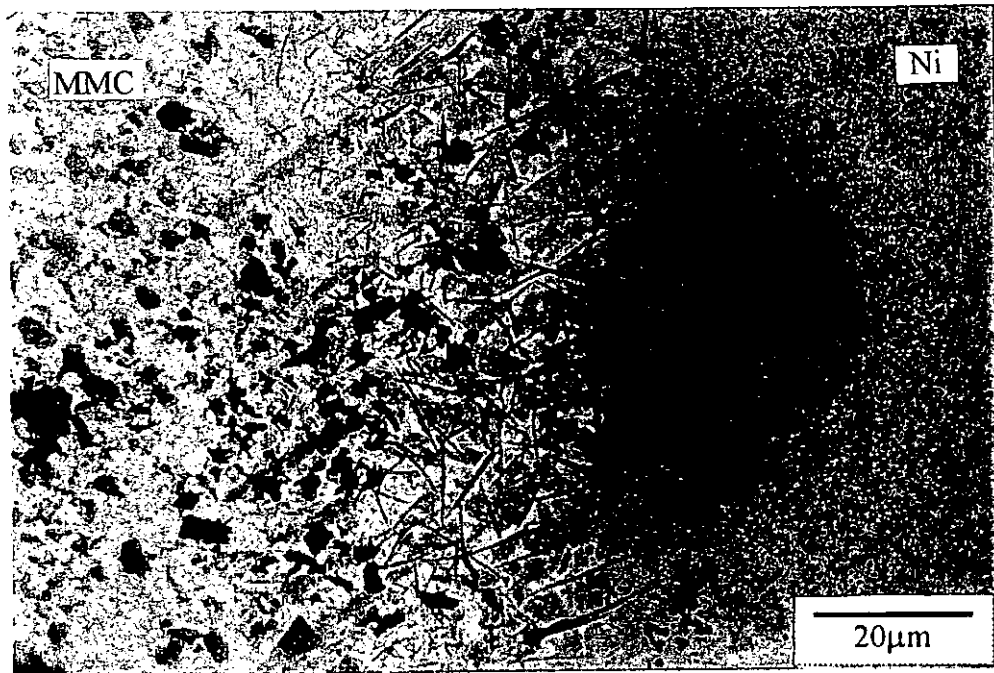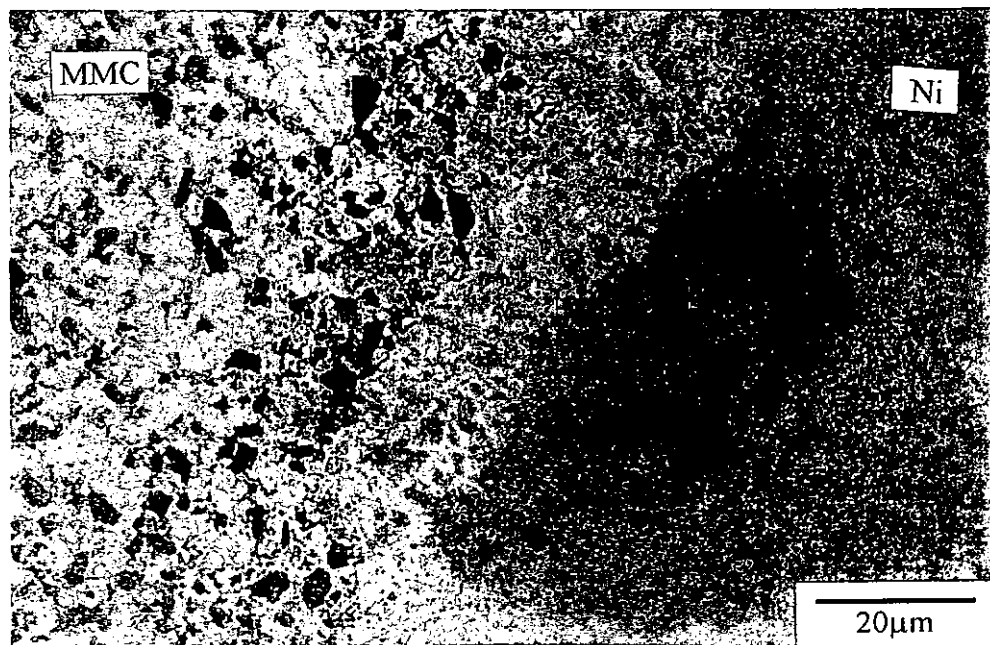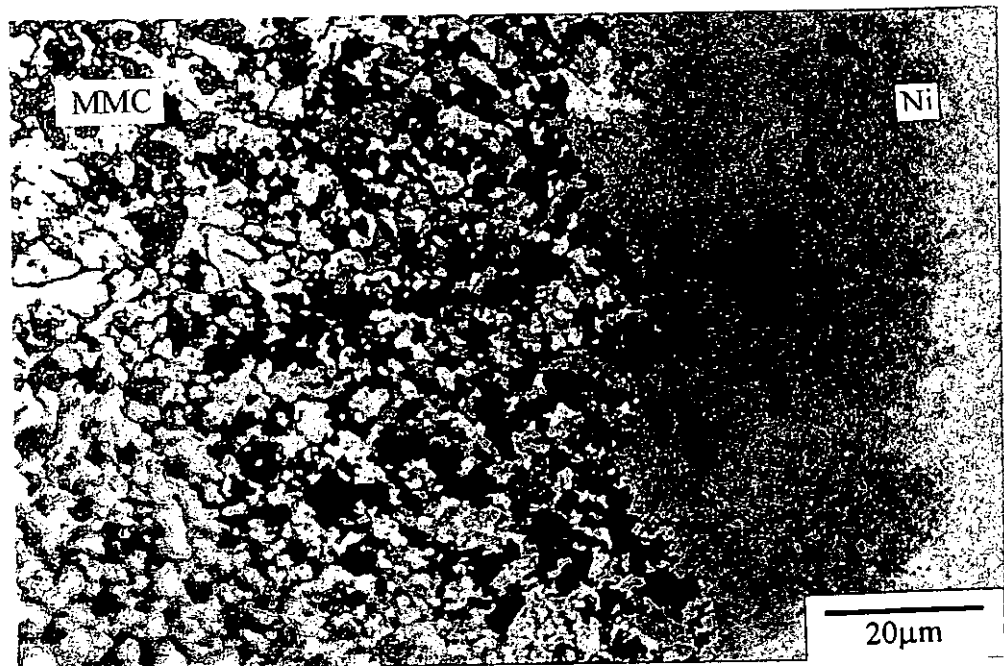
Figure 4.27 (a)

Figure 4.27 (b)

(c)

Figure 4.27: Microstructure at laser welded Ni-MMC interface.
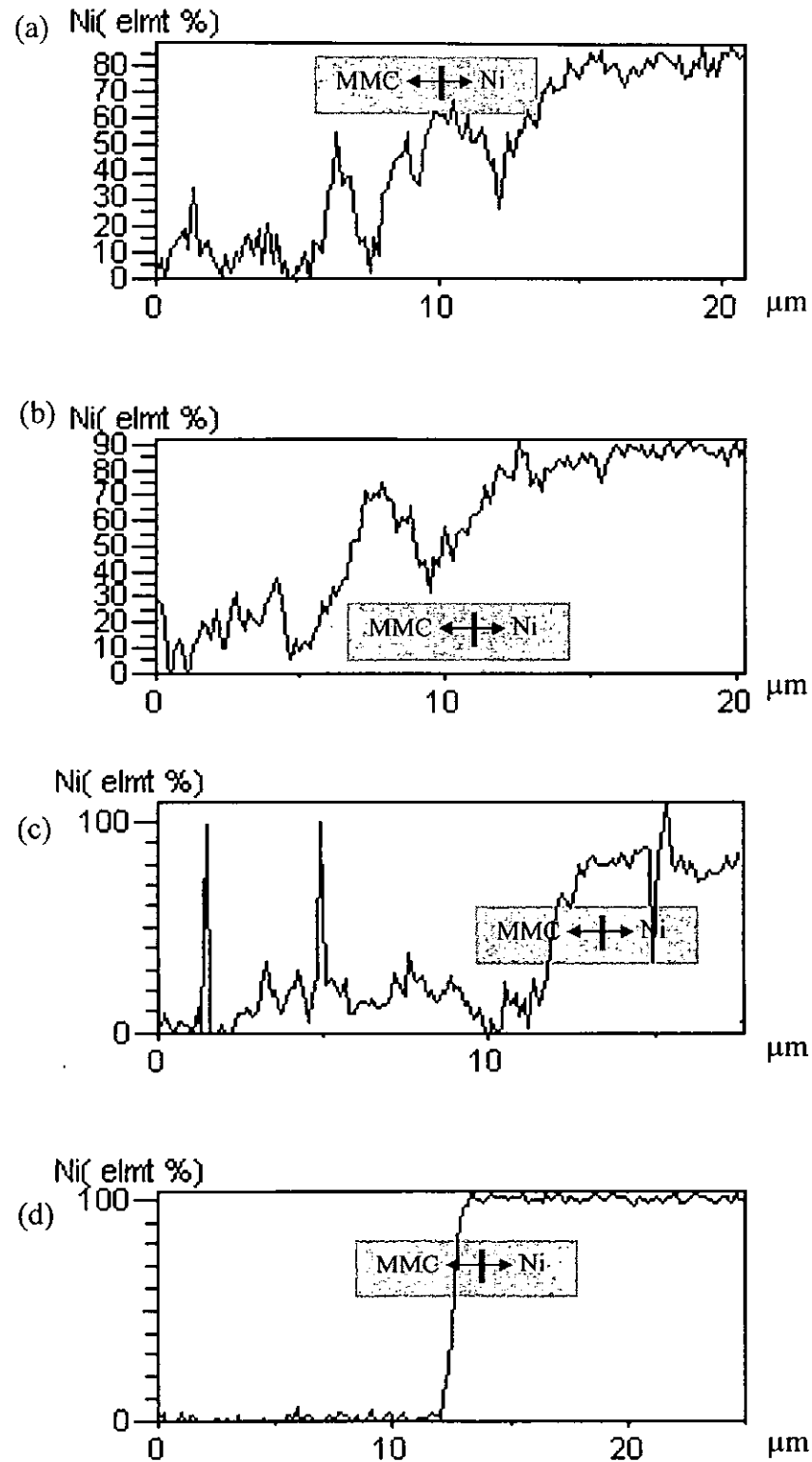(a) Sample1#; (b) Sample2#; (c) Sample3#.

Figure 4.28: EDS Elemental Linear Scanning Analysis of Nickel at the MMC-Ni interfaces. (a)Sample 1# laser welded; (b)Smple2# laser welded; (c)Sample3# laser welded; (d)before laser welding.

Results of the EDX analysis show that both Sample2# and Sample3# were free of the Al_4C_3 phase, however, Al_4C_3 compound which was in a plate-like form was detected at the Ni-matrix interface of Sample1# (Fig.4.27a). Apparently, a critical relationship must exist between the thickness of the coating and the laser parameters. In order that a carbide free interface is guaranteed further work in this area is obviously needed.

Table 4.2. Metallic compounds detected at the interfaces (see Appendix)

Sample number	Thickness of Ni plating	Metallic compounds				
		Al_3Ni	Al_3Ni_2	AlNi	$AlNi_3$	Al_4C_3
Sample1#	0.15mm	Yes	Yes	Yes	Yes	Yes
Sample2#	0.20mm	Yes	Yes	Yes	Yes	-
Sample3#	0.25mm	Yes	-	-	Yes	-

Figure 4.29 shows that after welding the nickelcoating exhibits a dendritic morphology. This means that during laser welding the temperature at the interface has been raised above 1455°C which is the melting point of nickel. According to the Al-Ni phase diagram [47], the reactions for the formation of the various Ni-compounds are as follows:

$$L \Leftrightarrow (Ni) + Ni_3Al \qquad \left(1385\ ^{\circ}C\right)$$

$$L + NiAl \Leftrightarrow Ni_3Al \qquad \left(1395\ ^{\circ}C\right)$$
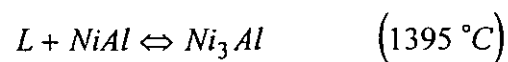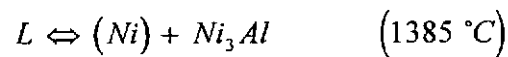
Since these reactions proceed at temperatures below the melting point of nickel, a strong liquid diffusion must have occurred at the interface and this has resulted a good metallic bonding between the matrix material and the nickel phase.
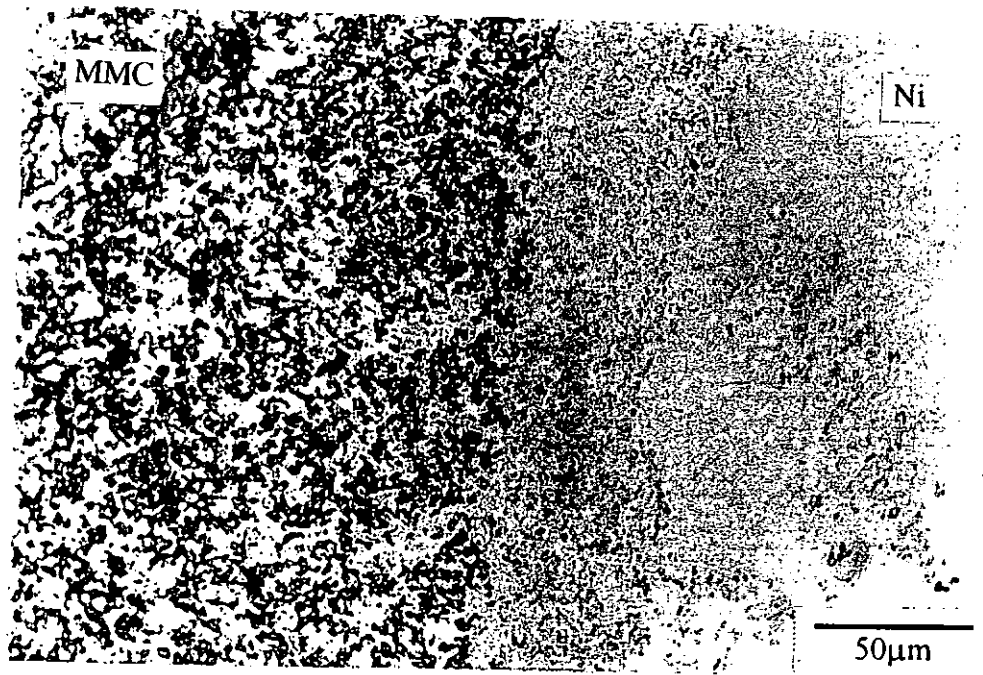
(a)
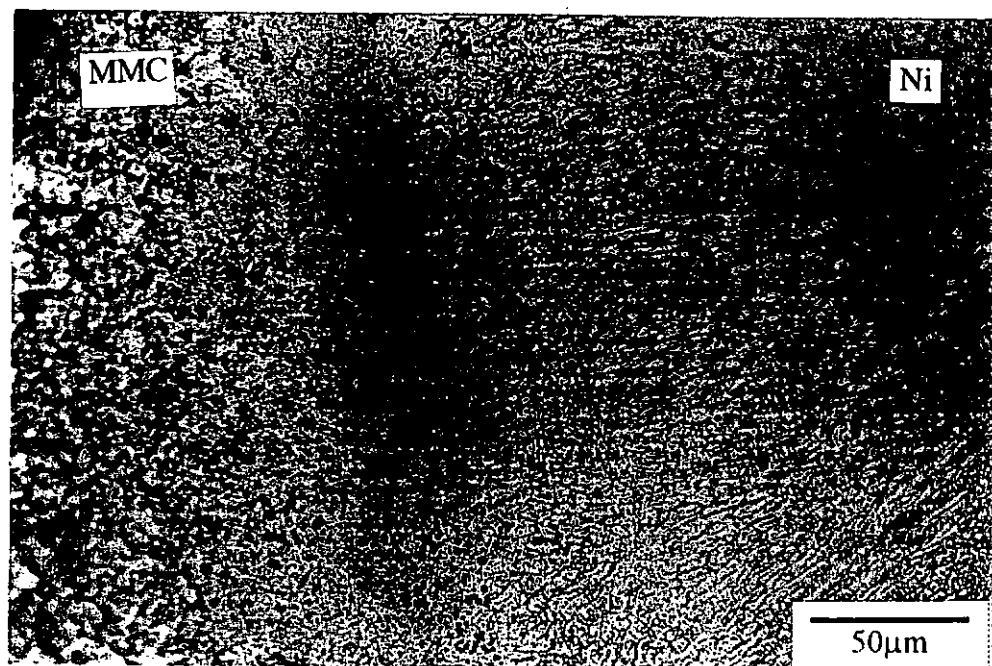
(b)

Figure 4.29: Ni-MMC interface after laser weld.
(a) not etched; (b) etched in nitric acid : glacier acetic acid 1:1 solution.

4.5 Corrosion Properties of Laser Weld

Figure 4-30 displays some typical potentiodynamic anodic polarization curves of the laser welded samples as well as the base material (un-welded) sample. Apparently, the curve of the non-plated sample and the Ni-plated sample was shifted respectively to the right and the left of that of the base material sample. This indicates that the corrosion current (I_{corr}) of the laser welded samples was greater than that of the un-welded sample with the former sample at a slightly more noble potential. The measured corrosion potential E_{corr} and the calculated corrosion current I_{corr} of the un-welded sample as well as the two different kinds of laser welded samples are listed in Table 4.3. Compared the weld with Ni plating to that without plating, a more than tenfold increase in the average corrosion rate was obtained.

Table 4.3: Corrosion potential E_{corr} and corrosion current I_{corr}

Specimen	Un-welded MMC	Laser Weld w/o Ni	Laser Weld with Ni
E_{corr} (mV)	-715.9	-685.8	-659.4
I_{corr} ($\mu A/cm^2$)	11.34	23.34	1.92

Figure 4.31 and Figure 4.32 show the appearance of the corroded un-welded sample and zone B of the laser welded sample. In both cases the tests were stopped at a corrosion potential of -250mV, and many deep cavities as well as cracks were found on the tested surface. However, larger cracks and cavities were found in the un-welded sample. Where as in zone B of the welded sample although more cavities were found, they are more evenly distributed. This could be due to the fact that the microstructure of zone B has been refined after laser welding. A higher magnification (Fig. 4.33) reveals that a particle was present inside these cavities or pits. The EDX point elemental analysis shows that the particle was SiC. (see
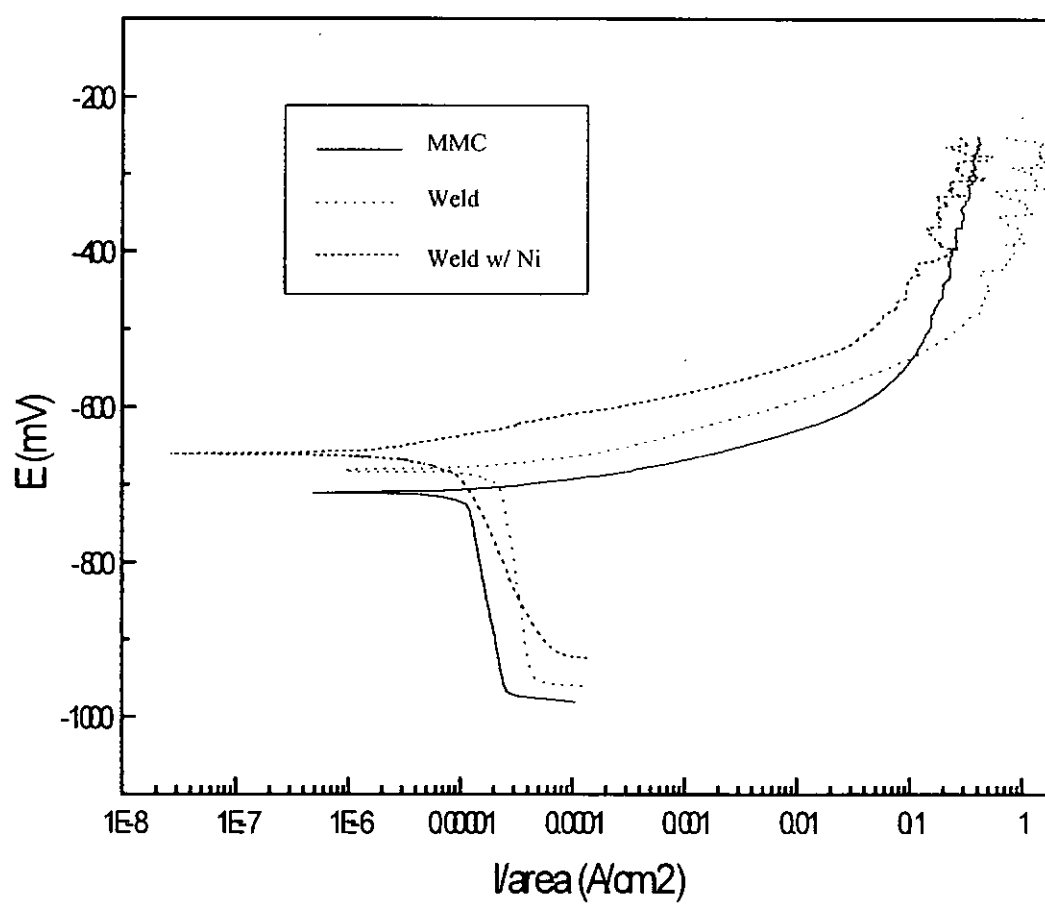
Figure 4.30: Anodic polarization plots for the welded and un-welded samples

Figure 4.31: Corroded surface of un-welded MMC, after anodic polarization test stopped at a corrosion potential of -250mV.

Figure 4.32: Corroded surface of zone B, after anodic polarization test stopped at a corrosion potential of -250mV.

Figure 4.33: Enhanced corrosion attack has occurred around a SiC particle
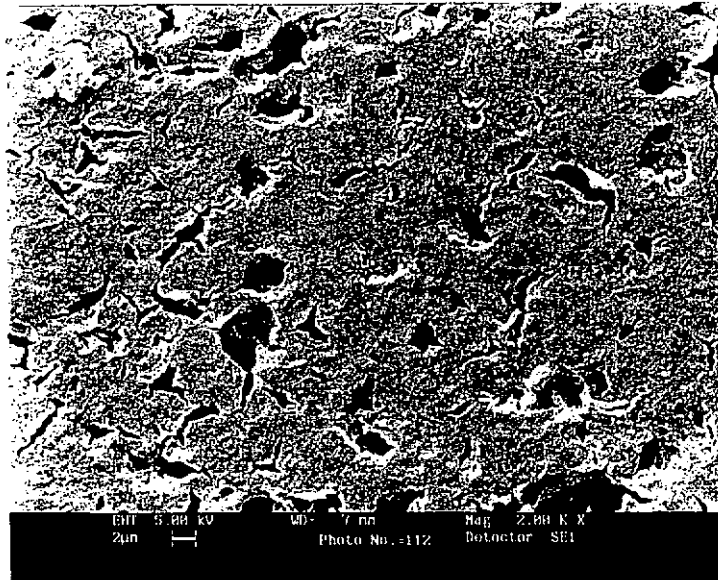
Figure 4.34: Corroded surface of un-welded MMC, after anodic polarization test stopped at a corrosion potential of +200mV.
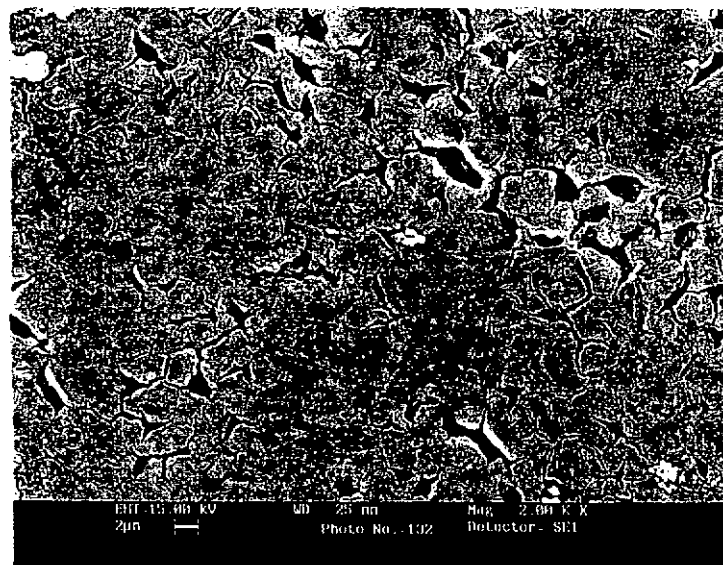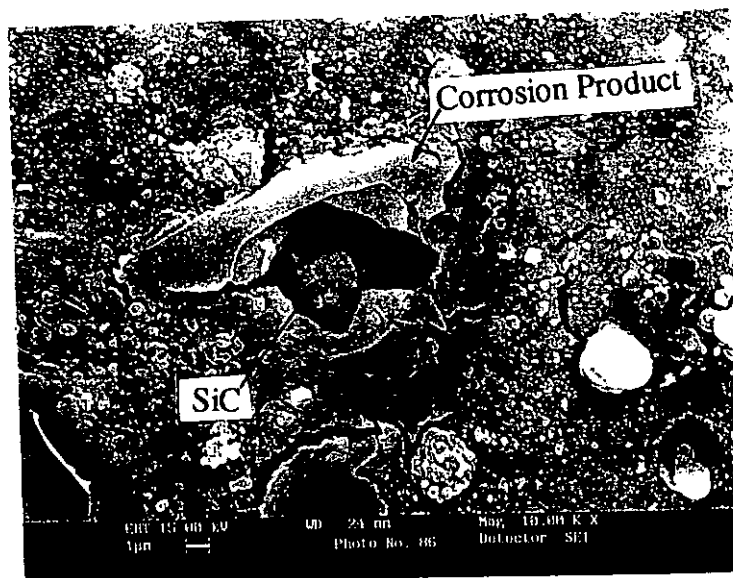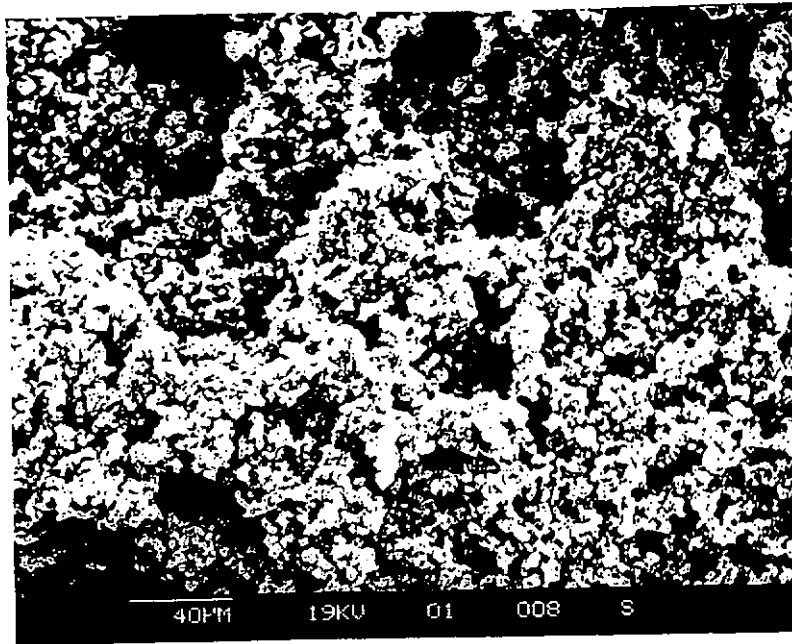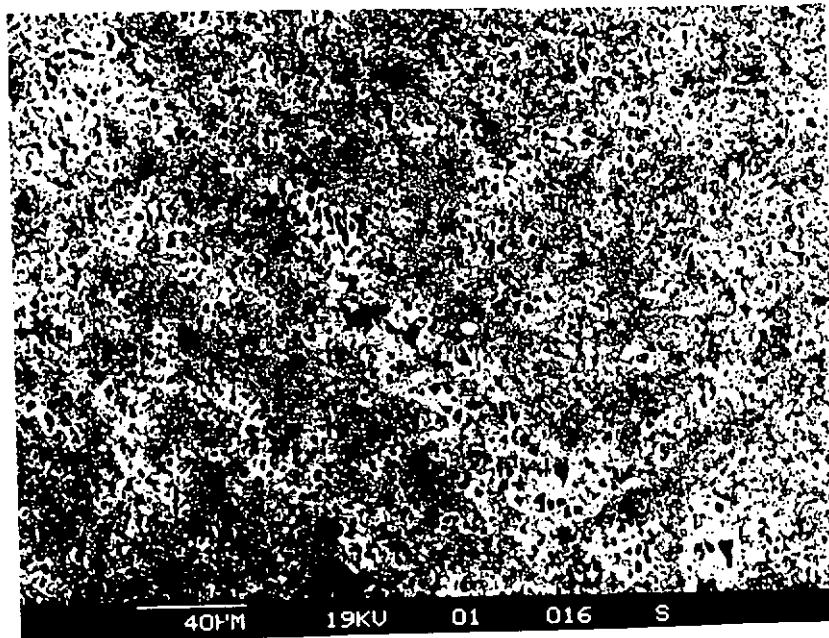

Figure 4.35: Corroded surface of zone B, after anodic polarization test stopped at a corrosion potential of +200mV.

Appendix) It can be seen that the matrix/particle interface has suffered enhanced corrosion attack and that deep pits were formed. The white substance adhered to the edge of corroded cavities was found containing a substantial amount of chlorine (see Appendix), hence it could be concluded that corrosion products of chloride were formed. Since the composite was prepared by the P/M route, elemental segregation at the interface should be minimal. It is therefore believed that galvanic corrosion has occurred, in that SiC acted as the net cathode while the matrix acted as the net anode. Further driving the test specimen to a higher corrosion potential has resulted in a complete corroded surface. Figures 4.34 and 4.35 show the appearance of the corroded areas of the parent material and zone B after the sample has been driven to a corrosion potential of +200mV. Comparing these two areas, zone B shows a more evenly corroded surface with much less corrosion products formed on the surface. It was understood that zone B had been melted and re-solidified, the improved corrosion property obtained for this zone was believed due to a more homogeneous matrix resulting from laser melting. Obviously, more work is required before a clear explanation on this can be obtained.

For the laser weld without Ni, it was found that zone A was corroded more seriously than zone B. Figure 4.36 shows the appearance of the corroded surface of zone A which have been driven to a corrosion potential of -250mV. It can be seen that the matrix around the primary silicon phase and the Al_4C_3 phase has been seriously attacked, and corrosion products were found at the interfaces. The EDX analysis confirms that the corrosion products contained chlorine. It is believed that the corrosion mechanism in zone A was also a galvanic type, in which Al_4C_3 and primary silicon phases acted as cathode. Furthermore, because a large amount of needle-like Al_4C_3 phase was formed a situation where a large cathode area to a small

anode area has arrived. This area effect could have an influential effect to the magnitude of the corrosion current density. In the corrosion test the current density was defined as the total current divided by the nominal surface area which includes both zone A and zone B. Therefore, in reality the corrosion current in zone A must be extremely high.

Further increase in the corrosion potential had resulted in the complete dissolution of the aluminium matrix with the network structure of the Al_4C_3 phase remained (Fig. 4.37). This situation was actually similar to that as occurs in the corrosion of pearlitic grey cast iron where highly active galvanic cells are created between the graphite flakes the anodic pearlite matrix. In an extreme case of galvanic corrosion of pearlitic grey cast iron, the matrix can corrode to such an extent that the cast iron is left as a network of interconnected graphite flakes. It was understood that aluminium carbide hydrolyses in water, it appears that the rate of galvanic reaction has preceded the dissolving rate in this kind of accelerated corrosion testing. However, it was found that after leaving the specimen in laboratory air for two weeks, zone A was completely destroyed having left behind some loose powder presumably aluminium hydroxide on the surface. It is therefore so important to prevent the formation of Al_4C_3 in the fusion zone in the first place.

Figure 4.38 shows the appearance of the corroded surface of the Ni-plated sample which has been driven to a corrosion potential of -250mV. In zone A where only pure nickel was found, no apparent corrosion pits nor any corrosion products were observed. At the nickel-composite interface where the various Al-Ni compounds exist, again no deep corrosion pit was found. On the contrary galvanic corrosion has happened and corrosion pits were found in zone B. The improvement of the corrosion properties of the weld having nickel plating was apparent.
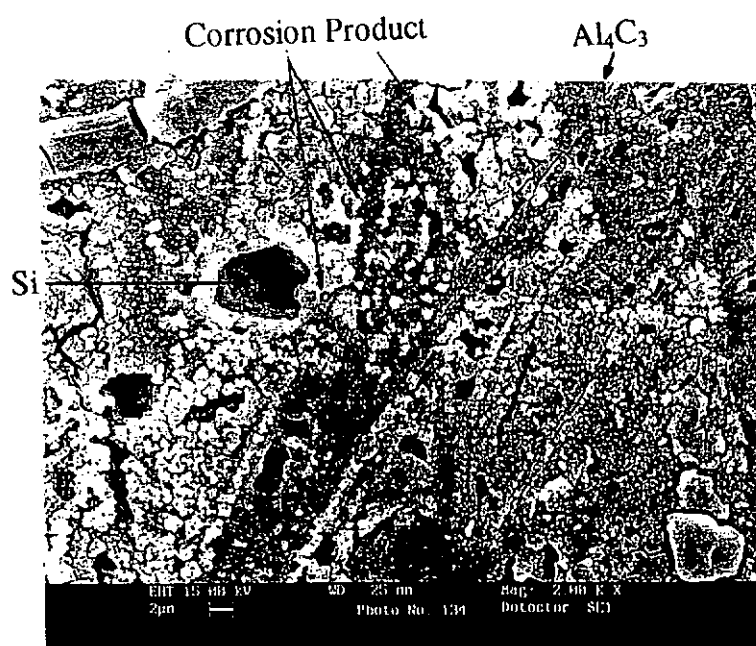
Figure 4.36: Corroded surface of zone A, after anodic polarization test stopped at a corrosion potential of -250mV.
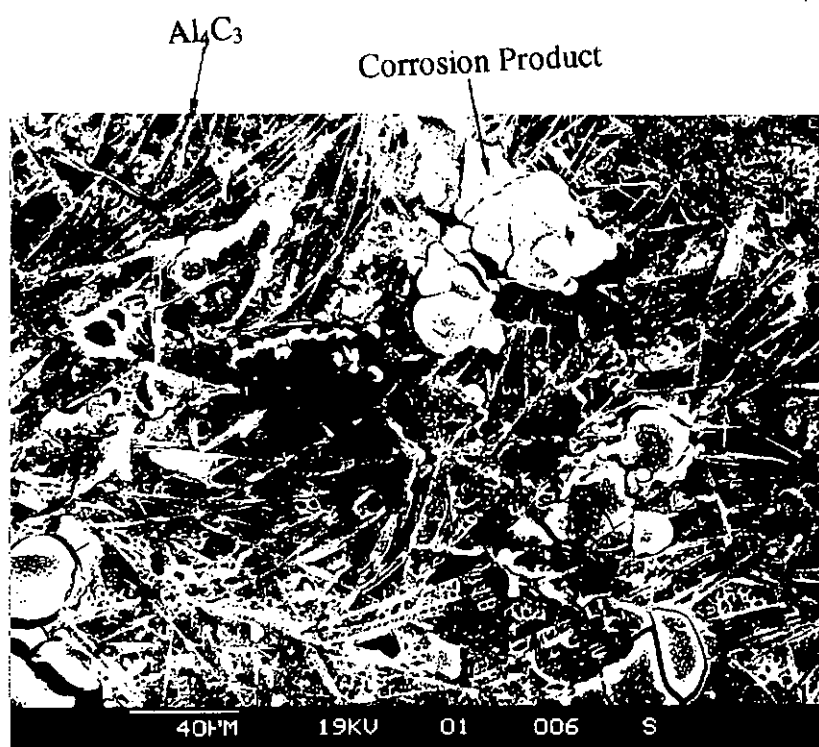

Figure 4.37: Corroded surface of zone A, after anodic polarization test stopped at a corrosion potential of +200mV.
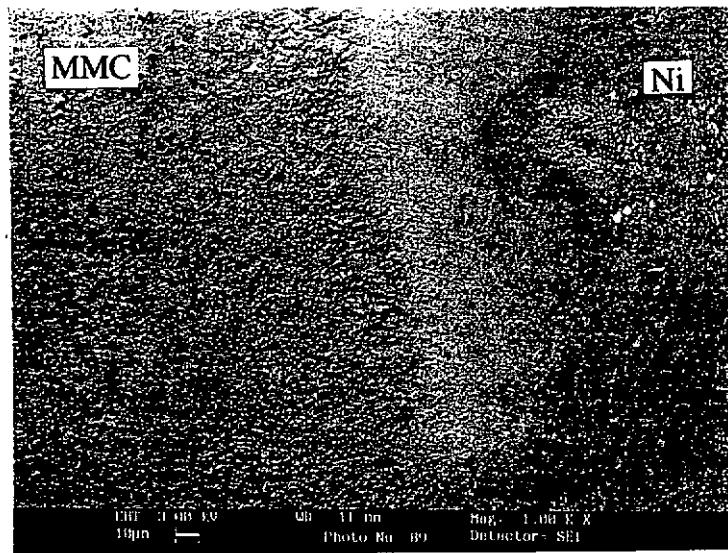
Figure 4.38: Corroded surface at the Ni-MMC interface after anodic polarization test stopped at a corrosion potential of -250mV.

Chapter 5. Conclusions

(i) Due to the development of keyhole in deep-penetration laser welding, it would not be possible to stop the formation of harmful aluminium carbides in the fusion zone simply by varying the laser output parameters and the waveform.

(ii) The laser output waveform has a significant effect on both the depth-of-penetration and the amount of porosity in the weld. The results show that although the square waveform could produce the greatest depth-of-penetration amongst the three different waveforms studied, i.e. CW, sine-wave and square-wave, a high level of porosity was observed in the weld. This is believed due to the inherent fast cooling rate of the square-wave process. Whereas, porosity free welds with a reasonable depth-of-penetration could be obtained by using a sine-waveform operated at high peak powers. The depth of the aluminium carbide zone can be predicted by using the threshold intensity model.

(iii) Laser welds without Al_4C_3 have been successfully produced by pre-welding treatment of the joining surfaces using a brush nickel plating technique. After laser welding, good metallurgical bond was obtained between the Ni coating and the composite matrix without the presence of the needle-like Al_4C_3 phase.

(iv) The nickel-plated laser joint has shown to have a better electro-chemical corrosion resistance than the non-nickel plated joint. The overall corrosion current was reduced by a factor of 10 when nickel plating was employed. For the non-nickel plated joint the fusion zone would be completely destroyed after leaving it in laboratory air for two weeks. This was due to the hydrolysis of Al_4C_3 to $Al(OH)_3$.

References:

(1)   Divecha, A.D., Fishman, S.G. and Karmarkar, S.D.
        "Silicon Carbide Reinforced Aluminium – A Formable Composite"
        Journal of Metals, Vol.33, No.9, pp.12-17, (1981)

(2)   Suresh S., Mortensen A. and Needleman A.
        "Fundamentals of Metal-Matrix Composites"
        Butterworth-Heinemann, Boston, (1993)

(3)   Mohn W.R. and Vukobratovich D.
        "Recent applications of metal matrix composites in precesion instruments
        and optical systems"
        Optical Engineering, Vol.27, No.2, pp.90-98, (1988)

(4)   Lundin C.D., Danko, J.C. and Swindeman, C.J.
        "Fusion Welding of SiC-reinforced Aluminum Alloy 2024",
        Conference: Recent Trends in Welding Science and Technology, Gatlinburg,
        Tenessee, USA, 1989, pp303-307. (1989)

(5)   Ellis, M.B.D.
        "Joining of Al-based metal matrix composites – a review"
        Materials and Manufacturing Processes 11(1), pp.45-66, (1996)

(6)   Kawall and Viegelahn, G.L.
        "Attempts at LASER Welding of an Alumina Reinforced 6061 Aluminum
        Alloy Composite"
        Advanced Composite Materials: New Developments and Applications
        Conference Proceedings, Detroit, Michigan USA, 1991, pp283-290. (1991)

(7)   Dahotre, N.B., McCay, T.D. and McCay, M.H.
        "Laser Processing of a SiC/Al-alloy Metal Matrix Composite"
        Journal of Applied Physics, Vol.65, No.12, pp5072-5077, (1989)

(8)   Lienert, T.J. Brandon, E.D. and Lippold J.C.
        " Laser and Electron Beam Welding of SiC_p Reinforced Aluminum A-356
        Metal Matrix Composite"
        Dcripta Metallurgica et Materialia, Vol.28, pp.1341-1346.(1993)

(9)   Dahotre, N.B., McCay, M.H., Gopinathan, S. and Sharp, C.M.
        "Laser Joining of Metal Matrix Composite"
        Proceedings of the Machining of Composite Materials Symposium, Chicago,
        Illinois, 1992, pp167-173. (1992)

(10)   McCay, M.H., McCay, T.D., Dahotre, N.D. and Sharp, C.M.
        "Fusion Zone Structures in Laser Welded Al-SiC Composites"
        Journal of Laser Applications, Vol. 3, No. 3, pp35-39. (1991)

(11)   Ehrstrom, J.C. and Kool, W.H.

"Production of rapidly solidified Al/SiC composites"
Journal of Materials Science, Vol. 23, PP 3195-3201, (1988)

(12) Nair, S.V. er al
"SiC-reinforced aluminum metal matrix composites"
International Metal Reviews, Vol. 30, No. 6, pp275-290, (1985)

(13) Brown, L.D., Maruyama, B. Cheong, Y.M., Rabenberg, L. K. and Marcus, H.L.
"Metal matrix interfaces and their impact on the mechanical behavior of composites"
Composite Interfaces, First International Conference on Composite Interfaces, Cleveland, Ohio, pp51-72, (1986)

(14) Fu, L.J., Schmerling, M. and Marcus, H.L.
"Interface studies of aluminum metal matrix composites"
Composite Materials: Fatigue and Fracture, ASTM STP 907, Philadelphia, pp 51-72, (1984)

(15) Hihara, L.H. and Latanision R.M.
"Corrosion of metal matrix composites"
International Materials Reviews, vol. 39, No. 6, pp245-264, (1994)

(16) Harrigan, W.C.
"Discontinuous Silicon Fiber MMCs"
Engineer's Guide to Composite Materials, ASM, pp889-895, (1987)

(17) McDaniels, D.L.
"Analysis of stress-strain, fracture and ductility behavior of aluminum matrix composites containing discontinuous silicon carbide reinforcement"
Metallurgical Transactions, Vol. 16A, No. 6, pp1105-1115, (1985)

(18) Logsdon, W.A. and Liaw, P.K.
"Tensile, fracture toughness and fatigue crack growth rate properties of silicon carbide whisker and particulate reinforced aluminum metal matrix composites"
Engineering Fracture Mechanics, Vol. 24, No. 5, pp737-751, (1986)

(19) White, J. and Murphy, M.
"Racing into production"
Materials World, vol. 5, No. 10, (1997)

(20) Goddard, D.M., Pepper, R.T., Upp, J.W. and Kendall, E.G.
"Feasibility of brazing and welding aluminum – graphite composites"
Welding Journal, Vol. 51, No. 4, pp. 178-182, (1972)

(21) Devletian, J.H.
"SiC/Al metal matrix composite welding by a capacitor discharge process"
Welding Journal, Vol. 66, No. 6, pp33-39, (1987)

(22)   Iseki, T., Kameda, T. and Maruyama, T.
        "Interfacial reactions between SiC and aluminum during joining"
        Journal of Materials Science, Vol. 19, pp 1692-1698, (1984)

(23)   Gopinathan, S., McCay, M.H. and McCay, T.D.
        "Continuous Wave CO_2 Laser Welding on SiC/A356 Al Metal Matrix
        Composites: an Analytical Estimate for the Formation of Aluminum
        Carbide"
        Processing of Advanced Materials, Vol. 3, pp213-224, (1993)

(24)   Khan, P.A. and Paul, A.J.
        "High Speed Joining of Aluminum Metal Matrix Composites Using
        Continuous Wave and Pulsed Lasers"
        Materials Research Society Symposium Proceeding, pp137-142, (1993)

(25)   Dahotre, N.B., McCay, M.H., McCay, T.D., Sharp, C.M. and Gopinathan, S.
        "Laser Welding of a SiC/Al-alloy Metal Matrix Composite"
        Conference: ICALEO'90, Vol. 71: Laser Materials Processing, Boston,
        pp343-356. (1990)

(26)   Cola, M.J., Lienert, T.J., Gould, J.E., Hurley, J.P.
        "Laser Welding of a SiC Particulate Reinforced Aluminum Metal Matrix
        Composite"
        Weldability of Material Conference, Detroit, pp297-303, (1990)

(27)   Dahotre, N.B., McCay, M.H., McCay, T.D., Sharp, C.M. and Gopinathan, S.
        "Pulse Laser Processing of a SiC/Al-alloy Metal Matrix Composite"
        Journal of Materials Research, Vol. 6, No. 3, pp514-529, (1991)

(28)   Dahtre, N.B., McCay, M.H.. McCay, T.D., Gopinathan, S. and Sharp, C.M.
        "Laser Joining of Metal Matrix Composite"
        Proceedings of Machining of Composite Materials Symposium, ASM
        Materials Week, Chicago, pp167-173, (1992)

(29)   Dahotre, N.B., McCay, T.D., and McCay, M.H.
        "Laser Induced Liquid Phase Reaction Synthesis Assisted Joining of Metal
        Matrix Composites"
        Materials and Manufacturing Processes, Vol. 9, No. 3, pp447-466. (1994)

(30)   Hauser, D., Kammer, P.A. and Dedrick, J.H.
        "Solid-state welding of aluminum"
        Welding Journal, Vol. 46, No. 1, pp11-22, (1967)

(31)   Olster, E.F. and Jones, R.C.
        "Diffusion bonded scarf joints in metal matrix composites"
        Composite Materials: Testing and Design, ASTM STP 460, pp393-404,
        (1969)

(32)   Cola, M.J. and Albright, C.E.

"Inertia friction welding of particulate reinforced aluminium composite – initial studies"
Proceedings of 3rd International Conference on Trends in Welding Research, pp.1139-1146, (1992)

(33)   Partridge, P.G. and Dunford, D.V.
"The role of interlayers in diffusion bonded joints in metal matrix composites"
Journal of Materials Science, Vol. 26, pp2255-2258, (1991)

(34)   Salkind M.J.
"Diffusion-bonding of whisker-reinforced aluminum"
Transactions of the Metallurgical Society of AIME, Vol. 242, No. 12, pp2518-2520, (1968)

(35)   Kazakov, N.F.
"Diffusion bonding of materials"
Pergamon Press, New York, pp.158-162, (1985)

(36)   Ready, J.F.
"Material processing - a overview"
Proceedings of IEEE, Vol. 70, No. 6, pp533-544, "1982"

(37)   Dawes, C.
"Laser welding – A practical guide"
Abington Pulishing – Cambridge, England, (1992)

(38)   Rubinstein, M.
"Electrochemical Metallizing Principles and Practice"
Van Nostrand Reinhold, New York, (1987)

(39)   Rubinstein, M.
"Electrochemical metallizing of advanced materials"
Materials & Manufacturing Processes, Vol. 4, No. 4, pp.561-578, (1989)

(40)   Ichinose, N.
"Introduction to Fine Ceramics"
Wiley - New York, (1987)

(41)   Lore, K.D. and Wolf, J.S.
"Extended abstracts, No. 154"
The Electrochemical Society, Abstract. Vol. 81-2, (1981)

(42)   Hihara L.H. and Latanision, R.M.
"Corrosion of metal matrix composites"
International Materials Reviews, Vol. 39, pp.245-264, (1994)

(43)   Turnbull A.
"Review of corrosion studies on aluminium metal matrix composites"
British Corrosion Journal, Vol. 27, No. 1, (1992)

(44)   Alwitt, R.S. and Thompson, G.E.
        " Aluminium Surface Treatment Technology"
        The Electrochemical Society – Princeton, (1986)

(45)   Mansfeld, F. and Jeanjaquet, S.L.
        "The evaluation of corrosion protection measures for metal matrix
        composites"
        Corrosion Science, Vol. 26, No. 9, pp.727-734, (1986)

(46)   Kawali, S.M. and Viegelahn, G.L.
        "Laser welding of alumina reinforced 6061 aluminum alloy composite"
        Proceedings of ICALEO/1991, pp.156-167, (1991)

(47)   Thaddeus, B.M.
        Binary Alloy Phase Diagrams,
        American Society for Metals, (1986)

(48)   Jiang, C.Y., Lau, W.S., Yue, T.M. and Chiang, L.
        "On the maximum depth and profile of cat in pulsed Nd:YAG laser
        machining"
        Annals of the CIRP, Vol. 42, No. 1, pp.223-226, (1993)

Further works:

Based on the experimental and analytical results of this study, the following recommendations are made for further research on laser welding of SiC/Al MMCs:

1. To develop a numerical model to simulate the temperature profile of laser welding of SiC/Al-based composites so that the various phase transformations in the weld zone can be better understood.

2. To develop fully the critical relationship between the thickness of the nickel coating and the laser output parameters such that no aluminium carbide is formed at the Ni/MMC interface.

3. The effects of the size of the fusion zone and the partially molten zone as well as their microstructure on the mechanical properties of the laser welded samples required a thorough investigation.

4. To study in some more detail the corrosion behaviour of the different microstructure produced in laser welding of SiC/Al-based MMCs. This could be achieved by reproducing the different microstructure on a larger area by laser surface melting and subjected these samples to corrosion tests.

Appendices: Result of EDX element analysis for phase identification

Appendix A: Analysis of the Ni-MMC interface of the laser welded sample.

A1: Al_3Ni phase

A2: Al_3Ni_2 phase
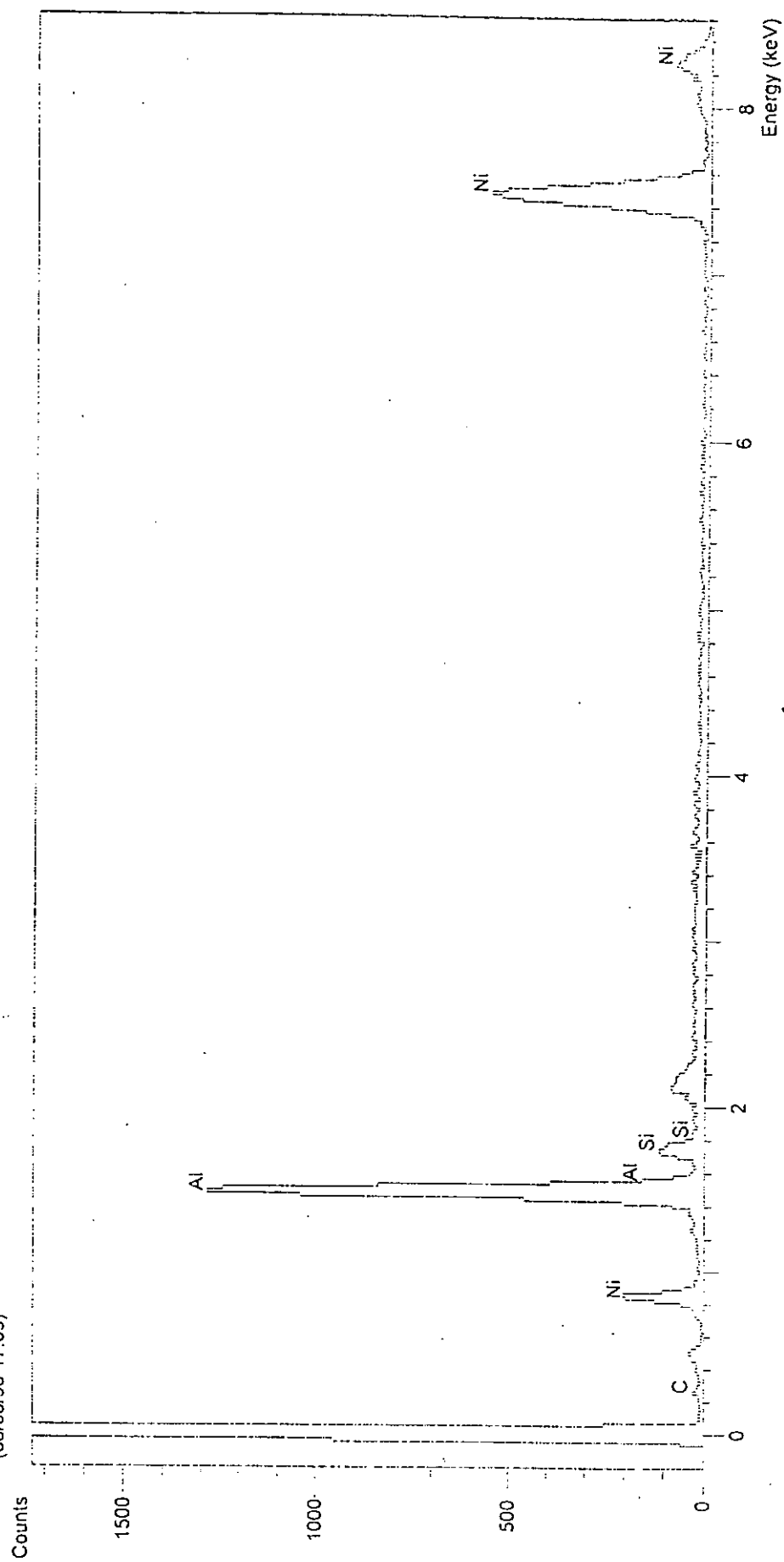
A3: AlNi phase

A4: $AlNi_3$ phase

A5: Al_4C_3 phase

Appendix B: Analysis of the surface of the MMC after anodic polarization test.

B1: SiC particle

B2: Corrosion products

Operator : Ma Hok Man
Client : All ISIS users
Job : QunatMap(demonstration data
(06/08/96 17:09)

Counts

1500

1000

500

0

Energy (keV)

Ni

Ni

Ni

Al

Al

Si

Ni

C

0   2   4   6   8

Appendix A1: Al₃Ni phase

- 90 -

SEMQuant results. Listed at 17:07:57 on 06/08/96
Operator: Ma Hok Man
Client: All ISIS users
Job: QunatMap[demonstration data
Spectrum label:

Calibration data: Energy Resn.   Area
 Strobe: -7.4 .43.50 22644
 Calib. element: '   6928.7 136.63 12178
 Gain factor = 50.077
 Livetime   = 60.0 seconds

Sample data: Energy Resn.   Area
 Strobe: -7.2 45.59   22079
 Total spectrum counts = 22486
 Livetime   = 60.0 seconds

System resolution = 61 eV

Geometry (degrees):
 Tilt   =   0.00
 Elevation   = 35.00
 Azimuth   =   0.00
 Entry angle =   0.00

Accelerating voltage = 20.00 kV

Quantitative method: ZAF (3 iterations).
 Analysed all elements and normalised results.
 1 peak possibly omitted: 5.90 keV

Standards :
 Al K   Al2O3 23/11/93
 Si K   Quartz 01/12/93
 Ni K   Ni 01/12/93

Elmt Apparent Stat.   Inten. Std   Element Sigma Atomic
      Conc.   Sigma   Corrn. Corrn.   %   %   %
Al K 26.121   0.319   0.717   0.98   54.18   1:28   69.14
Si K   2.069   0.128   0.494   1.07   6.23   .0.56   7.64
Ni K 24.128   0.877   0.907   1.00   39.59   1.37   23.22
Total   100.00   100.00

* = <2 Sigma
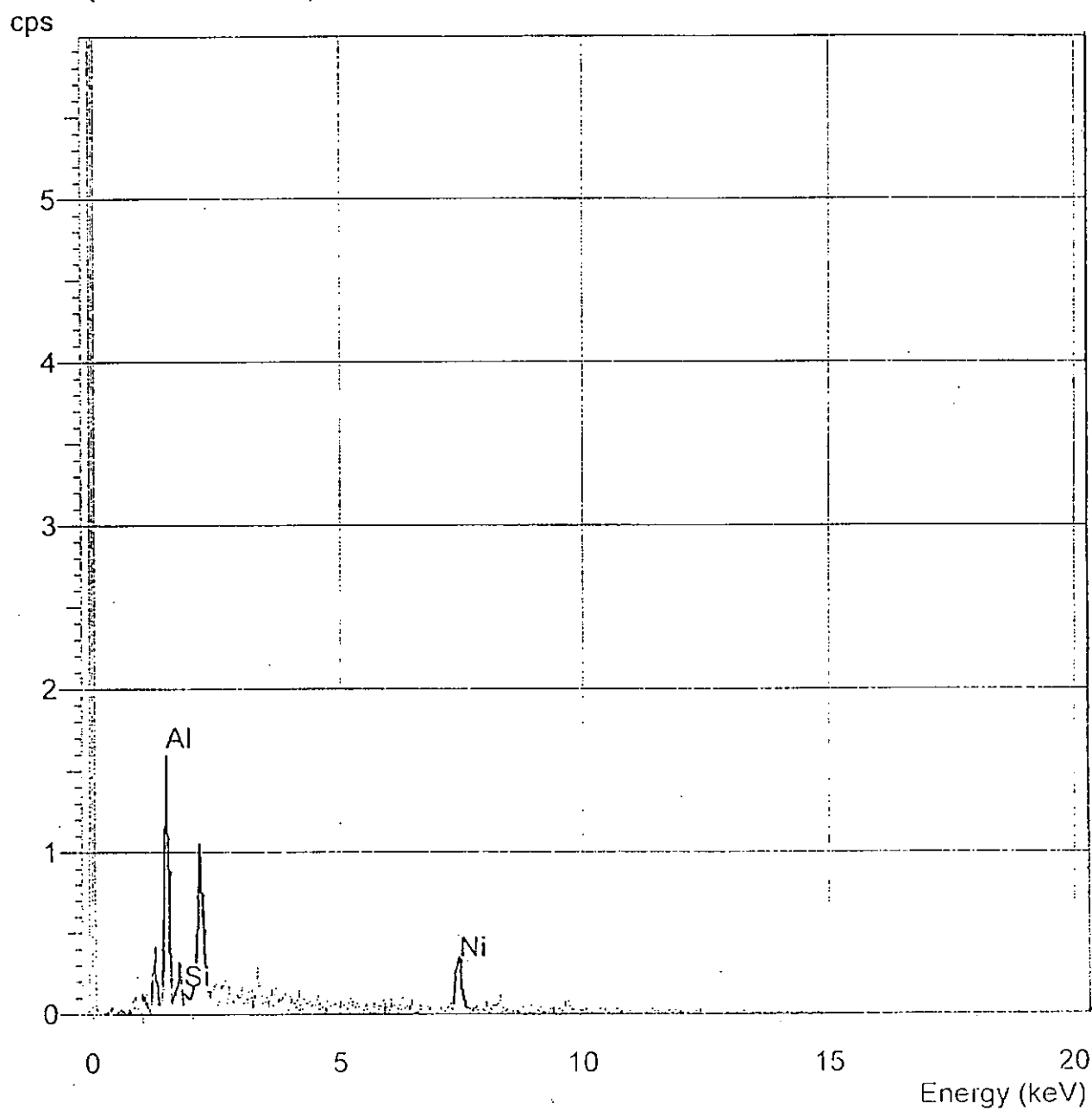
Appendix A2: Al$_3$Ni$_2$ phase

SEMQuant results. Listed at 11:01:57 on 4/11/1997
Operator: MRC, HKPU
Client: All ISIS users
Job: Demonstration data SiLi detector
Spectrum label:

Calibration data: Energy Resn.   Area
 Strobe: -6.6   97.57   17781
 Calib. element: 6903.6 157.13   4891
 Gain factor = 49.890
 Livetime   = 50.0 seconds

Sample data: Energy Resn.   Area
 Strobe: -7.2   45.04   33628
 Total spectrum counts = 4192
 Livetime   = 90.0 seconds

System resolution = 61 eV

Geometry (degrees):
 Tilt   =   0.00
 Elevation   =   35.00
 Azimuth   =   0.00
 Entry angle =   0.00

Accelerating voltage = 20.00 kV

Quantitative method: ZAF (3 iterations).
 Analysed all elements and normalised results.
 2 peaks possibly omitted: 0.00, 3.32 keV

Standards :
 Al K   Al2O3 23/11/93
 Si K   Quartz 01/12/93
 Ni K   Ni 01/12/93

Elmt	Apparent Conc.	Stat. Sigma	Inten. Corrn.	Std Corrn.	Element %	Sigma %	Atomic %
Al K	2.856	0.161	0.648	0.74	43.26	26.90	59.17
Si K	0.393	0.092	0.512	0.91	7.53	16.53	9.90
Ni K	4.607	0.485	0.919	1.00	49.20	29.62	30.93
Total					100.00		100.00

* = <2 Sigma
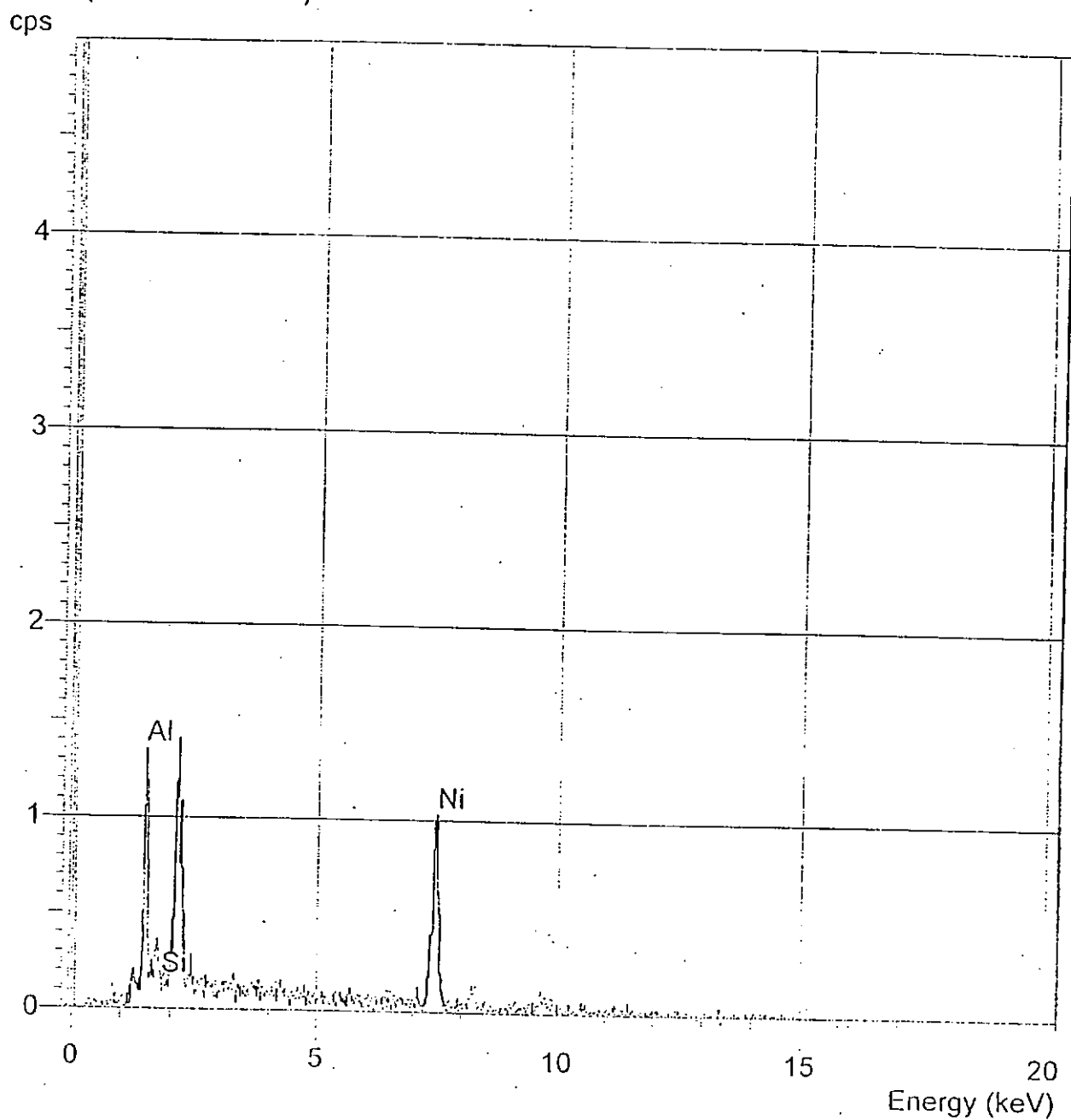
Appendix A3: AlNi phase

SEMQuant results. Listed at 10:58:14 on 4/11/1997
Operator: MRC, HKPU
Client: All ISIS users
Job: Demonstration data SiLi detector
Spectrum label:

Calibration data: Energy Resn.   Area
  Strobe: -6.6 97.57; 17781
  Calib. element: 6903.6 157.13   4891
  Gain factor = 49.890
  Livetime   = 50.0 seconds

Sample data: Energy Resn.   Area
  Strobe: -7.2 44.81 33846
  Total spectrum counts = 5261
  Livetime   = 90.0 seconds

System resolution = 61 eV

Geometry (degrees):
  Tilt   =   0.00
  Elevation   = 35.00
  Azimuth   =   0.00
 Entry angle =   0.00

Accelerating voltage = 20.00 kV

Quantitative method: ZAF (2 iterations).
  Analysed all elements and normalised results.
  1 peak possibly omitted: 0.00 keV

Standards :
  Al K   Al2O3 23/11/93
  Si K   Quartz 01/12/93
  Ni K   Ni 01/12/93

Elmt	Apparent Conc.	Stat. Sigma	Inten. Corrn.	Std Corrn.	Element %	Sigma %	Atomic %
Al K	2.351	0.156	0.559	0.74	28.76	13.43	44.88
Si K	0.398	0.105	0.528	0.91	5.14	8.96	7.71
Ni K	9.145	0.657	0.944	1.00	66.10	15.25	47.41
Total					100.00		100.00

* = <2 Sigma
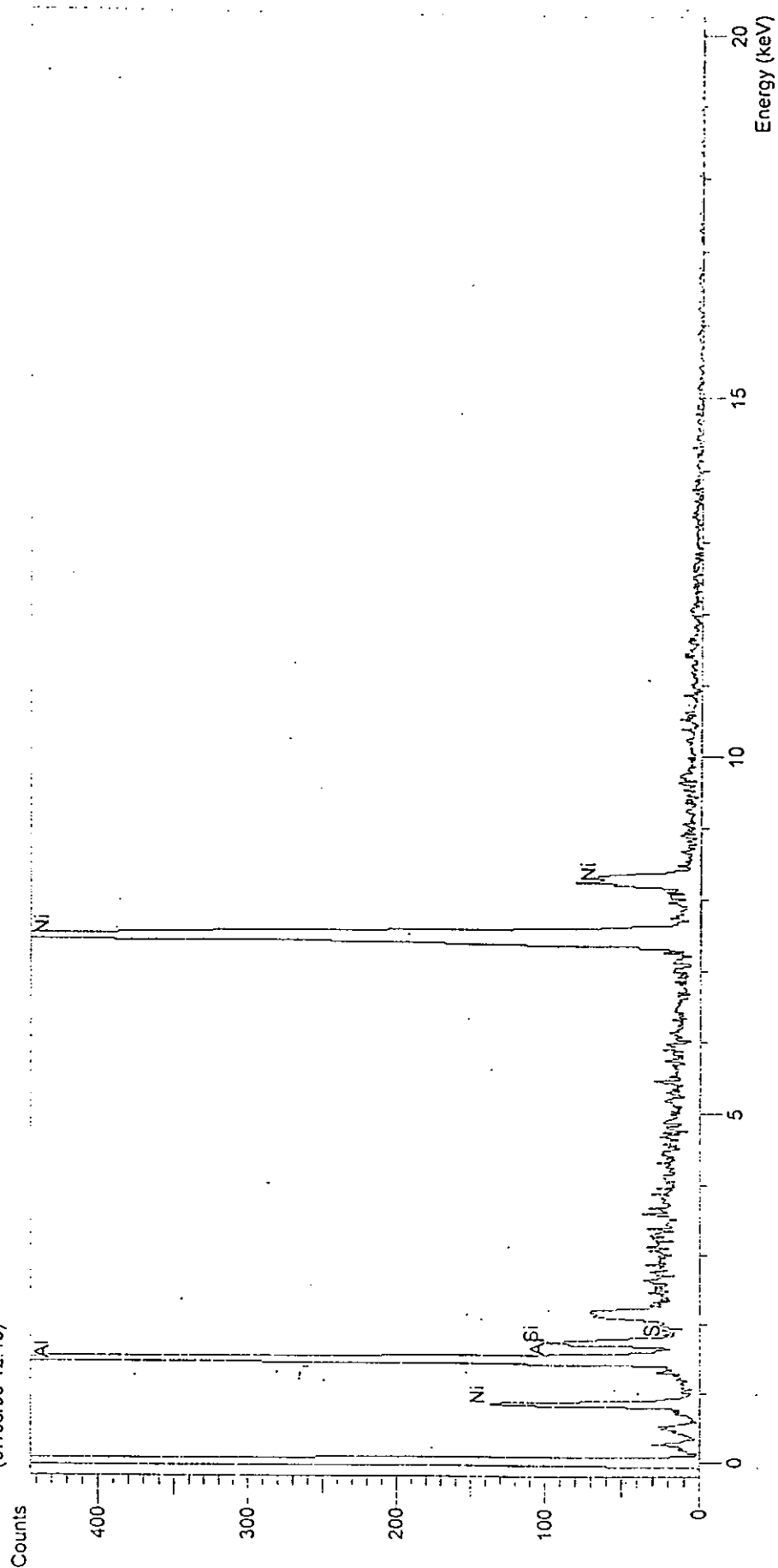
Appendix A4: AlNi₃ phase

SEMQuant results. Listed at 13:39:33 on 07/08/96
Operator: Ma Hok Man
Client: All ISIS users
Job: QunatMap[demonstration data
Spectrum label:

Calibration data: Energy Resn.   Area
  Strobe: -7.2   44.84   21880
  Calib. element: .6924.7 138.29 10324
  Gain factor = 50.047
  Livetime   = 60.0 seconds

Sample data: Energy Resn.   Area
  Strobe: -7.4   44.94   22106
  Total spectrum counts = 19039
  Livetime   = 60.0 seconds

System resolution = 61 eV

Geometry (degrees):
  Tilt   =   0.00
  Elevation   =   35.00
  Azimuth   =   0.00
  Entry angle =   0.00

Accelerating voltage = 20.00 kV

Quantitative method: ZAF (2 iterations).
  Analysed all elements and normalised results.
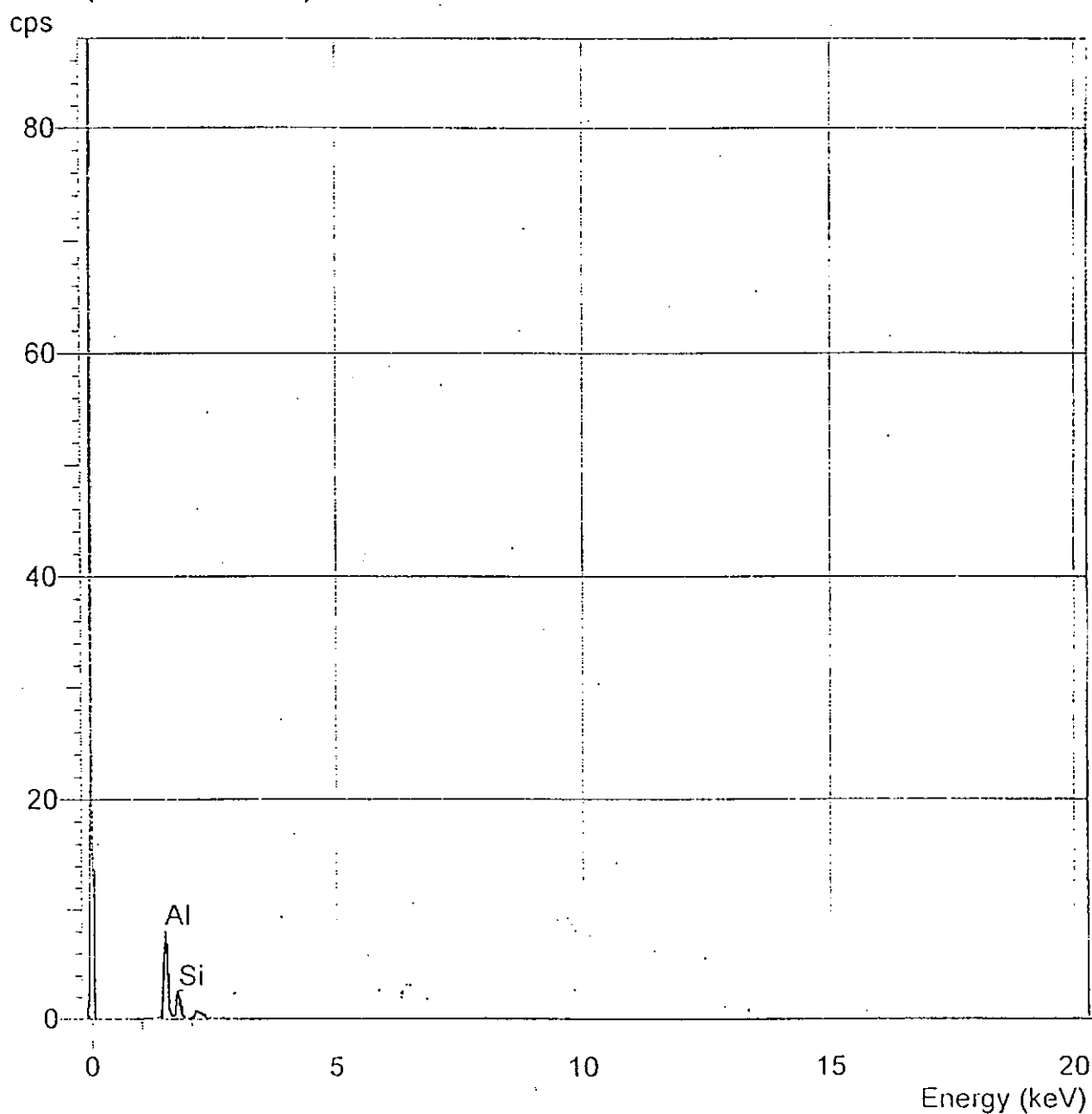 1 peak possibly omitted: 9.70 keV

Standards :
  Al K   Al2O3 23/11/93
  Si K   Quartz 01/12/93
  Ni K   Ni 01/12/93

Elmt	Apparent Conc.	Stat. Sigma	Inten. Corrn.	Std Corrn.	Element %	Sigma %	Atomic %
Al K	5.134	0.168	0.485	0.98	12.29	0.49	23.12
Si K	0.515	0.105	0.546	1.07	1.10	0.26	1.98
Ni K	72.823	1.580	0.977	1.00	86.62	0.55	74.90
Total					100.00		100.00

* = <2 Sigma

Appendix A5: Al_4C_3 phase

SEMQuant results. Listed at 15:40:17 on 4/11/1997
Operator: MRC, HKPU
Client: All ISIS users
Job: Demonstration data SiLi detector
Spectrum label:

Calibration data: Energy Resn.   Area
  Strobe: -6.6   97.57   17781
  Calib. element: 6903.6 157.13   4891
  Gain factor = 49.890
  Livetime   = 50.0 seconds

Sample data: Energy Resn.   Area
  Strobe: -7.2   45.07   33714
  Total spectrum counts = 7180
  Livetime   = 90.0 seconds

System resolution = 59 eV

Geometry (degrees):
  Tilt   =   0.00
  Elevation   =   35.00
  Azimuth   =   0.00
 Entry angle =   0.00

Accelerating voltage = 20.00 kV

Quantitative method: ZAF (3 iterations).
 Analysed all elements and normalised results.
 3 peaks possibly omitted: 0.00, 8.04, 9.74 keV

Standards :
 Al K   Al2O3 23/11/93
 Si K   Quartz 01/12/93

Elmt	Apparent Conc.	Stat. Sigma	Inten. Corrn.	Std Corrn.	Element %	Sigma %	Atomic %
Al K	15.736	0.347	1.278	0.74	61.46	5.99	62.40
Si K	4.516	0.206	0.585	0.91	38.54	5.99	37.60
Total					100.00		100.00

* = <2 Sigma

Operator : MRC, HKPU
Client : All ISIS users
Job : Demonstration data SiLi detector
(4/11/1997 16:15)
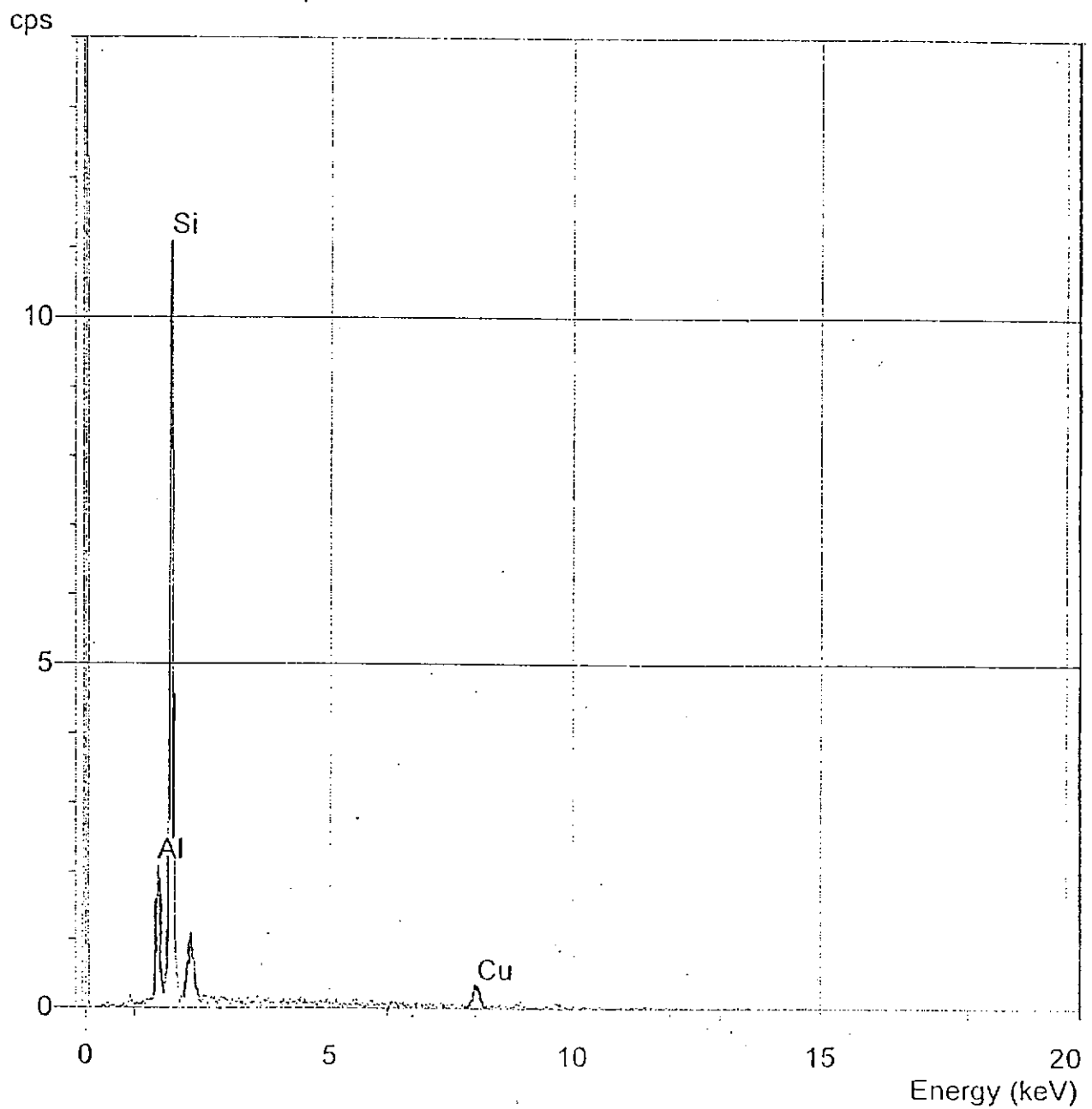
Appendix B1: SiC particle

SEMQuant results. Listed at 16:18:25 on 4/11/1997
Operator: MRC, HKPU
Client: All ISIS users
Job: Demonstration data SiLi detector
Spectrum label:

Calibration data: Energy Resn.   Area
  Strobe: -6.6   97:57   17781
  Calib. element: 6903.6 157.13   4891
  Gain factor = 49.890
  Livetime   = 50.0 seconds

Sample data: Energy Resn.   Area
  Strobe: -7.3   44.59   33724
  Total spectrum counts = 9013
  Livetime   = 90.0 seconds

System resolution = 60 eV

Geometry (degrees):
  Tilt   =   0.00
  Elevation   = 35.00
  Azimuth   =   0.00
  Entry angle =   0.00

Accelerating voltage = 20.00 kV

Quantitative method: ZAF (3 iterations).
  Analysed all elements and normalised results.
  1 peak possibly omitted: 0.00 keV

Standards :
  Al K   Al2O3 23/11/93
  Si K   Quartz 01/12/93
  Cu K   Cu 01/12/93

Elmt	Apparent Conc.	Stat. Sigma	Inten. Corrn.	Std Corrn.	Element %	Sigma %	Atomic %
Al K	3.673	0.212	0.957	0.74	12.23	2.19	13.85
Si K	19.417	0.364	0.855	0.91	72.33	4.99	78.72
Cu K	3.988	0.511	0.823	1.00	15.44	5.38	7.43
Total					100.00		100.00

* = <2 Sigma

Operator : MRC, HKPU
Client : All ISIS users
Job : Demonstration data SiLi detector
(4/11/1997 11:12)
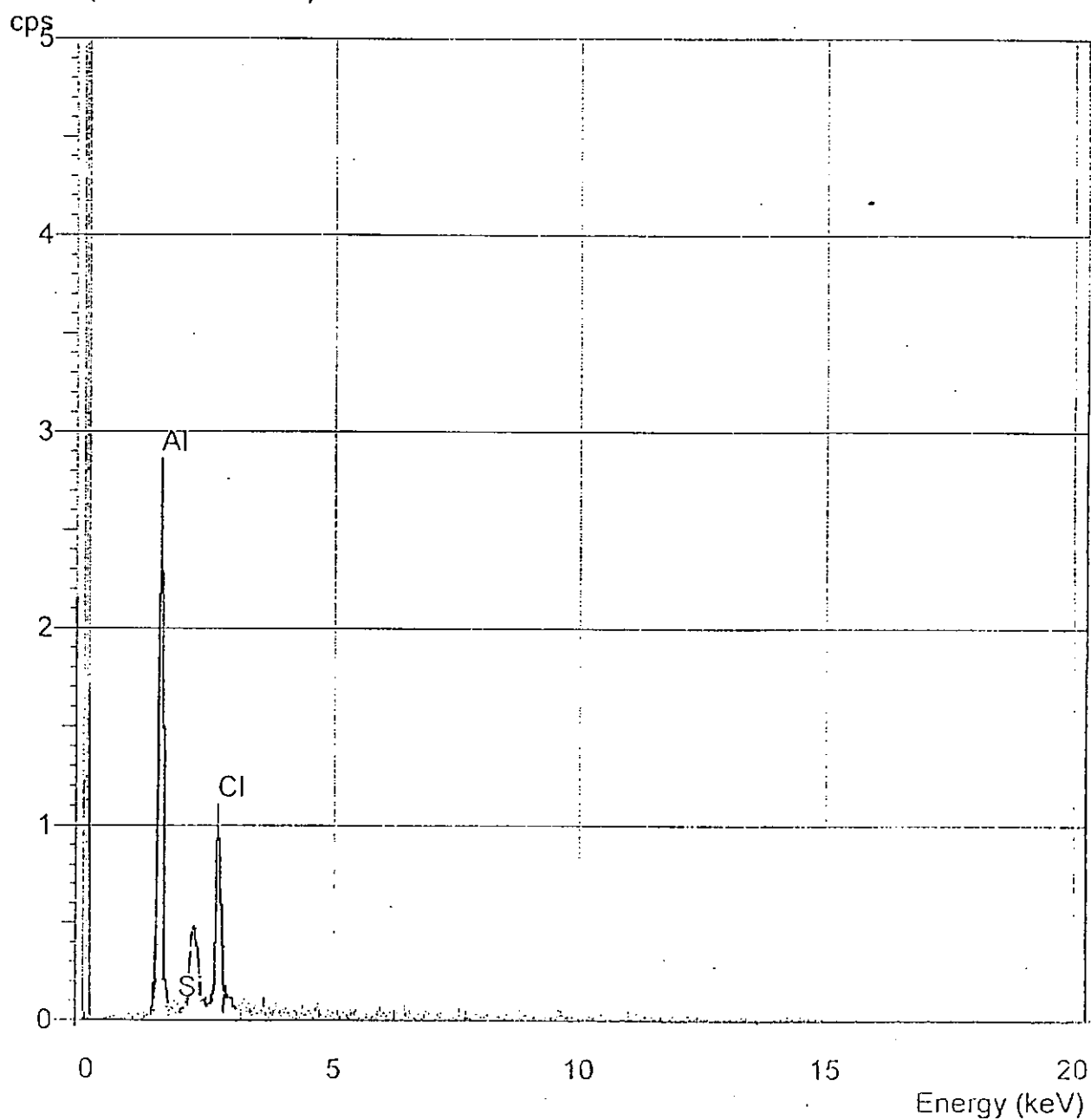
Appendix B2: Corrosion products

SEMQuant results. Listed at 11:16:19 on 4/11/1997
Operator: MRC, HKPU
Client: All ISIS users
Job: Demonstration data SiLi detector
Spectrum label:

Calibration data: Energy Resn.   Area
  Strobe: -6.6 97.57   17781
  Calib. element: 6903.6 157.13   4891
  Gain factor = 49.890
  Livetime   = 50.0 seconds

Sample data: Energy Resn.   Area
  Strobe: -7.1 44.89   33777
  Total spectrum counts = 3331
  Livetime   = 90.0 seconds

System resolution = 60 eV

Geometry (degrees):
  Tilt   =   0.00
  Elevation   =   35.00
  Azimuth   =   0.00
  Entry angle =   0.00

Accelerating voltage = 20.00 kV

Quantitative method: ZAF (2 iterations).
  Analysed all elements and normalised results.
  1 peak possibly omitted: 0.00 keV

Standards :
  Al K   Al2O3 23/11/93
  Si K   Quartz 01/12/93
  Cl K   KCl 15/02/94

Elmt	Apparent Conc.	Stat. Sigma	Inten. Corrn.	Std Corrn.	Element %	Sigma %	Atomic %
Al K	5.374	0.197	1.201	0.74	61.23	27.32	67.09
Si K	0.113*	0.062	0.587	0.91	2.64*	19.38	2.78*
Cl K	1.881	0.133	0.712	0.98	36.13	25.91	30.13
Total					100.00		100.00

* = <2 Sigma